Nanostructured Block Copolymer Templates for Solar Cell Application

Yogita Kumari

Department of Physics
Malaviya National Institute of Technology

This dissertation is submitted for the degree of
Doctor of Philosophy

September 2017

Dedicated to My Family

MALAVIYA NATIONAL INSTITUTE OF TECHNOLOGY JAIPUR
(Institute of National Importance under NITs Act, Established by Govt. of India)
मालवीय राष्ट्रीय प्रौद्योगिकी संस्थान जयपुर
JLN Marg, Jaipur-302017 (India)

Supervisor's Certificate

This is to certify that the thesis entitled ***"Nanostructured Block Copolymer Templates for Solar Cell Application"*** is being submitted by **Ms. Yogita Kumari** (ID No. 2012RPH9009), to the Malaviya National Institute of Technology Jaipur for the award of the degree of Doctor of Philosophy in Physics, is a bonafied record of original research work carried out by her. She has worked under our guidance and supervision and has fulfilled the requirement for the submission of this thesis, which has reached the requisite standard.

The result conetnd in this thesis have not been submitted in part or full, to any other university or institute for the award of any degree or diploma.

(Dr. Kamlendra Awasthi)
Supervisor
Assistant Professor
Department of Physics
MNIT Jaipur (India)

(Prof. K. C. Swami)
Co-supervisor
Retd. Professor
Department of Physics
MNIT Jaipur (India)

Acknowledgements

At very first, I express my sincere gratitude and the best regards to my supervisor Dr. Kamlendra Awasthi, for his guidance during my Ph.D. His knowledge and dedication towards the work always motivates me. He was always available to solve my problems with his kind behaviour. I am very thankful to him to encourage and support me during my journey of research.

I am very thankful to my co-supervisor Prof. K. C. Swami who always supported and encouraged me for doing my research work. He is very knowledgeable and kind-hearted person.

I wish to express my sincere gratitude to Dr. Manoj Kumar, Assistant Professor, MNIT Jaipur for his consistent valuable discussions. I also thank to Dr. Satinder Kumar Sharma, Associate Professor, IIT Mandi, for the fruitful discussion during Ph.D.

I wish my gratitude to Prof. Volker Abetz, University of Hamburg, Germany for his kind response to the my queries and problems facing during my experimental work.

I, sincerely thank to the Head, department of Physics for giving me this opportunity to work in this laboratory.

I also thank to all the Faculty members, Department of Physics, MNIT Jaipur for their suggestions during my research work and for their kind support specially Dr. Kanupriya Sachdev for giving moral support.

I would like to extend my sincere thanks to Dr. Anjali Awasthi, Mrs. Sarika Kashyap, and Dr. Kumud Kant Awasthi for their support and encouragement.

I would also like to express my thankfulness to Dr. Rishi Vyas and Dr. Sarla Sharma for helping me with their valuable suggestions during research work.

I express my heartiest thanks to my friends and labmates Rini Singh, Rajesh Kumar, Anil Kumar, Lokesh Kumar Jangir, Pooja Kumari, Anoop MD, Kamakshi, Shivani Shishodia, Prashant Sharma, Ritesh Dadhich, Aakanksha, and Jyoti from Soft Materials & High Pressure Physics Lab., Department of physics, MNIT Jaipur for their co-operation and making the journey memorable. I would also like to thank to all research scholars, Department of Physics, MNIT Jaipur, specially Dr. Vikas Sharma, Mr. Himanshu Sharma and Mr. Shushant Kumar Singh for their moral support and always available with a solution to my problems.

I specially thank to Dr. Swatantra, Assistant professor, Indian Institute of

Management, Indore, for being a friend, a senior and always having confidence in me for completing this journey. I wish to pay my regards to Mr. Rajeev Kaushik, Assistant Professor, K. K. Jain College, Meerut, for always guiding and encouraging me for the higher studies.

I am fortunate enough to have many good friends who support me in every aspect throughout my Ph.D. career. I am especially grateful to Parsee, Anu Malik, Geetanjali, Rahul Singhal, Ritu Vishnoi, Sarita, Mayuri Rajput, Anjali Raj, Ashwini, Poonam Jangir and Meenakshi for their continuous moral support and encouragement.

I am thankful to all the staff members of Department of Physics and Material Research Centre (MRC), MNIT Jaipur for their kind support

From deep of my heart, I am thankful to my parents, and my in-laws, who always encouraged me to pursue my goals and for always being my strength to face every difficulty and challenge in my life. I am grateful to my sisters Rubal, Varsha, Ritu, Sonam and brother Deepak, to make me strong with their unconditional love and adding the happy moments to this journey.

At last but not the least, I want to give a big thank to the person who has travelled this journey with me and keep motivating me to be on track every time. He is always like a pillar of strength in my life. The most important person in my life, my husband, Mr. Hemant Kumar, thank you so much for everything. This journey was not possible without your support.

I especially acknowledge the Department of Science and Technology, New Delhi, for providing me financial assistance under Women Scientist Scheme to carry out my research work. I also acknowledge the Ministry of Human Resources and Development, New Delhi, for providing me financial assistance under Institute Fellowship to carry out my Ph.D. work.

(YOGITA KUMARI)

Abstract

In the present investigations, supramolecular assembly of diblock copolymer PS-*b*-P4VP and additive HABA have been explored for the fabrication of well-ordered array of TiO_2 nanostructures for their photovoltaic applications.

The preparation and characterization of PS-*b*-P4VP block copolymer nanotemplates have been discussed. Ordered nanotemplates have been prepared using supramolecular assembly from diblock PS-*b*-P4VP and low molar mass additive HABA. Solvent annealing in a selective solvent (1-4 dioxane) affects the mobility of each block and results in the ordering of blocks. The molecular weight and volume fraction of one of the blocks determines the morphology of templates. It has been found that the cylindrical nanotemplates changes to lamellar when the relative volume fraction of minority block (P4VP/HABA) increases from $\sim 0.3 - 0.5$.

Synthesis of TiO_2 nanoparticles by sol-gel method and optimization of their particle size and phase have been discussed in detail. Particle size was calculated using XRD and TEM and initially it was found as $\sim 13\ nm$ at annealing temperature of 350°C which was not the suitable for the deposition into templates. So, an effort had been made to reduce the size and it was reduced from $\sim 13\ nm$ to $\sim 9\ nm$ at the same annealing temperature by using the 1-thioglycerol as capping agent in the same method. Further, the effect of capping agent on thermal stability of anatase phase of TiO_2 nanoparticles were also investigated. It was concluded that the anatase phase was more thermally stable with capping agent as compared to without capping agent. The onset temperature for the phase transformation was increased from 600°C to 700°C. The average crystallite size was found to be increased with the annealing temperature. For the successful deposition of nanoparticles into the nanotemplates, the particle size need to be reduced. For the further reduction in particle size, the nanoparticles were annealed at lower temperature 250°C and the average particle size was reduced to $\sim 5\ nm$, which was confirmed by XRD and TEM.

TiO_2 nanostructures were synthesized using block copolymer nanotemplates by *in-situ* and *ex-situ* approach. The nanotemplates were then backfilled with the titania precursor (TTIP) for the fabrication of TiO_2 nanostructures directed by block copolymer self-assembly. It was estimated that templates were overlayered with TiO_2. On removal of polymer matrix (PS) by heating at 450°C, a connecting network of TiO_2 was observed in case of the lamellar porous templates while a ring-like nanostructure connecting with each other were observed with cylindrical porous templates with

large pore size. The reason for the randomly connecting network was estimated the formation of the layer above the template instead of selective deposition and the high ramp rate of heating were also contributing to this type structures. The melting of polymer with high ramp rate can disturb the shape and size of materials deposited. This difficulty was resolved by adopting another approach; The nanoparticles with size 5 nm were then deposited into the nanotemplates. Nanoparticles were allowed to migrate into the pores and controlled by assembly time. The effect of immersion time on the arrangement of nanodots has been observed. On removal of polymer matrix by UV treatment ordered array of TiO_2 nanodots whose morphology mirrors that of the original nanotemplate. In this study, a sub-20 nm diameter of TiO_2 has been obtained which is in the range of exciton diffusion length, so it has the potential application in optoelectronic devices.

Table of contents

List of figures

List of Abbreviations

AFM Atomic force microscopy

DHN 1, 5-Dihydroxynaphthalene

DSSC Dye sensitized solar cells

ETL Electron transport layer

FFT Fast fourier transform

$\mathbf{f}_R$ Rutile fraction

FTIR Fourier transform infrared spectroscopy

GISAXS Grazing-incidence small-angle Xray scattering

HABA 2-(4-hydroxyphenylazo) benzoic acid

HBL Hole blocking layer

HNA 2-Hydroxy-6-Naphthoic acid

HOMO Highest occupied molecular orbital

ITO Indium-tin oxide

LUMO Lowest unoccupied molecular orbital

NDP 4-Nonadecylphenol

OSC Organic solar cell

P3HT Poly (3-hexylthiophene).

PBA 1-Pyrenebutyric acid

PC Polycarbonate

PCBM Phenyl-C61-butyric acid methyl ester

PCE Power conversion efficiency

PDP 3-Pentadecylphenol

PET Polyethylene terephthalate

PLA Polylactide

PS-b-P2VP Poly (styrene)-b-poly (2-vinylpyridine)

PS-b-P4VP Poly (styrene)-b-poly (4-vinylpyridine)

PS-b-PB Poly (styrene)-b-poly (butadiene)

PS-b-PDMS Polystyrene-b-polydimethylsiloxane

PS-b-PEB-b-PMMA Poly (styrene-b-(ethylene-co-butylene)-b-methyl methacrylate)

PS-b-PEO Poly (styrene)-b-poly (ethylene oxide)

PS-b-PFS Poly (styrene)-b-poly (ferrocenyldimethylsilane)

PS-b-PI Poly (styrene)-b-poly (isoprene)

PS-b-PMMA Poly (styrene-b-methyl methacrylate)

PSC Polymer solar cell

RIE Reactive ion etching

RMS Root mean square

SEBM Syrene-b-(ethylene-co-butylene)-b-methyl methacrylate

SEM Scanning electron microscopy

SRc S welling ratio

TEM Transmission electron microscopy

$\mathbf{T}_g$ Glass transition temperature

TTIP Titanium tetra isopropoxide

XPS X-ray photoelectron spectroscopy

XRD X-ray diffraction

Chapter 1

Introduction

1.1 Block copolymers

It is well known that the polymers are long chain molecules and broadly, they can be divided in two categories; homopolymer and copolymer. Homopolymers are the polymer consisting of only one monomer while copolymer is comprising of two or more than two monomers. In copolymers, these monomers are arranged in two ways; random and periodic. Second one is known as block copolymer. So, block copolymers are the polymers comprising of the blocks of monomers repeating in a particular sequence and according to the number of blocks they are called di, tri or multi block copolymers, for example;

A-A-A-A-A-A-A-B-B-B-B-B-B-B **AB diblock copolymer**

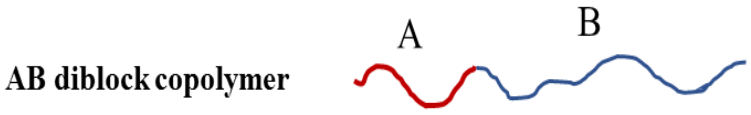

A-A-A-A-A-A-A-B-B-B-B-B-B-B-A-A-A-A-A-A-A **ABA triblock copolymer**

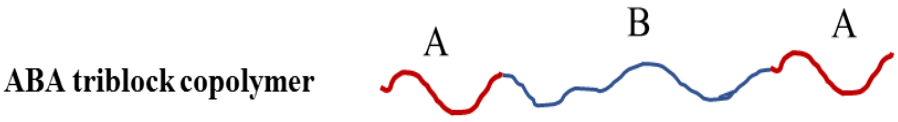

1.1.1 Self-assembly

Self-assembly is an apposite process to arrange the material on the nanoscale over large areas. Block copolymers are well-known for their ability to self-assemble into various well-ordered morphologies within nanometer dimensions [1, 2]. Block copolymers consist of immiscible copolymers which are covalently bonded with each other.

Generally, polymers are macrophase separated similar to oil and water but in case of block copolymers, covalent linking prevents the macrophase separation. However, the non-favourable interactions between the blocks induce the phase separation but due to their connectivity on a sub-micron scale, the phase separation occurs within a range of 5-100 nm [1]. It is also known as microphase separation which is impelled by chemical irreconcilability between the blocks.

There are many parameters that govern the arrangement of blocks and surface morphological features; molecular weight of block copolymers, degree of polymerization $N = N_A + N_B$ i.e. total number of repeating units, volume fraction of blocks (f_A,f_B), chain flexibility, chain architecture and Flory-Huggins interaction parameter between the blocks (χ) [3]. Size of the domains or blocks mainly depend on the molecular weight of block copolymers. Arrangement of the domains in the various shape like spherical, cylindrical, lamellar, or gyroidal is primarily governed by the volume fraction of the copolymers. As the polymer chains are linked with covalent bond so the size of the domains commensurate with polymer chain length. Degree of polymerization defines the entropic contribution to Gibbs free energy of block copolymers and non-favourable interactions between the blocks causes repulsion between them. This incompatibility is expressed by Flory-Huggins interaction parameter χ [4] and it identifies as enthalpic contribution to Gibbs free energy of block copolymer. χ can be defined as;

$$\chi_{AB} = \frac{Z}{k_B T}[\varepsilon_{AB} - 1/2(\varepsilon_{AA} + \varepsilon_{BB})] \tag{1.1}$$

Where Z represents the nearest neighbour monomer unit to a copolymer, ε_{AB} is defined as the interaction energy per monomer between A and B. It is clear from the above equation that χ is a function of temperature.

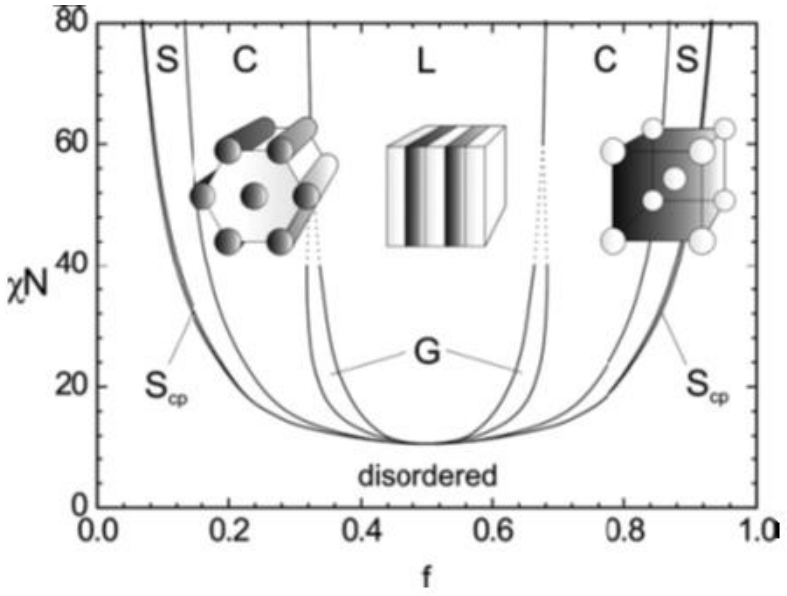

Fig. 1.1 Phase diagram of diblock copolymer calculated using SCFT. S, C, L, and G represent spherical, cylindrical, lamellar, and gyroid respectively [5].

The theory of self-assembly of block copolymers has been well-predicted by self-consistent field theory (SCFT). Matsen and Bates determined the phase diagram to define the shape of the blocks in the block copolymers [6]. Phase diagram is defined as the plot between χN and the relative volume fraction f of minority blocks as shown in figure 1.1. Basically, it is the phase balance between entropy and enthalpy which drive the microphase separation. The structure of the nanodomains in the equilibrium are corresponding to the minimized non-favourable interactions between A and B block, when the polymer chains are not overstretched. The strength of segregation of domains is proportional to χN and it was found that when the interaction between the blocks is relatively weak as $\chi N < 10.5$ the domains are in disordered state and $\chi N_{(ODT)} = 10.5$ is considered as order-disorder transition for the symmetric block copolymer. As the value of χ increases the domains are phase separated as shown in figure 1.1. $\chi N < 10.5$ is defined as the weak segregation regime and theoretical aspects were explained by Leibler and co-workers [7]. Earlier the phase behaviour of the block copolymers was explained by Hefand and co-workers in the strong segregation regime ($\chi N > 100$) [8, 9]. Matsen and Bates have further explained the phase behaviour of the nanodomains in the intermediate segregation regime ($10.5 < \chi N > 100$) [6]. Phase separation strongly depends on temperature as defined in equation (1.1). As the temperature increases, χ decreases and at a certain value of χN copolymer blocks are not able to maintain the phase separation and undergoes to order-disorder transition and vice versa.

Different morphologies of a diblock copolymer in the intermediate segregation regime as a function of volume fraction of one block are shown in figure 1.2 (Red and blue colour represent the block A and B respectively) and it is concluded that the symmetrical diblock copolymers are phase separated in lamellar microdomains while asymmetric diblock copolymers are obtained in the ordered spherical, cylindrical and gyroidal microdomains. In spherical morphology, the minority blocks are arranged in body cubic centre (BCC) manner. And in cylindrical morphology, the minority domains are arranged in hexagonally packed cylinders (HCP).

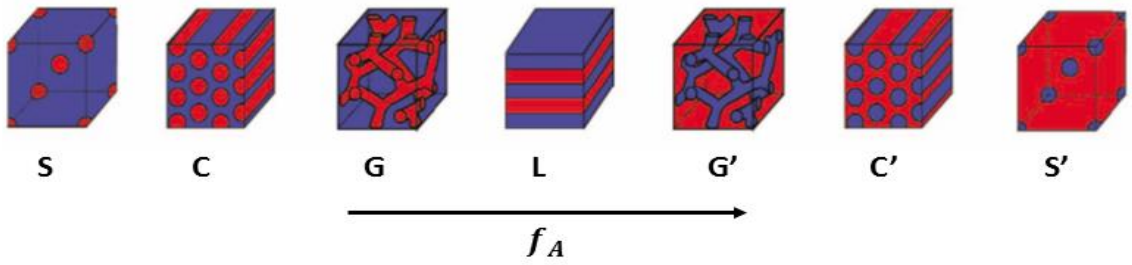

Fig. 1.2 Various phase structures as a function of volume fraction of one block [10].

1.1.2 Supramolecular assembly

Supramolecular assembly (SMA) is the process in which the small molecules called additives are attached with the one of the copolymer blocks via some specific interactions. The addition of these small molecules swells significantly one of the blocks and induces the interesting phase behaviour of the block copolymers. These small molecules are associated with the copolymer with weak interactions or non-covalent bonds. Generally, they interact with copolymer via hydrogen bond. As these molecules attach with one of the block so the relative volume fraction of that block altered and results in the change of morphology. Another advantage with the SMA is the readily removal of these small molecules by selective solvents which make them interesting for the fabrication of variety of functional nanomaterials. An example of the supramolecular complex system is polystyrene-*b*-poly(4-vinylpyridine) (PS-*b*-P4VP) and pentadecylphenol (PDP) which has been widely investigated by Ikkala and co-workers [11–14]. The chemical structures and schematic representation of PS-*b*-P4VP and PDP are shown in figure 1.3 (a), PDP molecules possess the hydroxyl group which is bonded with pyridine group of P4VP via hydrogen bond. PDP molecules have polar backbone and non-polar alkyl tails with a sufficient repulsion between them. This repulsion is responsible to form the structures within structures with two length scale (figure 1.3 (b)). So, PDP molecules are microphase separated from P4VP and non-polar alkyl tails are aligned normal to the P4VP copolymer (shown in figure 1.3 (a)).

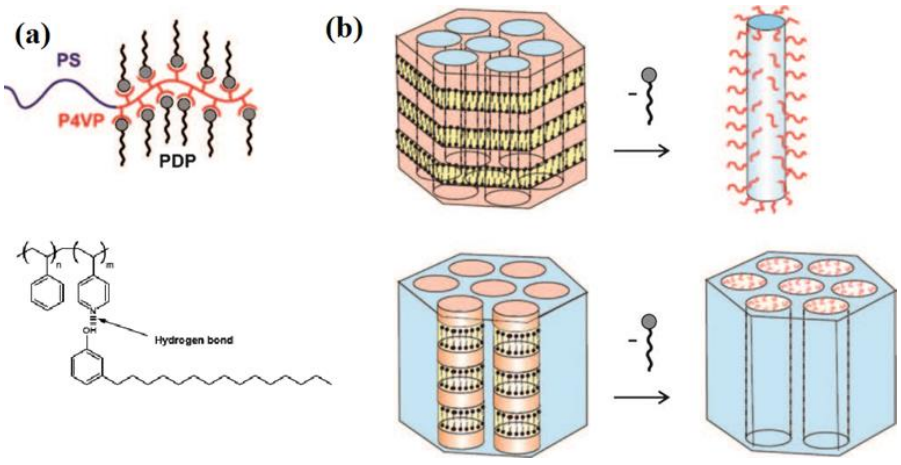

Fig. 1.3 (a) Chemical structures of supramolecular complex PS-b-P4VP (PDP) and its schematic representation (b) Schematic representations of structures within structures ; cylinders within lamellae and lamellae within cylinders and the formation of nanorods and nanoporous membranes [5].

Size of the nanodomains and the morphologies can be tuned by changing the content of PDP or additives. Furthermore, PDP or additives can be washed away easily and leads to the formation of porous nanostructures or nano-objects. Figure 1.3 (b) shows

schematic for PS-*b*-P4VP (PDP) showing structures; cylinders within lamellae and lamellae within cylinders and removing the PDP molecules selectively results into the formation of nanorods and nanoporous membranes functionalized with P4VP respectively. These nanoporous membranes can be further used as nanotemplates.

1.1.3 Nanolithography

Nanolithography is the process to make the various type of pattering on the nanometer scale. Block copolymer lithography provides an alternative tool to the conventional photolithography or e-beam lithography. It is compatible with the "chip-on-silicon" technology, therefore, one may also combine the "top-down" process with the "bottom-up" process [15]. In photolithography, shrinkage of feature size is limited by the wavelength of source and the photoresists used. On the other hand, e-beam lithography provides the feature size is sub 10 *nm* but this process is limited by the high fabrication cost. Block copolymer lithography overcomes these issues and the large area fabrication is easier and cost effective than the conventional photolithography. Block copolymer lithography has been under intensive research after first investigation on this technique by Park *et al.* [16]. They have used microphase separated diblock copolymer (PS-*b*-PB) for the fabrication of patterned silicon nitride. It is two-step process; one is to create the mask by removing one of the blocks selectively, second, pattern transferring to other materials. Depending on the chemical nature of the different block copolymers, different techniques have been used for the selective removal of one of the blocks and then the pattern transfer [16–19].

1.2 Titanium dioxide (TiO_2) nanomaterials

An extensive research for nanomaterials has been going on in the field of science and technology since past decades. When the size of the materials is reduced to the nanoscale, their structural, thermal, electrical and optical properties altered drastically. TiO_2 nanomaterials have elicited the immense interest because of their excellent stability, physiochemical properties at nanoscale as well as great availability and moderate cost. They are commonly used in various commercial products like pigments, sunscreen, paints, ointments and toothpaste [20–23].

1.2.1 Crystal structure of TiO_2

Mainly TiO_2 exhibits three polymorphs, anatase, rutile, and brookite. Each polymorph has the different structure and different properties. Thermodynamically, rutile is most stable while the other two are metastable and transforms into rutile at higher temperatures. However, the transformation from anatase to rutile and brookite to

rutile depends on various parameters; precursor, reaction temperature, pressure, and initial particle size. Anatase phase is commonly obtained and transformed into rutile on annealing at the temperatures around $500°C - 700°C$. Brookite TiO_2 is less investigated polymorph. Figure 1.4 shows the unit cell structures of anatase, rutile and brookite TiO_2. Rutile has tetragonal structure with six atoms per unit cell. Anatase also have the tetragonal structure but with a slightly larger distortion of TiO_6 octahedron. Brookite possess the orthorhombic structures. Owing to their suitable band structure and high surface reactivity (band gap of rutile - 3.0 eV, anatase - 3.2 eV) render TiO_2 useful for many applications; gas sensing, photovoltaics, batteries, catalytic activity [24–29]. Energy level matching with materials for solar cells and the lower charge carrier recombination rate bestowed anatase TiO_2 nanomaterials with potential to be used for solar cell applications [24].

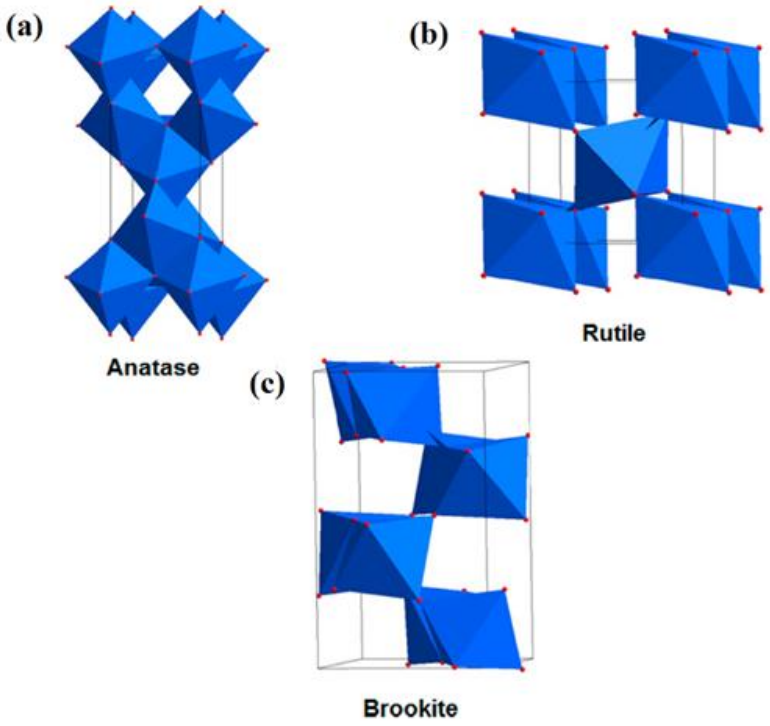

Fig. 1.4 Schematic representation of unit cell of different polymorph of TiO_2 (a) anatase (b) rutile (c) brookite [30].

1.2.2 Fabrication of TiO_2 nanostructures

TiO_2 nanostructures (nanorods, nanodots, nanowires) have been synthesized using several routes; sol-gel method, hydrothermal, solvothermal, direct oxidation, anodization and templating [31–33]. Among them templating process is the best way to obtain the ordered nanostructures [34]. Ordering of TiO_2 nanostructures provides the better pathways for the charge carriers and reduce the charge recombination which is one of the important factors that affects the power conversion efficiency (PCE) of solar cell. It has been investigated that TiO_2 nanorods and nanotubes

enhance the power conversion efficiency of solar cell as compared to thin film of TiO_2 [35, 36]. TiO_2 nanorods and nanotubes are advantageous instead of film as they provide the large donor-acceptor interface area for electron transfer. Moreover,the ordering of the nanostructures helps in the reduction of charge recombination and fast transportation of charge-carriers to the charge collecting electrode. Alumina templates are commonly used for the fabrication of TiO_2 nanorods/nanotubes. The length and diameter of nanorods/nanotubes can be tuned by varying the pore size and thickness of alumina templates [37]. The pores size and the thickness of alumina templates can be varied on varying the anodization time and voltage. These nanorods and nanotubes have been used in the active layer of the device and enhancement in PCE of solar cell has been observed. This enhancement may be attributed to the availability of number of junctions and ordered pathways for the exciton dissociation and charge transportation as compared to thin film. However, the diameter of the nanorods and nanotubes synthesized by alumina templates are larger than that of exciton diffusion length which limits the generation of charge carriers (electrons and holes). This limitation can be overcome using the block copolymer nanotemplates.

1.3 Block copolymer nanotemplates directed nanostructures

The ordering in the block copolymers thin films can be extended to the inorganic materials. Using the block copolymer nanotemplates, the nanostructures with higher aspect ratio can be obtained than the other methods based on self-assembly. However, commercially available alumina nanotemplates have the high aspect ratio but block copolymer nanotemplates provide a denser array of pores (less size of pores and periodicity) and it comes with plenty of patterns because of their self-assembly into various morphologies on nanometer scale. Block copolymer nanotemplates with porous structures normal to the substrate are mainly used for the fabrication of ordered nanostructures. Mainly the cylindrical and lamellar block copolymer structures are used for the fabrication of nanorods, nanowires, nanodots and nanowalls [38–40]. The fabrication process mainly involves three steps;

1. Selective removal of sacrificial block and creation of nanoporous templates.
2. Backfilling of porous channels.
3. Removal of remaining polymer matrix.

There are the different ways to remove the polymer block like UV etching, chemical etching or chemical dissolution, depending on the chemical nature of the block copolymer. Nanoporous channels can be backfilled by sol-gel method or direct deposition of nanoparticles into the templates. In sol-gel method, titanium alkoxides

are generally used for the backfilling. However, titanium alkoxides are not much stable and can by hydrolysed even in the moisture which can result in the pore blocking before diffusion of the sol into the templates. So, the reaction conditions have to be controlled carefully. Another way is to deposit the pre-synthesized TiO_2 nanoparticles into the templates. It offers the flexibility to tailor the properties of TiO_2 nanoparticles before deposition and can be controlled by their assembly time. Polymer templates/matrix can be removed by UV irradiation, pyrolysis and plasma etching.

1.4 Objectives of thesis

Block copolymer nanotemplates using supramolecular assembly of diblock copolymer PS-*b*-P4VP and additive HABA have been explored for the fabrication of TiO_2 nanostructures. The main objectives of the thesis are as follows;

- To fabricate the block copolymer nanotemplates with different morphologies varying their molecular weight and the volume fraction.
- To synthesize TiO_2 nanoparticles and optimization of their particle size and phase.
- To fabricate the ordered TiO_2 nanostructures using the prepared block copolymer nanotemplates by sol-gel method and direct deposition of nanoparticles into templates.

Chapter 2

Literature Review

2.1 Brief introduction

The trend of miniaturization in devices along with high throughput and lower consumption of energy promotes the field of nanomaterials in the industrial applications. Block copolymers have elicited immense interest over more than a decade for their use in semiconductor device applications because they possess the ability to self-assemble in the nanometer scale (typically 5 - 100 nm) with various morphologies [5, 41]. This length scale encompasses the same which is required for the futuristic emerging semiconductor devices for industrial applications. The rate of advancement in the semiconductor industry depends on the high resolution and low scale patterning on the substrate. Conventional UV photolithography have been used for pattering on the substrates and nowadays patterning with a 40 nm scale can be successfully created on the substrate. It is notable that further improvement in the pattering structures in terms of scale with the remarkable efficiency makes the process tedious and increase the overall cost. The replacement for the UV photolithography such as nanoimprint lithography, extreme UV photolithography, and interference lithography are still facing some difficulties for next generation device applications. These issues intensify the growing interest in self-assembly of materials which offers the well-ordered structures with a precise control at atomic or molecular level. For the device application of self-assembly, the nanomaterials, as a device component, are to be deposited on the substrate in a well-organized manner. Mansky *et al.* have first proposed and demonstrated the block copolymer lithography using a block copolymer with spherical microdomain structure [42, 43]. The introduction to various morphologies and basic concept of self-assembly of block copolymers have already been addressed in **section 1.1**. Electronic applications of block copolymers are more moderate and seek to connect their self-assembling properties so that they may be used as an alternative for the polymeric photoresist used in current practice. This approach offers the opportunity to explore the more benefits of self-assembly of block copolymers towards the device applications. With this aim, enormous efforts

have been dedicated to exploit the practical applications of block-copolymer-based nanostructures. Despite of ease of process and spatial scale of block copolymer pattering, still the work remains for the practical use of self-assembly in electronics applications. To combine the block copolymer lithography with the current photolithography, important issues of domains orientation and lateral ordering must be focussed. The cylindrical domains are preferable than spherical domains for pattering or templating, owing to their stability or connectivity to the substrate and high aspect ratio. In this chapter, we have reviewed the literature for materials and methods for self-assembly of block copolymers, controlling the orientation of the microdomains and the fabrication of nanostructures using block copolymers for device applications.

2.2 Materials

2.2.1 Diblock copolymers

Diblock copolymers consist of two monomers grouped together in a homogenous block of the polymer chains. The phase diagram for possible morphologies and their dependency on volume fraction (f), degree of polymerization (N) and Flory-Huggins interaction parameter (χ) as well as schematic representation of the morphologies have been addressed in **section 1.1.1**. Diblock copolymers represents the simplest architectures rather than the other block copolymers (triblock and multiblock) and these are the most investigating block copolymers for the device applications. Mostly diblock copolymers are consisting of PS, here are some examples for diblock copolymers; PS-*b*-PMMA, PS-*b*-P4VP, PS-*b*-P2VP, PS-*b*-PEO, PS-*b*-PI, PS-*b*-PB. Among them PS-*b*-PMMA and PS-*b*-P4VP have been extensively investigated for different structures, ordering, alignment and fabrication of nanostructures. We have reviewed mainly the diblock copolymers so in order to avoid recapitulation the literature is discussed in detail in further sections.

2.2.2 Triblock copolymers

Triblock copolymers comprise of three dissimilar monomers (ABC triblock copolymer) grouped in homogenous blocks having repulsive interactions among them. Unlike diblock copolymers, the phase separation of microdomains and the morphology of ABC triblock copolymers not only depends on f, N and χ but also depends on the mutual interactions between the blocks A-B, B-C and C-A, and the sequence of the blocks. Therefore, more complexed morphologies have been anticipated in triblock copolymers. Zeng *et al.* have theoretically calculated the phase diagram for the morphology of triblock copolymers [44]. They have focussed on the dependence of

morphology on the sequence of block and strength of interactions between the blocks. A variety of morphologies possible in triblock copolymers have shown in figure 2.1.

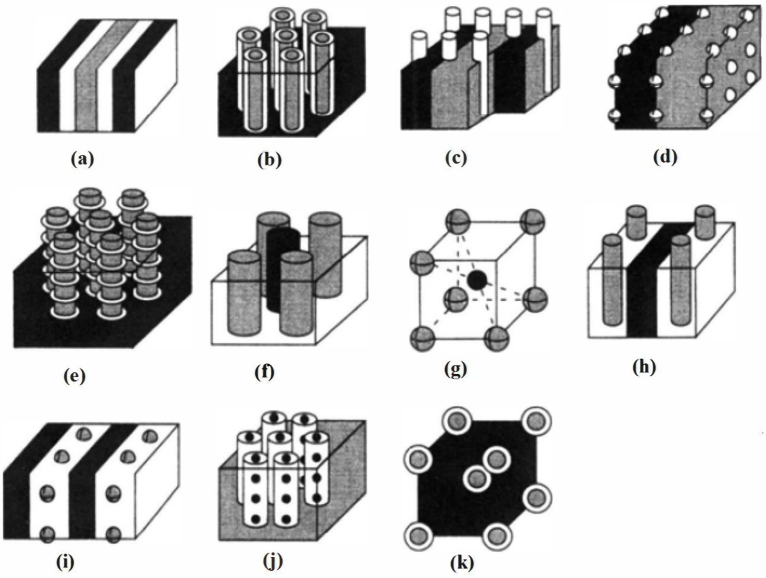

Fig. 2.1 Schematic representation of phase separated domains of ABC triblock copolymer. A-dark, B-white, C-grey. (a) Lamellae phase, (b) Coaxial cylinder phase (c) Lamellae-cylinder I, (d) Lamellae-sphere I, (e) Cylinder-ring phase, (f) Cylindrical domains in square lattice structure, (g) Spherical domains in CsCl type structure, (h) Lamellae-cylinder II, (i) Lamellae-sphere II, (j) Cylinder-sphere phase, and (k) Concentric spherical domains in BCC structure [44]

Experimentally, Stadler *et al.* investigated the morphology of triblock copolymer PS-*b*-PEB-*b*-PMMA (SEBM) with the variation of volume fraction of midblock EB [45]. EB formed cylinders with PS and PMMA lamellae when the volume fraction of the blocks was S:EB:M = 48:17:35 wt%, respectively (shown in figure 2.2). While EB block forms rings around PS cylinders with PMMA lamellae when the ratio was changed to S:EB:M = 45:6:49 wt% respectively (figure 2.3). A new morphology similar to "knitting pattern"was also observed (shown in figure 2.4) when the fraction of EB was 27% [46]. It was considered the intermediate morphology of two morphologies; A, B, and C lamellae and A, and C lamellae with B cylinders. It is notable here that with these complex morphologies nanofabrication is still not much explored.

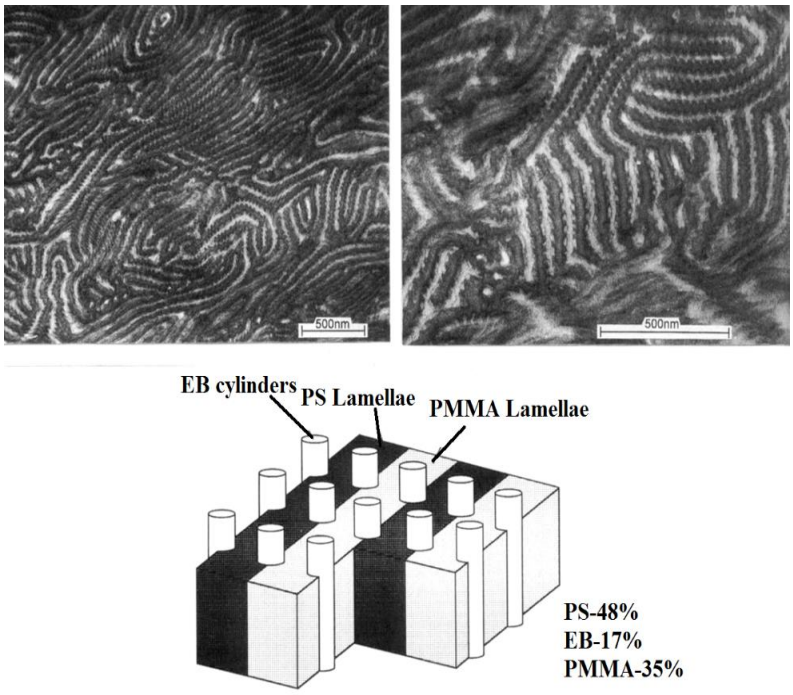

Fig. 2.2 Surface morphology of SEBM (EB-17%) at lower magnification (top left) and higher magnification (top right). In the top right image, EB cylinders appears as spheres in cross section view. Schematic representation of EB cylinders dispersed in PS and PMMA lamellae (Bottom) [45].

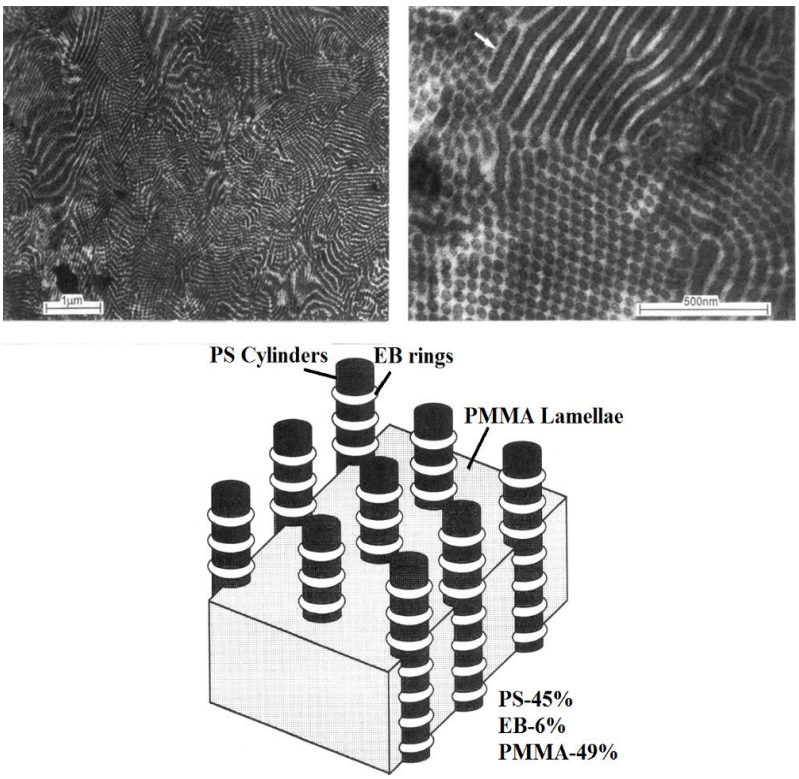

Fig. 2.3 Surface morphology of SEBM (EB-6%) at lower magnification (top left) and higher magnification (top right). Schematic representation of PS cylinders surrounded by EB rings and dispersed in PMMA lamellae (bottom) [45].

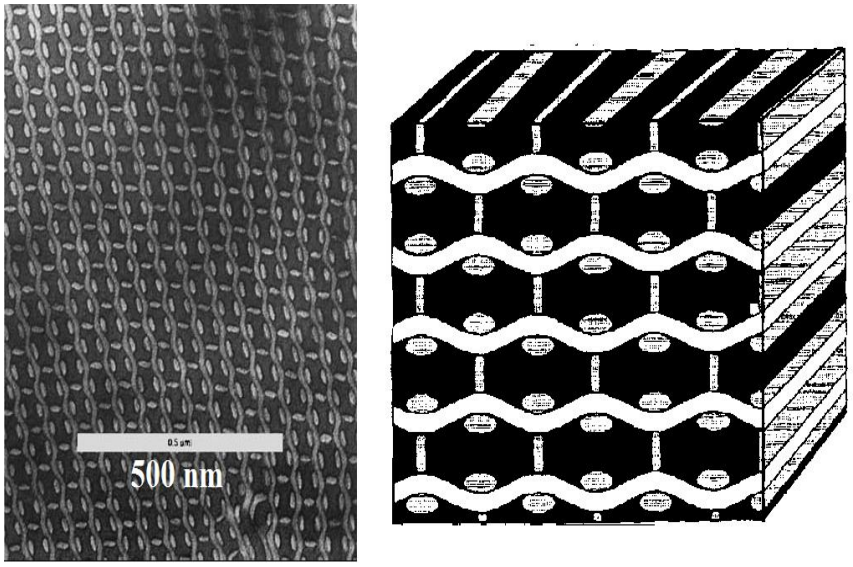

Fig. 2.4 TEM image showing the Morphology of SEBM (EB-27%) stained with RuO_4 (left). 3-D schematic representation of knitting pattern showing on left (right) [46]

2.2.3 Supramolecular complex system

Supramolecular complex systems are very promising for tailoring the morphology of thin films of block copolymer and formation of nanotemplates. Most studied block copolymer for the supramolecular assembled system is PS-*b*-P4VP. Many additives (PDP, NDP, DHN, HABA, PBA, and HNA etc.) have been investigated with different molar ratio and their effect on the morphology have been discussed in detail by many groups [47, 48]. Mostly, carboxylic or hydroxyl functional group of small molecules have been hydrogen bonded with P4VP block. Stamm and co-workers have extensively investigated the morphology of the supramolecular assembled thin films using additives PBA and HABA [49–52]. Both the additives selectively linked with P4VP block via hydrogen bonding of carboxylic group with pyridine group of P4VP. It is easy to create the pores or channels by surface reconstruction using a solvent like ethanol or methanol as P4VP/PBA and P4VP/HABA are soluble in ethanol/methanol while PS is insoluble in ethanol/methanol. FTIR is suitable technique to make sure that the additive has been removed. The removal of the additive in PS-*b*-P4VP can be confirmed by FTIR that the characteristic peak corresponding to the hydrogen bond of carboxylic group with pyridine group was absent after surface reconstruction by ethanol and the signals for free pyridine group was available. They demonstrated that the pure block copolymers show the P4VP cylindrical domains surrounded with PS matrix, while supramolecular system shows the lamellar morphology. The molecular weight of PS-*b*-P4VP in this study was taken 32.9 kg/mol (PS) – 8 kg/mol (P4VP) which corresponds to the P4VP cylindrical domains surrounded with PS matrix according to the phase diagram. But in supramolecular system, binding of PBA with P4VP (equimolar ratio) alters the

relative volume fraction of P4VP and the cylindrical morphology changes to lamellar morphology (figure 2.5). On the surface reconstruction, the nanotemplates with the pores of 12 *nm* with a periodicity of 26 *nm* have been obtained.

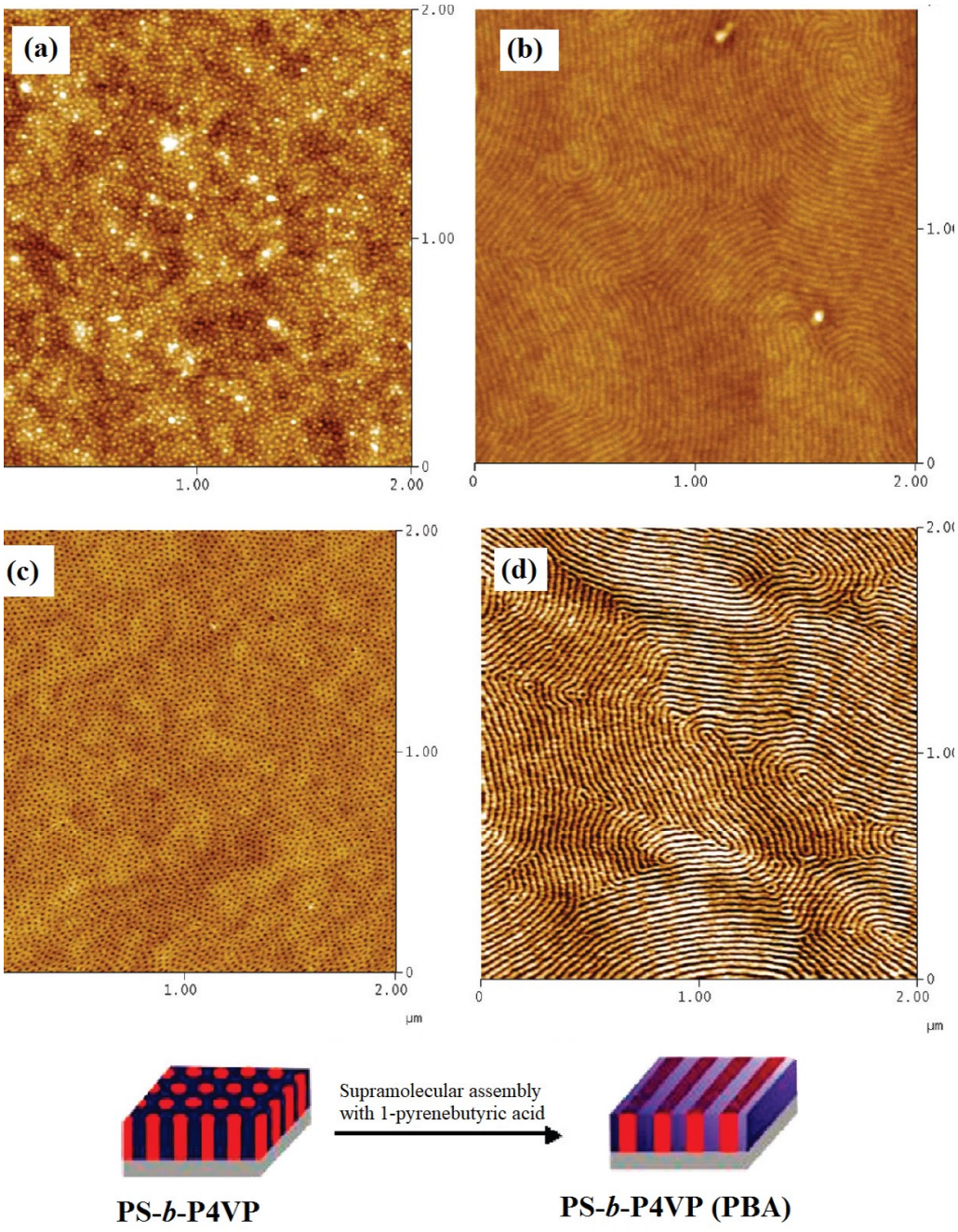

Fig. 2.5 AFM images of (a) PS-*b*-P4VP thin films, (b) PS-*b*-P4VP (PBA) thin films, (c) nanotemplates on surface reconstruction of PS-*b*-P4VP in ethanol (d) nanotemplates created from PS-*b*-P4VP (PBA). Schematic representation of switching in morphology on addition of PBA (bottom) [50]

Brinke *et al.* [53, 54] and Tung *et al.* [48, 55] have also investigated the interaction of PDP with P4VP and were able to observe structure within structure morphologies. The reversible switching of orientation of microdomains from perpendicular to parallel

to the surface by using different annealing solvents [49, 50] were also observed by Stamm *et al.*. It was due to the different selectivity of solvents to each copolymer. Correlation between the orientation of microdomains in thin films and the content of associated small molecules is well reported and observed that the adequately high molar ratio of small molecules drives/directs the perpendicular orientation of microdomains [47, 52]. Here, it is concluded that the supramolecular assembly is incredibly powerful concept to obtain the different morphologies with the same block copolymer and easy fabrication of nanotemplates.

Effect of Content of Small Molecules

The morphology of supramolecular assembled thin films depends on choice of the small molecules and geometrical parameters governed by the content of the small molecules [48, 56, 57]. DHN is a ditopic molecule and it possess the single type of hydrogen bonding group (hydroxy) unlike HABA (it possesses two type of hydrogen bonding group; hydroxy and carboxylic). The stoichiometry ratio of P4VP and DHN greatly influenced the geometrical parameters of porous structures. DHN selectively enhances the P4VP block via hydrogen bonding and it should be resulted in the lamellar morphology in the bulk according to phase diagram. But the selectivity of the solvents towards each block also plays the role in the arrangement of the domains. Instead of lamellae, nodules of P4VP/DHN protruding from PS matrix has been observed which can be attributed to higher solubility of PS in THF than that of P4VP[58]. This solubility difference between PS and P4VP depends on the content of DHN also and it is estimated to be highest for the equimolar ratio of P4VP and DHN. It should be mentioned here that even in case of P4VP/DHN fraction equal to 0.7 the nodular morphology with the PS matrix is observed, despite of the P4VP/DHN being the majority phase. This type of structures is known as "inverted structures" which resulted due to the greater affinity of solvent for the minority block [59]. It is also to be noted here that cylindrical morphology have already been obtained in PS-*b*-P4VP/HABA system with the same composition of copolymers [49]. So, it is concluded that the type of additives is solely responsible for the nodular morphology.

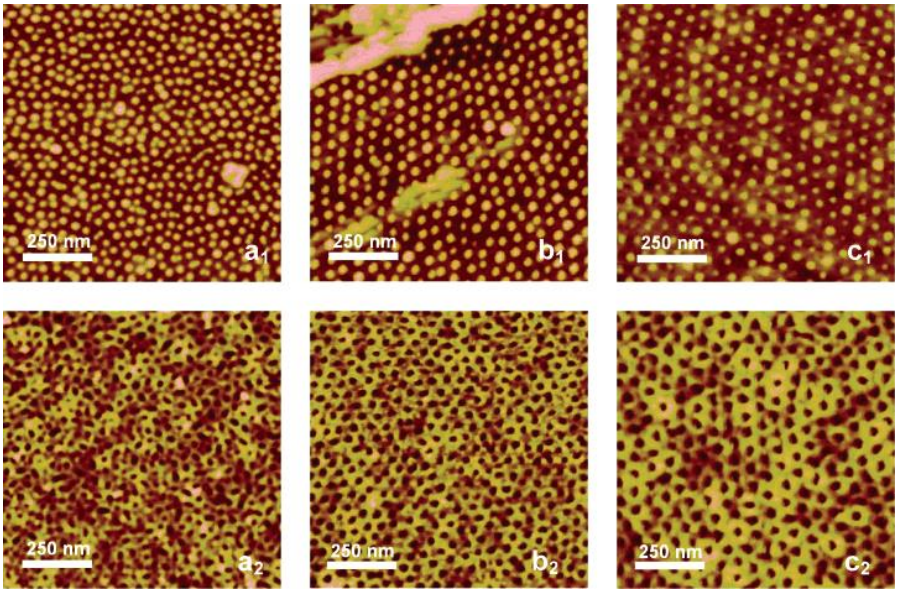

Fig. 2.6 AFM images of PS-*b*-P4VP (DHN) supramolecular assembled thin films with P4VP: DHN (a1) 1:0.5, (b1) 1:2, and (c1) 1:4 (top) and corresponding nanotemplates (bottom) [58].

The geometrical parameters for the nanoporous structures rely on how deep the solvent penetrate in the additive. So, it is obvious that it must be affected by the content of additive. In case of the ratio P4VP:DHN of 1:0.5 the nodules are found to be smaller in size and periodicity than equimolar ratio. On increasing the ratio to 1:2, DHN molecules are in access and they may form hydrogen bonds with the DHN molecules only and the phase separation may also occur. The bright patches in figure 2.6 (c) is an indication of phase separation. However, in the higher ratio (1:4) the DHN phase separation does not occur, that suggest the excess incorporation of DHN in P4VP block. It is concluded that on increasing the content of low molar mass additive the size and the periodicity of the porous structures increases. Further, the composition dependent morphological features of supramolecular system of PS-*b*-P4VP (HABA) were investigated by Stamm *et al.* As far as the morphology concerned, cylindrical P4VP/HABA domains dispersed in PS matrix were obtained corresponding to stoichiometric ratio and as the molar ratio of additive is far lower than that of stoichiometric ratio, the cylindrical domains transform into the spherical domains. As the molar ratio increases higher than the stoichiometric ratio, the mixed cylinders (parallel and perpendicular) with the higher ratio of laterally oriented cylinders were obtained. The morphology of the supramolecular assembled thin films can be controlled by the solvent annealing also which is omitted in this section and further discussed in section 2.3.2.

2.3 Ordering in thin films

To achieve the ordering in thin films is an emerging issue for the fabrication of well-ordered nanostructures for device application for the past few years. Generally, the domains are not perfectly arranged in the as-deposited supramolecular assembled thin films. It happens because of the fast evaporation of solvents, which does not provide the sufficient time to rearrange the molecules in the equilibrium. The ordering and the alignment of microdomains are driven by two surface interactions; polymer-substrate and polymer-air [2]. The block, interacts strongly with substrate, prefers to stick parallel to the substrate. Lateral ordering and the desired orientation of microdomains can be achieved by thermal annealing, solvent annealing, shear or electric field [60–63]. Annealing is an efficient approach to obtain the long-range ordering in the thin films.

2.3.1 Thermal annealing

The conventional strategy to improve the lateral arrangement of the microdomains in block copolymer thin films commonly depends on annealing step to enhance the chain mobility. It is usually done by elevating the temperatures of the thin films above the glass transition temperature (T_g) of each copolymer. Annealing temperature is a crucial parameter for the ordering and alignment of microdomains in thin films. For the vertically aligned domains, the surface energies for both the copolymer blocks should be nearly equal. The surface energies and their difference is a function of temperature. In a special case of PS-*b*-PMMA, both the blocks PS and PMMA have the almost same surface energy over a broad range of temperature [64]. This property makes PS-*b*-PMMA a unique candidate for the self-assembly via thermal annealing. The diffusivity (D(T)) of the polymer chains is represented by Arrhenius equation as follows;

$$D(T) \sim \frac{1}{t} = Aexp(-\frac{\triangle E_a}{RT}) \tag{2.1}$$

Where t, A, R, T and $\triangle E_a$ represent annealing time, constant, ideal gas constant, annealing temperature, and activation energy of polymer respectively. It is clear from the above equation that increasing the annealing temperature the diffusivity of the polymer chains increases which reduces the annealing time. The minimum annealing time for the self-assembled defect free lamellar forming PS-*b*-PMMA thin films was reported by Welander *et al.* [65]. The annealing time is a limitation for lithographic applications of block copolymer. However, the self-assembly of thin films have already been achieved within few minutes using hot plate or rapid thermal annealing process [66, 67]. Recently, Seshimo *et al.* have obtained sub-10 *nm* vertically oriented lamellae in modified polysiloxane-based block copolymers by thermal annealing at 130°C in atmospheric conditions for 1 minute [68]. Perpendicularly aligned PMMA

cylinders in PS matrix with a high aspect ratio ($h/d \approx 7$) have been investigated with a thickness window of 5 nm to 400 nm under rapid thermal annealing at high temperatures (190°C $\leq T_a \leq$ 310°C) [69]. Initially the annealing temperature was optimized by keeping the annealing time (900 s) and thickness of film ($\approx$ 35 nm) same. Below and above 270°C, disorganized PMMA cylinders were observed and this was correlated to orientational correlation (ξ) [70]. High temperatures speed up the kinetics of the block copolymer system and lead to a long-range ordering in orientational correlation which remarkably reduces the ordering time [65–67]. Further increasing the temperature results in the degradation of polymer chain and lead to the disarrangement of the blocks. Figure 2.7 (a) shows the variation of ξ with annealing time and the maximum value is corresponding to 270°C. Once the annealing temperature was optimized, the optimization for annealing time and the thickness of film was carried out for the perfectly aligned (vertically) cylindrical domains (shown in figure 2.7 (b & c)). Annealing time $t < 300s$ is sufficient to form organized cylinders without any defects. When the thickness $t < 10$ nm, the formation of droplets were observed. The reason may be attributed to the high surface tension of diblock copolymer which leads to the formation of droplets on annealing at high temperatures. On increasing the thickness, mixing of the droplets leads to the hexagonal arrangement of cylindrical domains up to $\sim$ 200 nm and then increasing more thickness the disarranged cylinders were obtained, due to decrement in correlation length.

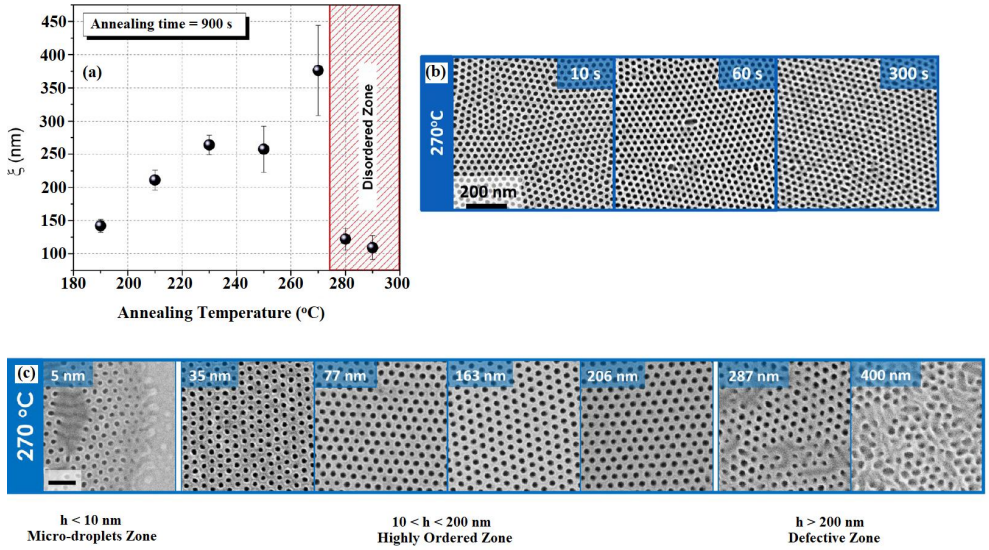

Fig. 2.7 (a) Variation of correlation length with annealing temperature, (b) Time evolution of lateral ordering at an annealing temperature 270°C, and (c) Thickness dependence of lateral ordering annealed at 270°C [69]

.

2.3.2 Solvent annealing

Besides the thermal annealing, solvent annealing is another commonly used approach for the self-assembly of block copolymer thin films. In solvent annealing, the thin films of block copolymer or supramolecules is placed in a closed glass jar having the reservoir of solvent for a particular period of time [71, 72]. Annealing solvent in jar evaporates and eventually the vapours get saturated. Then, thin films are to be removed from the jar and get dried in air. The thin films can be dried by purging N_2 also to remove the excess amount of solvent [73]. The copolymer blocks get swollen by the vapours of the annealing solvent and the thickness of block copolymer increases and copolymer blocks rearranged accordingly. After removing from the jar, the thickness of film again comes to the original value. Many novel set ups for several purposes have been proposed; solvent annealing assisted by thermal or microwave to reduce the annealing time, set up for localized solvent annealing which could be done by using a vapour nozzle, use of polymer gel pad swelled by annealing solvent for the ultra-fast annealing over large areas [74–79]. The reasons for adopting the solvent annealing over thermal annealing are;

1. It provides a path to reconcile the interfacial energies (polymer-substrate and polymer air) and promotes the perpendicular orientation of microdomains [71, 80–82] .

2. It lowers the T_g of block copolymers, so, it induces the self-assembly even of the thermally unstable block copolymer [83].

3. It is appropriate for block copolymers with large molecular weights also. As it reduces T_g, that enhance the chain mobility and then the mass transport is obtained which is not possible in thermally annealed system [84, 85].

4. Provide an additional control to the process by varying the solvents with different selectivity, rate of evaporation of solvent, annealing time [55, 86–88].

Additionally, for supramolecular assembled system, solvent annealing is preferable than thermal annealing because the thermal annealing may evaporate the small molecules. A little loss of small molecules may result the great variation in the morphology of supramolecular complex. The understanding of phase behaviour of block copolymer thin films is more complicated in solvent annealing than that of thermal annealing. Selectivity of the solvents is a key parameter that affects the phase behaviour. A non-selective solvent swells the copolymer with the same amount while the selective solvent swells the copolymers blocks differently which induces the change in relative volume fraction. The effective interaction parameter χ_{eff} will also be influenced in the presence of the selective solvent; it may be smaller or higher than χ. Generally, the solvents are removed after the solvent annealing, and then

dried. The process of removal of solvent may also affect the morphologies in the dried block copolymer thin films. So, basically, the solvent annealing process consists of two steps; swelling and drying. Phase segregation of microdomains may occur at any one of two stages; microdomains may be phase separated in a swollen state and gets affected by drying or microdomains may not be phase separated and are in disordered state and gets phase separated during drying. However, the connection between the nanostructures formed in swollen state and dried state is not well-established [60]. Recently, Bai *et al.* have in-situ studied the swelling and the microdomain orientations in PS-*b*-PDMS 16 kg/mol (with a period of $\sim$18 nm) thin films during solvent annealing using GISAXS [89]. Thin films were annealed in a non-selective solvent of a mixture toluene : heptane :: 5:1 and observed the swelling ratio with annealing time. Swelling ratio is defined as the ratio of the film thickness in swollen state to the thickness of as-deposited film. Cylindrical domains were obtained at lower swelling ratio and the in-plane cylindrical domains were promoted because of the preferential interaction of PDMS with the substrate. The transitions from short cylinders to out of plane cylinders and then in-plane cylinders with the annealing time were observed. They also observed the effect of vapour pressure on the swelling ratio and measured the critical value of swelling ratio (SRc) where the well-ordered cylinders were obtained at particular vapour pressure. Further the effect of thickness (28 nm -1141 nm) on the structural arrangement was investigated in the regime of swelling ratio below SRc. Thinner films led to the in-plane cylinders while thicker films show the well-ordered perpendicular cylinders. The selectivity of solvents causes the change in the orientation of the nanostructured domains [49, 55]. Stamm *et al.* have demonstrated the transition in the orientation of P4VP cylindrical domains from horizontal to perpendicular alignment. PS-*b*-P4VP/HABA thin films were annealed in the vapours of chloroform and 1-4 dioxane respectively [49]. Chloroform and 1-4 dioxane hydrogen bonded with P4VP by phenolic and carbonyl group respectively. The P4VP cylinders dispersed in PS matrix were aligned parallel to the substrate and switched the orientation to vertical to the substrate. This switching of orientation is attributed to the difference of substrate interfacial energy of P4VP/HABA in the presence of each solvent. They have shown the similar results for solvents 1-4 dioxane and mixture of toluene and THF (80:20) shown in figure 2.8 [90].

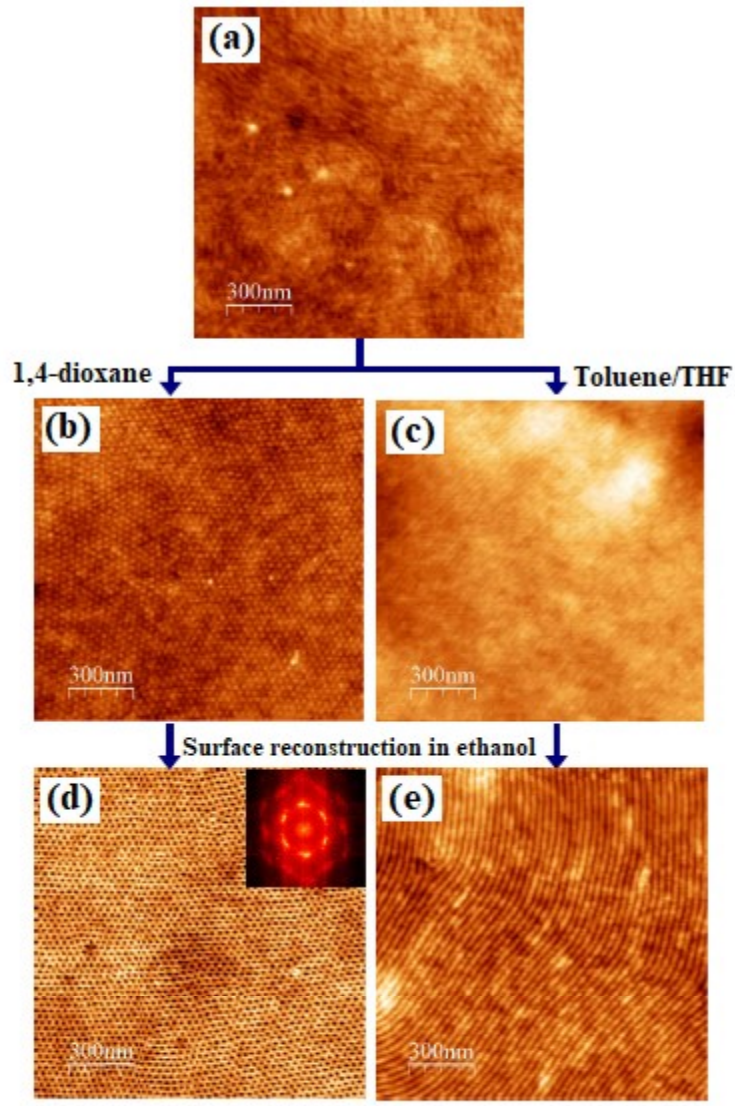

Fig. 2.8 AFM images of as-deposited PS-*b*-P4VP thin film (a), before (b) and after (d) surface reconstruction of thin film annealed in the vapours of solvent 1-dioxane, and before (c) and after (e) surface reconstruction of thin film annealed in solvent toluene/THF [57]

2.4 Thickness dependent morphology

When the thin film of block copolymer is deposited with a thickness on the nanoscale, the morphology of the film critically influenced by the thickness of the film and the interaction of the copolymers with at interfaces [91]. The thickness of film and the periodicity (L_o) in the block copolymer correlates with each other and causes to the final morphology. When the thickness of the film commensurate with L_o, a series of alternating nanostructured domains obtained, while incommensurate thickness with L_o leads to the formation of islands and holes on the surface to balance the surface energies. The films with thickness of film less than L_o incur the complicated ordering due to entropic loss. Many research groups have demonstrated

the different morphologies with the variation in thickness [92–94]. Usually, spin coating and dip coating techniques have been adopted for the deposition of thin film. The thickness of film depends on several parameters; spinning speed, spinning time, withdrawn speed in dip coating, concentration and viscosity of block copolymer solution. Hua-Yan *et al.* have deposited the thin film of PS-*b*-P4VP (45.6 kg/mol) by spin coating by varying the concentration of the solution from 1 mg/ml to 4 mg/ml and keeping the spinning speed and spinning time constant [94]. The films were annealed isochronally in the vapours of 1-4 dioxane for different time. Thickness of film was estimated as 20 nm, 27 nm and 100 nm for the concentration of 1 mg/ml, 2 mg/ml, and 4 mg/ml respectively. Different annealing time is required to obtain the well-ordered cylindrical domains for different thickness of film. Bazuin and co-workers have investigated the morphological evolution of supramolecular assembly of block copolymer PS-*b*-P4VP ($\sim$ 30 wt% P4VP) with the low molar mass additives 1-naphthol (NOH), and 1-naphthoic acid (NCOOH) [93]. Supramolecular assembled thin films were deposited using dip coating technique by varying the dip-coating rate in the capillary regime (low rates). It was observed that the striped morphology transformed into dotted morphology with decreasing the dip-coating rate (figure 2.9 (a & c)). The stripe morphology was corresponding to the minimum film thickness which corresponds to the brush copolymer regime. Further they extended this study in their next report to the variation of dip-coating rate over a wide range (1 mm/min to 100 mm/min) [93]. The overall understanding of thickness variation with the dip-coating rate has already well explained by D. Grosso and it shows that thickness varies in V-shape with dip-coating rate [95]. Thickness of the films initially decreases, reaches to a minimum value and then increases with dip-coating rate (shown in figure 2.9 (b)). In addition to the thickness they have also investigated the effect of concentration of solution, small molecule uptake ratio, molar ratio of additives and the types of additive (hydroxyl and carbonyl linking) on the morphology.

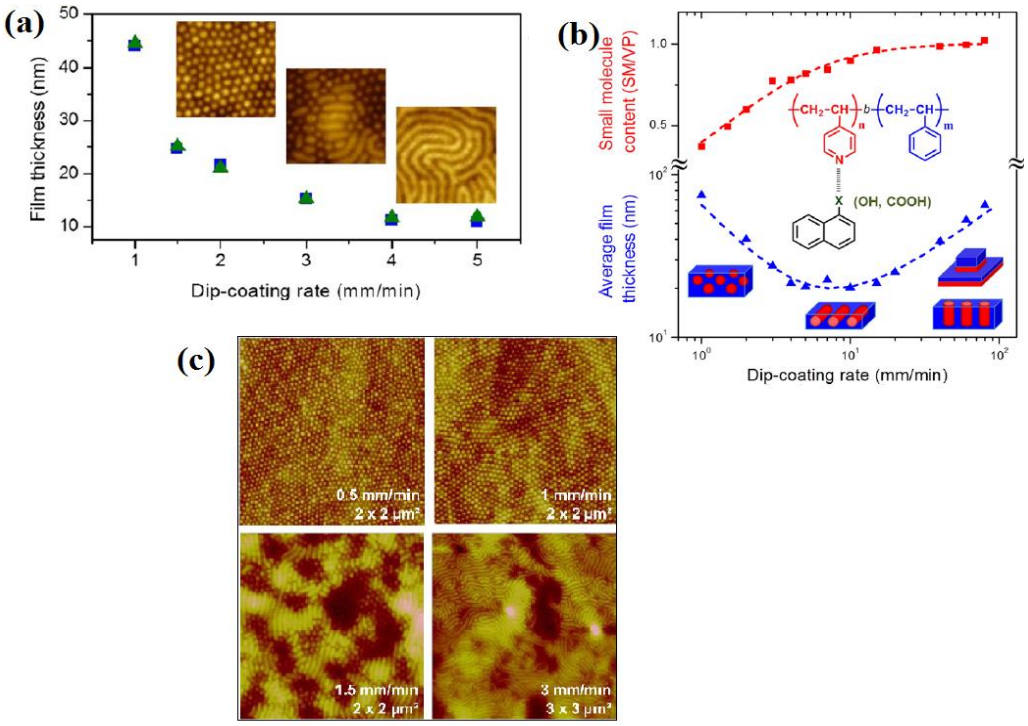

Fig. 2.9 (a) Variation of thickness of PS-*b*-P4VP thin films along with the morphology in capillary regime (low dip-coating rate) (b) Variation of thickness as well as small molecule content with dip coating rates over a wide range, and (c) AFM images of the morphology of PS-*b*-P4VP (NCOOH) (NCOOH:P4VP 1:1) with different dip coating rate (mentioned in the figure) [93, 93]

2.5 Nanostructures by block copolymers

The ordering in the thin films have been discussed in the previous section which is a part of the fabrication of ordered nanotemplates. Now, for the fabrication of ordered nanostructures the following steps are to be addressed;

1. Creation of porous structures by removing one of the blocks selectively (nanotemplates).
2. Selective deposition of the inorganic material in the nanotemplates.
3. Removal of remaining polymer matrix.

2.5.1 Preparation of porous nanotemplates

In order to prepare the nanotemplates, one of the blocks has to be removed selectively and different methods have been adopted to remove the one of the blocks depending on the chemical nature and stability of block copolymer. Deep UV exposure (25 J/cm^2 dosage) followed by rinsing with acetic acid have been widely used to remove the PMMA block from PS-*b*-PMMA block copolymer thin film. UV exposure degrades

the polymer chains in PMMA block while it provides the crosslinking in the polymer chain of PS, so that PS can sustain while removing the PMMA block using acetic acid [96]. Ozone treatment have been adopted for the removal of PI or PB block from PS-*b*-PI or PS-*b*-PB respectively [16]. Chemical dissolution is the easy process and can be used for various copolymer blocks, for example; PDMS block from block copolymer PS-*b*-PDMS can be removed by the degradation using HF solution [97], hydrolysis process has been applied to PLA containing block copolymers to remove PLA block [98], and the rinsing in ethanol/methanol has been applied to remove the P4VP block from most commonly used block copolymer PS-*b*-P4VP [49, 94]. Reactive ion etching (RIE) process has also been used for the selective removal of one of the blocks in which the nanoporous templates are generated by increasing the oxygen or decreasing the carbon atoms in the one of the blocks [49].

2.5.2 Deposition of inorganic material into the nanotemplates

Metallization

Conducting and semiconducting nanowires have the great potential to be used in the optoelectronic applications. Metallization is an easy and cost-effective process to obtain the metallized nanowires from block copolymers. It is the electro less process that means no catalyst or electrolytes are required which reduce the tediousness and cost as well. Fahmi *et al.* have demonstrated the process for the Pd nanowires from PS-*b*-P4VP block copolymer [99]. It has been well reported that the metals interact well with the pyridine functional group of P4VP which is key point in the metallization process. So, PS cylinders dispersed in P4VP lamellae is the basic requirement for the fabrication of nanowires. PS-*b*-P4VP (PDP) thin films was converted to PS nanofibers lined with the P4VP functional groups by removing the additive so that free pyridine groups can be available to capture the metal ions. Metallization was ocurred by the reduction of $Pd(CH_3COO)_2$ in the aqueous solution of $(CH_3)_2NBH_2$. The same process can be applied to the other metals also like Ag, Ni, Au which possess the great affinity towards the pyridine group of P4VP. The diameter of the nanowires can be controlled by diameter of PS nanofibers as well as by the reaction conditions. CdSe nanowires were also synthesized by the same PS nanofibers but in this case, CdSe nanoparticles of average size of 2 nm were used. Intercalation of metals with pyridine works as inorganic-organic junction. Figure 2.10 shows the schematic representation of synthesis of Pd and CdSe nanowires from the self-assembly of PS-*b*-P4VP (PDP).

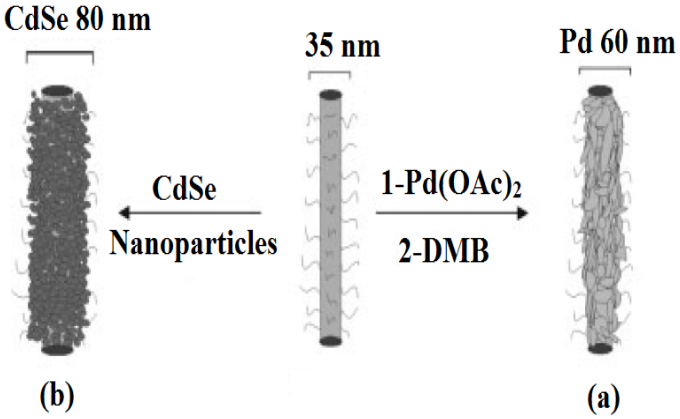

Fig. 2.10 Schematic for the synthesis of Pd, and CdSe nanowires by metallization process, PS nanofiber is shown in the middle, (a) represents the Pd nanowire, and (b) shows the CdSe nanowire [99]

Template assisted sol-gel method

Semiconducting nanostructures (especially TiO_2) are of great interest for the photovoltaic applications. Sol-gel method have been widely used for the backfilling of the nanotemplates to develop the well-ordered semiconducting nanostructures. Though, metal oxide nanorods have been synthesised by alumina template-assisted sol-gel method but block copolymer nanotemplates provides the more controllability to the diameter of the nanorods or nanodots [100]. For the fabrication of metal/metal oxide nanostructures, the metal/metal oxide precursor solutions need to be impregnated into the porous templates either by immersing the template into the sol or by using spin coating or dip coating technique. Raulet *et al.* have prepared the ordered array of metal oxides nanoparticles (TiO_2, RuO_2, SiO_2, ZnO, MnO_2 and CeO_2) by spin coating the precursor solutions at a speed of 3000 rpm for 30 sec [101]. Figure 2.11 shows the schematic representation for the fabrication of metal oxide nanostructures by block copolymer template assisted-sol-gel method. The filling of the templates can be tuned by the spinning speed and spinning time.

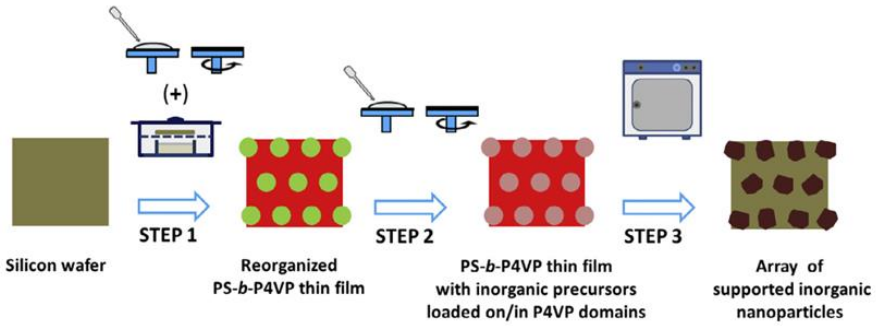

Fig. 2.11 Process flow for the fabrication of ordered array of metal oxides nanoparticles [101]

Removal of templates leads to the ordered metal oxide nanoparticles (characterized by SEM) shown in figure 2.12.

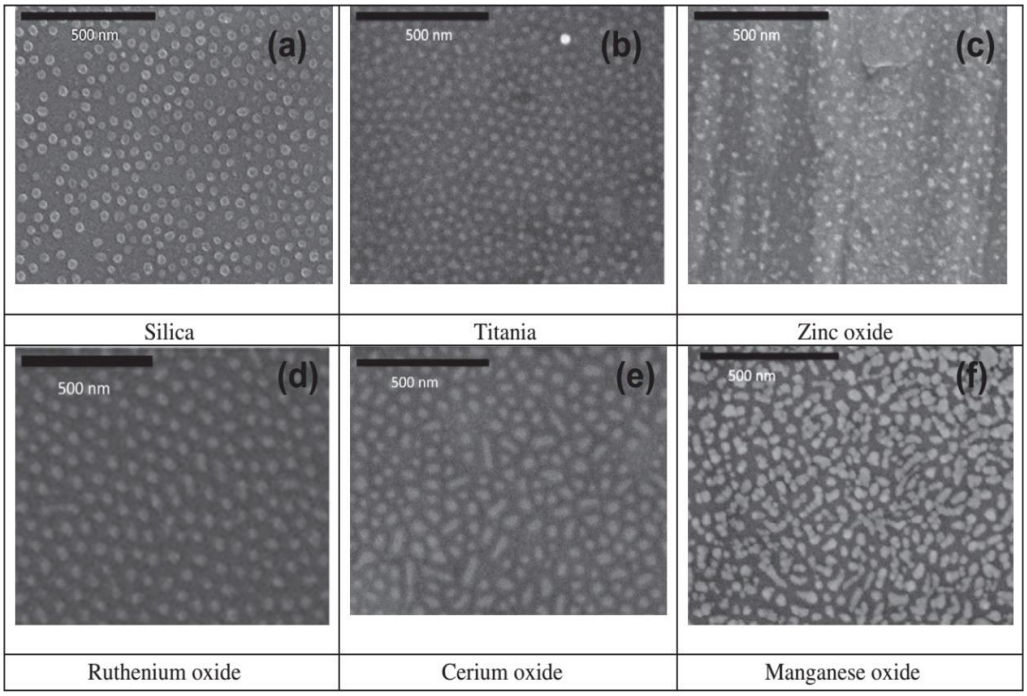

Fig. 2.12 SEM images of metal oxide nanoparticles [101]

Above-mentioned way of backfilling the pores might have an issue of forming a continuous layer over templates instead of the selective deposition. In that case, the overlayered metal oxide has to be removed by using ion etching techniques. So, in the same direction, another way of fabrication of ordered nanostructures by template assisted sol-gel method is the incorporation of metal ions of the precursors in one of the blocks of block copolymer solution. The metal oxide precursor selectively reacts with the P4VP phase. Deposition of thin film of composite solution followed by polymer removal left the the substrate decorated with metal oxide nanoparticles [102]. The ordering of the nanoparticles deposited on the substrate can be tuned by varying the precursor concentrating loading to P4VP [103, 104]. Two dimensional array of TiO_2 strings have also been obtained by the micellar solution of block copolymer [105].

Direct deposition of nanoparticles

Direct deposition of the pre-synthesized nanoparticles into the templates offers the flexibility to tailor the properties of nanoparticles in advance. Moreover, the nanoparticles can be selectively deposited into the pores and the formation of a layer of metal oxides over the template, (case of sol-gel method) can be avoided. This approach is easy as compared to sol-gel method because a number of the reaction parameters need to be optimized for the fabrication of well-ordered nanostructures

in sol-gel method.

As the pores are functionalized with pyridine group of P4VP in the nanotemplates, the nanoparticles can be directly deposited or may be functionalized depending on their reactivity with the pores. Stamm's group and the other researchers have published several reports on fabrication of metal nanoparticles array by direct deposition of nanoparticles into the pores [106–111]. The whole process of the fabrication of well-ordered nanoparticles array is depicted in figure 2.13. Magnetic nanoparticles (Fe_3O_4) were also deposited by this approach without any surface modification to the nanoparticles [112]. The deposition of nanomaterials on the substrate is also possible without removing one of the blocks. Nanoparticles can selectively bind with one of the blocks. The concentration of the nanoparticles loading to the block copolymer solution governs the fidelity of the nanoparticles deposited with the block copolymer morphology. Barandiaran *et al.* have synthesised the PS-*b*-P4VP/(Fe_2O_3) nanocomposites by using this approach [113]. However, the array of TiO_2 nanostructures by the deposition of pre-synthesized nanoparticles is yet to be explored.

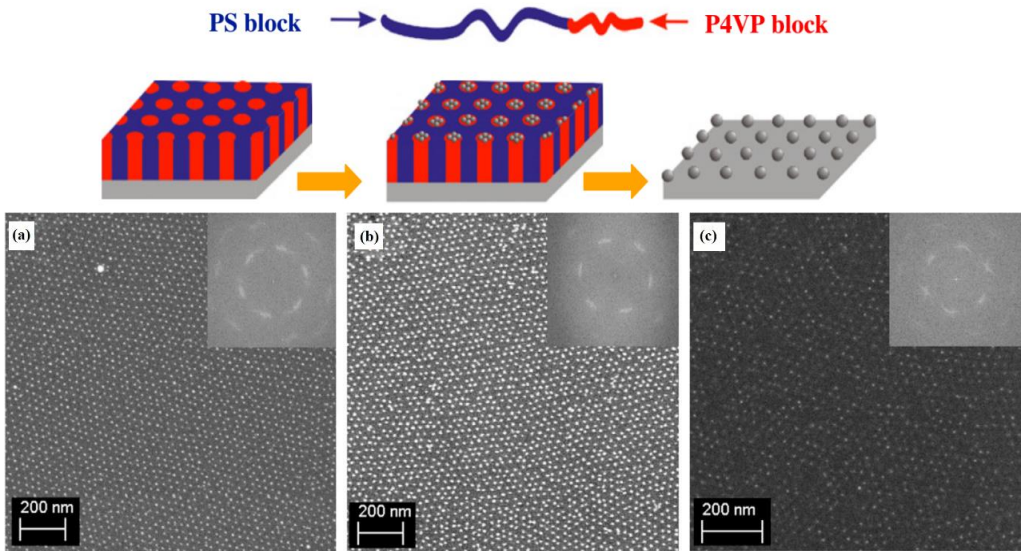

Fig. 2.13 Scheme for the fabrication of ordered array of nanodots (top) and SEM images of the ordered array of metal nanodots (a) Au, (b) Pt, and (c) Pd. Inset shows the FFT of the image [111]

Removal of remaining polymer matrix

Polymer removal is the last step of the process of the fabrication of ordered nanostructures. Polymer matrix can be removed by many ways depending on the nature of copolymer and the deposited material like, RIE, UV irradiation, dissolution, plasma etching (oxygen or oxygen/ozone mixture), and pyrolysis [107, 111, 114–116]. Pyrolysis involves the degradation of polymers at high temperatures. For TiO_2 nanostructures, heating at high temperature leads to the transformation from amorphous

to crystalline behaviour while Au nanoparticles undergo the thermal coarsening due to recrystallization at high temperature. So, the choice of method for removal of polymer matrix depends on the deposited materials and its application.

2.6 Applications of block copolymers

2.6.1 Nanopatterning

Nanopatterning is one of the promising applications of the block copolymers. Ruiz *et al.* have used the PS-*b*-PMMA block copolymers self-assembly to increase the density of array of patterning and also to improve the quality of pattern, already developed by e-beam lithography [117]. PMMA block was removed and 7 nm of Cr was evaporated. PS mask was removed using piranha solution, leaving the array of Cr dots on the substrate. Then, 20 nm Si pillars with a density of $\sim$1 Tb/in^2 were obtained on the substrate using the RIE (CF_4). Cheng et al. have prepared the array of Co nanodots by using PS-b-PFS block copolymer as an etching mask [118].

2.6.2 Membranes

The cylindrical and gyroidal morphologies of block copolymers can be used as nanoporous membranes. The narrow pore size distribution due to the self-assembly of block copolymers makes these membranes more advantageous like in virus filtration. Yang *et al* [119]. have fabricated PS-PMMA membranes with average pore diameter of $\sim$18 nm (figure 2.14 (a)). This type of membranes offer the high selectivity and high flux for in-filtration of virus. Block copolymer provides the high porosity and the supported membranes gives the mechanical stability. The authors have investigated that the passage for human rhinovirus (HRV 14) with an average diameter of $\sim$ 30 nm was completely blocked due to the uniform pore-size of membranes. It also maintains a high flux compared to track-etched PC membranes with the nearly same pore size. Plaque assay test was also performed and it was observed that none of HRV 14 passed through the membrane (figure 2.14 (b)). But these membranes were not mechanically stable at high filtration pressure. Tang *et al.* have prepared the PS-PMMA membranes with relatively high thickness of $\sim$ 160 nm [120].
Abetz *et al.* demonstrated a one-step process for the fabrication of nanoporous PS-*b*-P4VP membranes by non-solvent induced phase separation of block copolymers [121]. This process is suitable for scale-up nanofabrication. Membranes with uniform pore size provided by self-assembly of block copolymer can be explored for the application of protein drug delivery. It can be beneficial to minimize the denaturation of protein drugs.

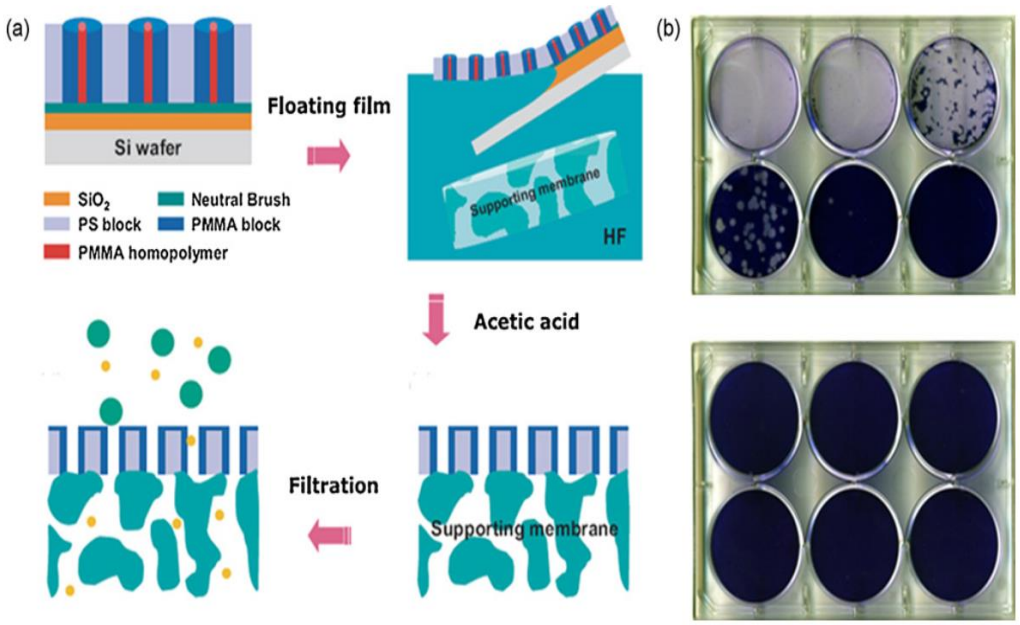

Fig. 2.14 (a) Schematic representation of the process for the fabrication of block copolymer based membranes, and (b) Plaque assay test, before filtration (top), and after filtration (bottom) [119]

2.6.3 Photovoltaics

Solar energy conversion, one of the renewable energy source, can be seen as a major contributor to eliminate the mankind's dependency on fossil fuel sources. New technological advancement is required to use the full potential of solar energy in photovoltaics. Block copolymer provides a platform for investigating the connectivity among the morphological, structural properties and PCE of device. Topham *et al.* have reviewed the benefits of the block copolymers in photovoltaic energy conversion [122]. Interest in the organic photovoltaics has been increasing due to their light weight, flexibility which makes them easily portable, and most importantly, cost-effective. The mechanism of an organic solar cell (OSC) mainly consists of three steps (i) absorption of photons; generation of coulombically bound electron-hole known as excitons, (excitation from HOMO to LUMO) (ii) migration of these excitons towards the donor-accepter interface; dissociation of excitons into charge carriers (electron, hole) at the interface, (iii) transportation of charge carriers to their respective electrodes [123]. The mechanism is shown schematically in figure 2.15. Dissociation of excitons is limited to exciton binding energy and exciton diffusion length. As the block copolymers self-assembled into various structures on a nanometer scale (or on the scale of exciton diffusion length), so, PCE of OSCs is expected to be enhanced in block copolymer based solar cell. Block copolymers can be used in the OSC in two ways; as active materials or structure directing agents.

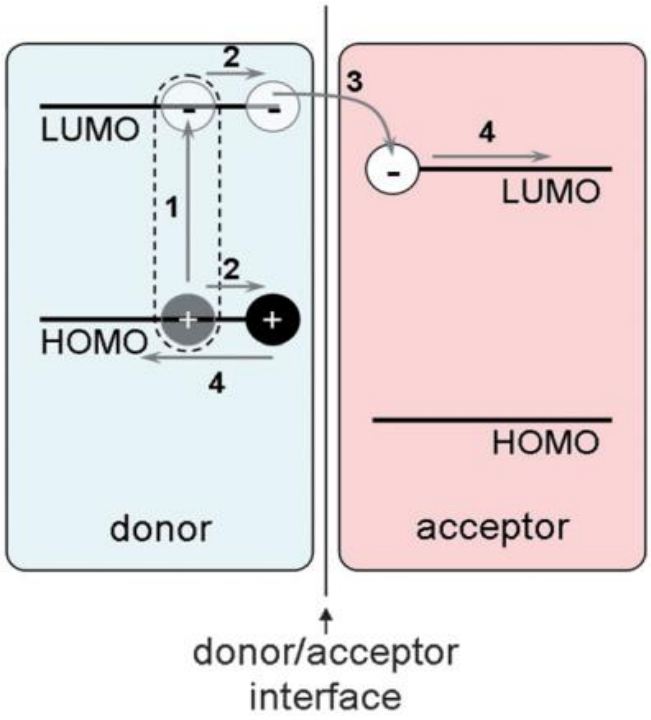

Fig. 2.15 Schematic depiction of working of OPV process. 1 represents the creation of excited excitons by absorbing the incident photon, 2 shows the migration of excitons to the donor-acceptor interface, 3 is the representation of dissociation of excitons into electron and holes, and 4 shows the transportation of electrons and holes towards the electrodes [124]

Block copolymers as active materials

Initially, the OSCs were fabricated with a bilayer concept; p-type and n-type. High PCE was not achieved because of the loss of excitons before reaching to the p-n junction. Then, the concept of bulk heterojunctions was introduced (polymer blends), and the issue of exciton loss was resolved up to some extent. But these blends showed the random phase separation of the donor and acceptor. Therefore, very large domains cause to exciton loss, while very small domains can be responsible for charge recombination. Ordered heterojunctions on few nanometer lengths in the active layer were supposed to overcome the issue of exciton loss and charge recombination which can be easily provided by block copolymers. One can imagine a block copolymer comprised of p-type copolymer (donor) and n-type copolymer (acceptor) as the active material. This journey from bilayer to ordered heterojunctions in active layer is represented in the figure 2.16. Meyers and co-workers first proposed the use of block copolymers in optoelectronics [125] and experimentally pioneered by Jenekhe *et al* [126]. Several groups have studied the rod-coil block copolymer system comprised of P3HT and a polyacrylate with perylene bisimide pendant groups [127, 128]. These materials provide the crystallinity required for high charge carrier mobility.

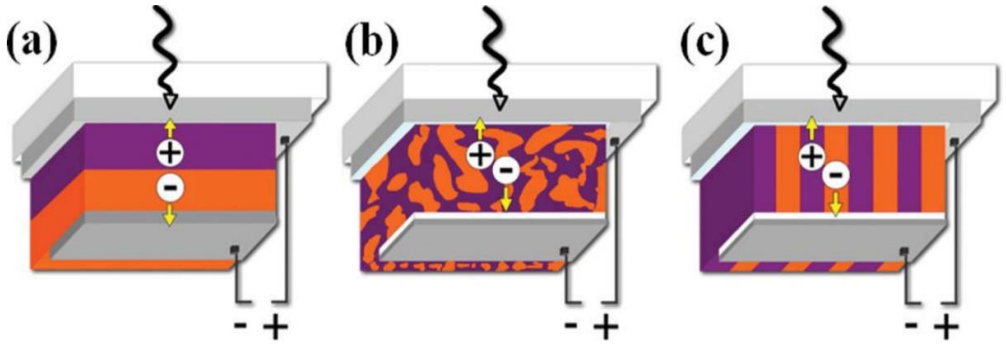

Fig. 2.16 Representation of OSC (a) bilayer, (b) bulk heterojunction, and (3) block copolymer based heterojunctions [122]

Block copolymers as structure directing agents

Instead of using block copolymers directly as active materials, it can be used as a template for the inorganic materials suitable for solar cell applications. For hybrid solar cells, including DSSC, metal oxides are most promising materials. Among various metal oxides TiO_2 has been widely used because of i) its wide band gap; transparent to the visible region, ii) suitable matching of energy levels with organic semiconductors. Additionally, nanostructured TiO_2 helps in the better transportation of charge carriers to electrodes. High surface area is a key parameter for enhancement in PCE of solar cell. For this purpose, mesoporous TiO_2 was synthesised and DSSC was fabricated with the mesoporous TiO_2 by Chen *et al.* [129]. The size and shape of the mesoporous TiO_2 was tuned by varying the concentration of Ti source, and sequence of adding TiO_2 precursor and H_2O. The size and interparticle distance can be tuned more efficiently using the synthesis process assisted by the block copolymers. Many groups have synthesized the mesoporous TiO_2 using block copolymers by selective incorporation of TiO_2 precursor into one of the blocks of the block copolymer with more controlled size and spacing between them [130, 131]. The other nanostructures like nanorods can also be fabricated by this approach using cylindrical block copolymer thin films with perpendicular alignment. Another approach for the ordered nanostructures, the creation of templates and backfilling of the pores, can be used to obtain the well-ordered nanostructures as discussed in section 2.5.2. These nanostructures were found to be beneficial for both, the photo electrode as well as active layer. Allen *et al.* have synthesized ordered alumina nanoparticles using PS-PMMA block copolymers and integrated into buffer layer (TiO_2) in PSC in conjugation with active materials P3HT:PCBM [39] (figure 2.17).

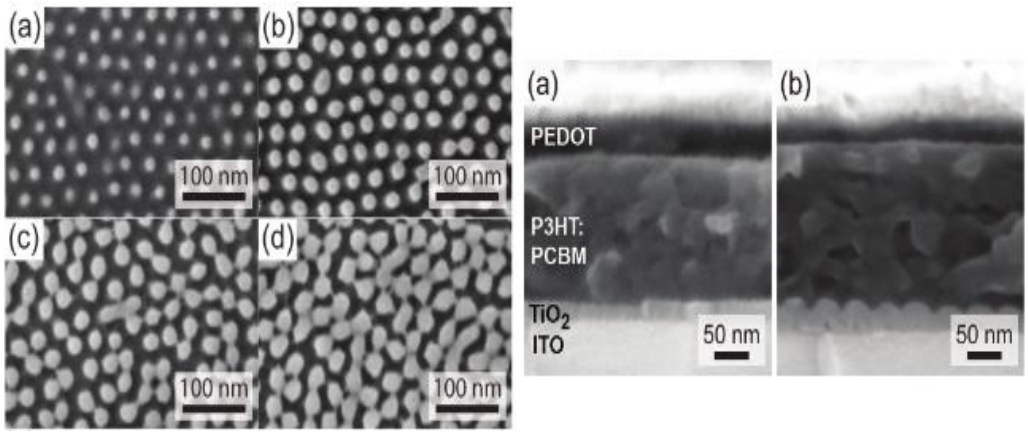

Fig. 2.17 SEM images of alumina nanoparticles with cycle of exposure of alumina precursor (a) 3, (b) 6, (c) 9, and (d) 12 cycles (left). Cross-sectional view of device (a) without, (b) with alumina nanoparticles (right) [39].

The height of the nanoparticles were controlled by the exposure of alumina precursor. The enhancement in PCE was found to be 25% which was mainly attributed to increment in the absorption due to scattering from nanoparticles. Many researchers have demonstrated the enhancement in PCE of hybrid solar cell (polymer/metal oxide) using the metal oxide nanorods, and nanotubes [35, 132]. Recently Seo *et al.* have fabricated the perovskite solar cells integrated with vertically oriented TiO_2 nannorods and nanowalls [38]. TiO_2 nanorods nnd nanowalls were synthesized by vertically oriented PS-*b*-PMMA block copolymer thin films with cylindrical and lamellar domains respectively (figure 2.18). As, TiO_2 is a promising material for solar cells, so TiO_2 nanostructures synthesized by block copolymer self-assembly approach can further be explored in this field.

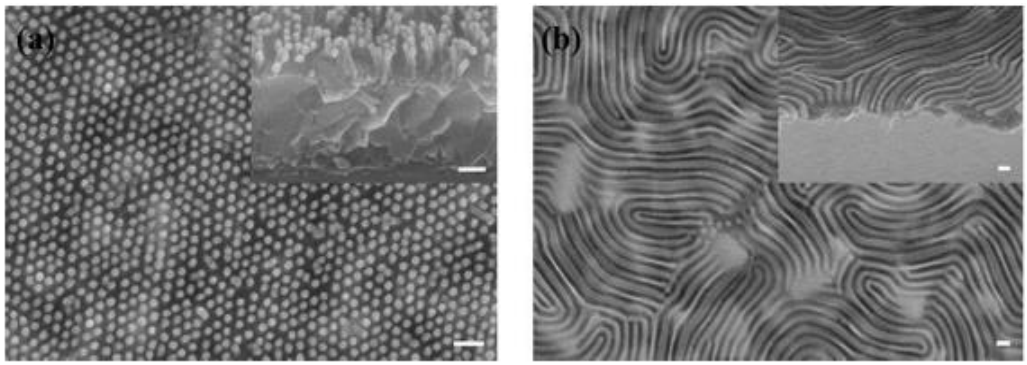

Fig. 2.18 FE-SEM images of (a) TiO_2 nanorods, and (b) TiO_2 nanowalls. Insets are the cross-sectional view [38]

2.7 Conclusions

Literature survey about the variety of morphologies of block copolymers and their self-assembly have been discussed. The materials and the methods for the synthesis

of block copolymer thin films were also introduced. The research reports published by many researchers revealed that the supramolecular assembly of block copolymer is an efficient approach for the nanopatterning and fabrication of functional nanomaterials. Functional nanomaterials have their own advantages in various applications. It was also revealed that the ordering in thin films of block copolymers can be improved by thermal and solvent annealing. There are several other factors that affect the morphological behaviour and orientation of domains like thickness of film, content of small molecules or additives, type of additives etc. Few applications of the block copolymers (nanopatterning, membranes and photovoltaicshave) have also been discussed. Tuneable size of the pores in the block copolymer membranes make them beneficial for the virus filtration. For the photovoltaic applications, block copolymers act as either active material or structure directors or both. In the end, it can be concluded that metal oxide nanostructures shows the improvement in the PCE of solar cells and block copolymers provides the plenty of morphologies that can be used for the fabrication of metal oxide nanomaterials.

Chapter 3

Materials and Methods

3.1 Introduction

The present thesis deals with the formation of ordered TiO_2 nanodots using the block copolymer nanotemplates. Nanostructures have been potentially used in various area of applications like photovoltaic devices, memory devices, batteries, and gas sensing. Various routes have been employed to synthesis TiO_2 nanostructures (nanorods, nanowires, nanotubes, nanodots) such as sol-gel, hydrothermal, solvothermal, anodization, templating synthesis. Among them synthesis using templates is a very efficient and easily controlled approach which gives the highly-ordered nanostructures with a tunability of their size and the periodicity. Block copolymer nanotemplates shows very interesting and easily tailored morphologies. The synthesis of block copolymer thin films, TiO_2 nanoparticles and the fabrication of TiO_2 nanostructures have been discussed. Characterization techniques are very important part of the research work to understand the properties of the materials and their applications. This chapter describes the experimental and instrumental details for the synthesis and investigating the properties.

3.2 Materials

Chemicals and materials used in this work were as follows: for the synthesis of TiO_2 nanoparticles Titanium tetra isopropoxide (TTIP) ($Ti(OC_3H_7)_4$, 99.5 %, Sigma Aldrich), Hydrogen peroxide (H_2O_2, 30% w/v, RANKEM), Ethanol (C_2H_5OH, Merck), and 1-thioglycerol ($C_3H_8O_2S$, purity $> 97\%$, Sigma Aldrich) were used. Si wafer (p-type (100), Mcwin India), ITO coated glass sheet (sheet resistivity $\sim$15 $\Omega/\square$, Mcwin India), and ITO coated PET (sheet resistivity $\sim$16 $\Omega/\square$, Sigma Aldrich) were used as substrates. Substrates were cleaned using Dichloromethane (Fisher Scientific), Isopropyl alcohol (IPA) (Merck), Ammonia Solution (NH_4OH, 25%, Merck), and Hydrogen peroxide. For the fabrication of nanotemplates diblock copoly-

mer poly(styrene)-*b*-poly(4-vinylpyridine) (PS-*b*-P4VP) with the molecular weights of M_n = 39.9 kg/mol, (M_n^{PS} = 35.5 kg/mol, M_n^{P4VP} =4.4 kg/mol, polydispersity index (PDI) = 1.09), M_n =41 kg/mol, (M_n^{PS} =33 kg/mol, M_n^{P4VP} =8 kg/mol, PDI = 1.10) and M_n =205 kg/mol, (M_n^{PS} =130 kg/mol, M_n^{P4VP} =75 kg/mol, PDI = 1.25) were purchased from Polymer Source Inc. Canada. 2-(4-hydroxyphenylazo) benzoic acid (HABA) (> 98%, Sigma-Aldrich) and 1-4 dioxane (Merck) were used as additive and solvent respectively. 1-4 dioxane was used as annealing solvent also. 0.2 μm PVDF syringe filter (Whatmann) was used to filter the block copolymer as well as nanoparticles solution. To characterize the TiO_2 nanoparticles by FTIR the pellets were prepared using Potassium bromide (KBr, Sigma aldrich)as a binder.

3.3 Cleaning of substrates

Cleaning of the substrates is an important factor which affects the quality of film deposited. All the substrates were cut with the dimension of 20 mm × 10 mm. Before the deposition of the thin films of block copolymers, the substrates were thoroughly cleaned by following procedure:

3.3.1 Cleaning of Si wafers

Firstly, substrates were cleaned by sonication in dichloromethane for 15 minutes and after each step the wafers were in rinsed in DI water. Subsequently, the wafers were cleaned in a mixture of ammonia, hydrogen peroxide and water (NH_3: H_2O_2: H_2O :: 1:1:2) at 70°C for 90 minutes. This mixed solution is very corrosive so it should be handled carefully and not advised to be stored in a sealed bottle. Further, the wafers were rinsed with DI water 5-6 times under sonication and dried.

3.3.2 Cleaning of ITO coated glass

ITO coated glass substrates are commonly used for optoelectronic applications because of their good conductivity and transparency in visible region. ITO coated PET (polyethylene terephthalate) provide the flexibility in addition to conductivity and transparency. Substrates were cleaned in detergent solution (Labolene) with sonication for 15 minutes. Then the substrates were rinsed in DI water 4-5 times and sonication in acetone for 10 minutes. After rinsing in DI water, substrates were cleaned in IPA with sonication for 10 minutes. Again, the substrates were rinsed 5 times in DI water.

3.4 Techniques used to prepare the samples

In the present thesis sol-gel route was adopted for the synthesis of nanoparticles because of its easiness, high yield and low cost. For the preparation of nanotemplates, the thin films of block copolymer were deposited on the substrates by dip coating and lateral ordering was improved by solvent annealing.

3.4.1 Dip coating

Dip-coating is an affluent and fast method for the thin film deposition from the chemical solution. This method provides the great facility to deposit coating on large area with very good control for various technological applications. The working principle for the dip coating can be described as follows; the substrate is to be immerged in the solution tank with user controlled speed and left it for the particular time and then, it is to be withdrawn from the solution with a particular speed (figure 3.1). The immerging and withdrawn speed can easily be controlled. During this dipping process, solution spreads out on the substrate homogeneously due to the basic physical effect of capillary rise and viscous force. Then evaporation process occurs after coating which is responsible for the solidification of the final film which already grown on the substrate. Different evaporation conditions and withdrawal speed are the key parameters for the film quality as well film thickness. So, one has to take care of that carefully.

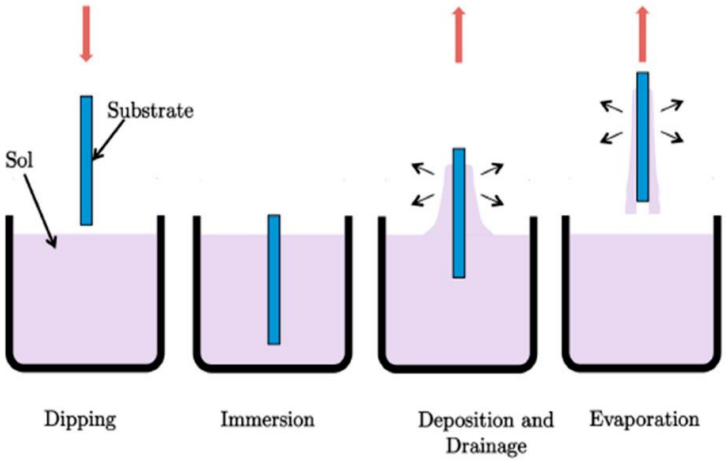

Fig. 3.1 Process flow for the dip coating [133]

.

The whole deposition process may be divided in the following three major steps:

1. Immersion of the substrate into the solution tank.
2. Dwell time for the film deposition.
3. Withdrawal of the substrate from the solution tank.

We have used programmable dip coating system (XDIP-SV1, Apex) in this study with a withdrawn speed of 100 mm/min.

3.4.2 Sol-gel method

Sol-gel is well-known process for the synthesis of nanomaterials which is based on wet-chemical-based self-assembly process. Two major parts are involved in the evolution of the networks through the formation of a colloidal suspension name as sol and other gelation of the sol to form a network in a continuous liquid phase name as gel. The precursors are used for making the colloids which consist of metallic ions and ligands. In general, sol-gel process consists of four important steps:

1. Hydrolysis and alcoholysis
2. Condensation and polymerization process
3. Growth of nanoparticles
4. Agglomeration of the formed nano-particles

All these steps are leading the sol-gel process and depend on various conditions such as temperature of the reaction, pH of the solution, molar concentration and time of reaction etc. By controlling these parameters, one can easily tune the different properties like structural, optical and electrical of the nanoparticles and could be used in various applications. Figure 3.2 represents the process for the synthesis of TiO_2 nanoparticles followed in this thesis.

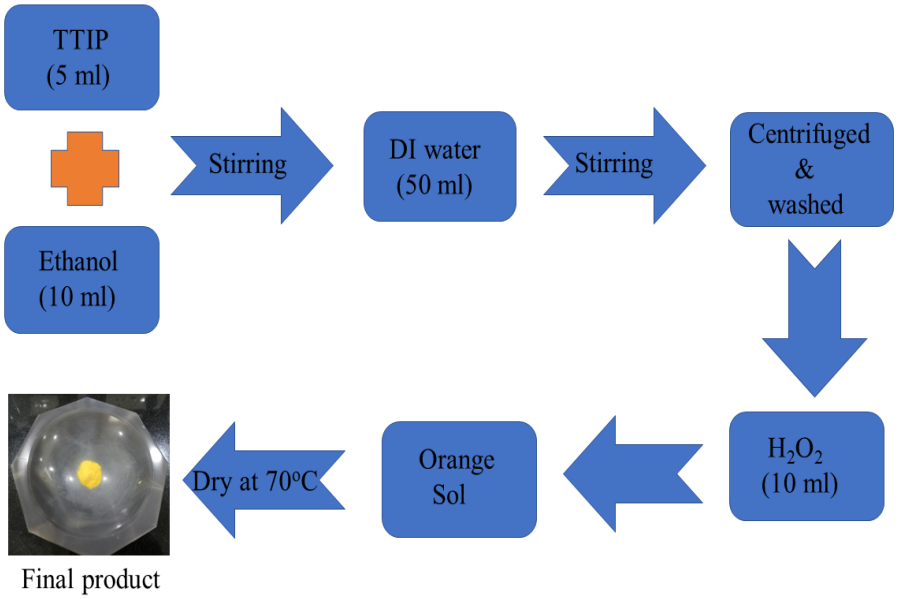

Fig. 3.2 Schematic for the synthesis of TiO_2 nanoparticles.

3.4.3 Solvent annealing

Thermal annealing and solvent annealing are the common process to improve the ordering in thin films of block copolymer. Solvent annealing is considered more advantageous and better than the thermal annealing because in thermal annealing small molecules in the supramolecular assembly may evaporate. Evaporation of small number of molecules may affect the morphology of thin films of block copolymer to a great extent. Solvent annealing is the process in which each copolymer interacts with the vapour of the solvent (selective/non-selective). Ordering in the thin films depends on the affinity of copolymers towards solvent molecules, rate of evaporation of solvent, volume of solvent and container, and time of annealing. Depending on their affinity for the annealing solvent, the copolymers swell with different rate. Thin films were put in a tightly sealed glass chamber along with the annealing solvent in a bottle with some pinhole shown in figure 3.3. The thin films were removed from the annealing chamber after a particular time and solvents were allowed to evaporate.

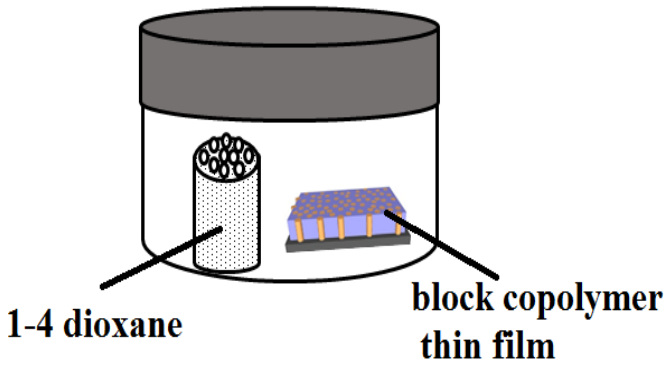

Fig. 3.3 Schematic for the solvent annealing of block copolymer thin film

.

3.5 Techniques used to characterize the samples

3.5.1 Atomic force microscopy (AFM)

AFM has been widely used for the fundamental research, material science, medical science and technology applications. It is suitable characterization tool to investigate for various technological materials including membranes, thin films of polymers and semiconductors etc. [134]. In the AFM, sharp metallic tip interacts with the surface of the material and produce the Vander-Waals force between tip and surface of the sample. This Vander-Waals force could be generated due to short-range repulsive force (in contact mode) or longer-range attractive force (in non-contact mode). In the contact mode (repulsive force), the instrument slightly connects with a tip at the end of cantilever which scan over the sample surface during imaging. During the raster-scan, metallic tip goes along the surface of the material and found the

vertical deflection of the cantilever. These deflections indicate the undulation in the surface of the film. In non-contact mode (attractive force), the metallic tip does not touch the sample surface and gives the topographic images of the material due to attractive forces. In the tapping mode, the cantilever is driven to oscillate up and down close to the resonance frequency due to presence of piezoelectric material which is mounted on the scanner. This mode is very much effective for the scanning of the soft material like polymer and membranes due to its non-destructive nature in comparison of contact mode. Surface damage possibilities are reduced in this mode because tip does not drag across the sample during scanning [135]. Figure 3.4 shows the schematic diagram for the working of the AFM and the force variation with distance between tip and sample. When the cantilever bends due to the surface of the sample, the path of laser beam also deflected which leads to deviation at different angle and these variations perceived by the photodiode. The force between the tip and sample is responsible for the fluctuations in cantilever.

$$F = ks \tag{3.1}$$

Where, k = spring constant and s = bending distance for the cantilever during imaging [134]. The cantilever of the AFM is made up of silicon nitride or silicon material with a very sharp tip (width of few $\sim$10 nm) which provide the facility to observe very high-resolution image on nanometer scale. In the present study, the thin films were characterized by AFM (Bruker) in tapping mode.

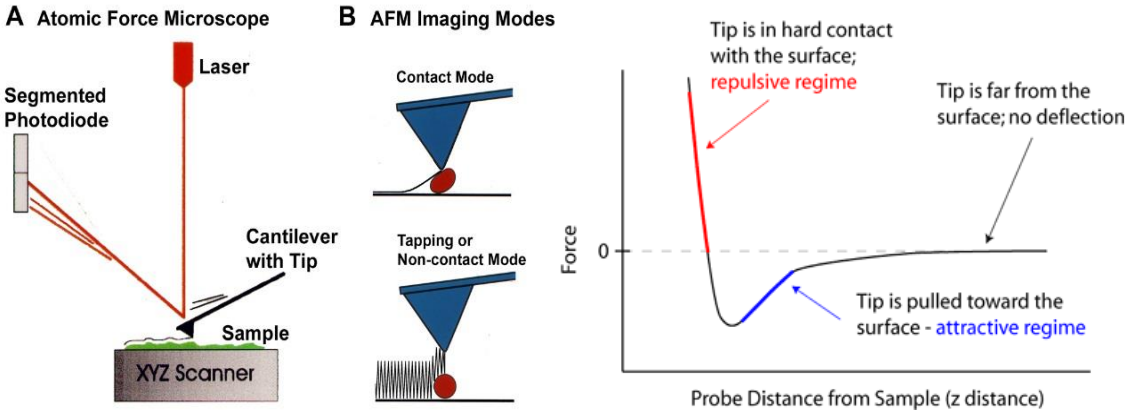

Fig. 3.4 Schematic for working of AFM (left), and Vander walls force variation with the distance between tip and sample.

3.5.2 X-ray diffraction (XRD)

X-ray diffraction is the fundamental tool for determining the structure of the material and widely used for material characterization. When a monochromatic X-ray beam incidents on the material at an angle θ, it gets scattered from the sample (figure 3.5). The scattered beam is detected by the detector and give the crystallographic

information about the lattice structure. The wavelength of the beam is nearly comparable to the atomic size which leads to collect the information about atomic arrangement of the material. If the arrangement of the atoms in the material is in regular manner, then diffracted beam interfere constructively or destructively with each other depending on the path difference. A well-known formula Bragg-relation [136, 137] holds for the condition of constructive interference as in following manner:

$$2dsin\theta = n\lambda \tag{3.2}$$

Where, n = order of reflection, λ = wavelength of incident X-rays, d = interatomic spacing between lattice plane and θ = diffraction angle. The average crystallite size of the nanoparticles can be calculated by the following equation known as Debye-Scherrer's formula [137]

$$D = \frac{0.9\lambda}{\beta cos\theta} \tag{3.3}$$

Where, λ = wavelength of X-rays, β = full width at half maxima (FWHM) of diffracted peak, θ = diffraction angle.

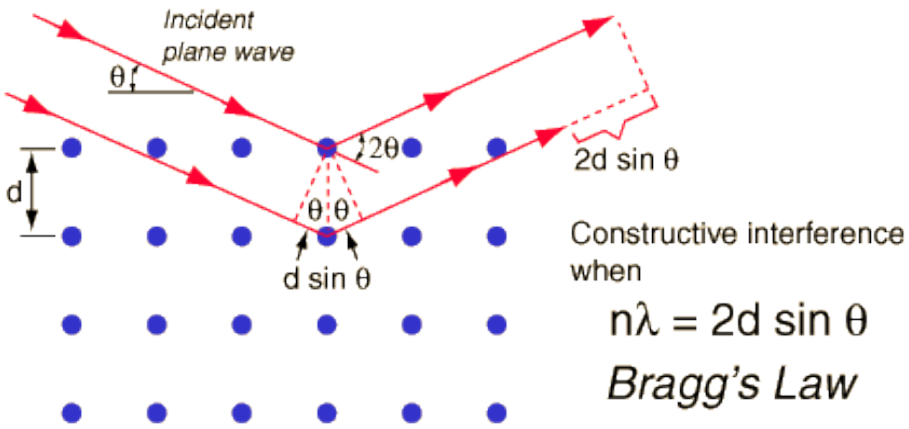

Fig. 3.5 Schematic diagram for the interaction of X-ray with the plane of the material, (Bragg's diffraction).

3.5.3 Transmission electron microscopy (TEM)

TEM is a well-known technique to identify the crystallinity and intermolecular arrangements for an ultra-thin sample. The schematic of TEM is shown in figure 3.6. Sharp electron beam is generated by electron gun and further collimated by different magnetic lens. These were accelerated by high potential anode with potential ~100-400 kV. After transmitted through the sample these made to fall on CCD sensor which response to form a very high-resolution image of the sample. The image is detected by the CCD and displayed in real time on computer screen. The electron beam have a fine control from different condenser/objective lens assembly

and get the very fine electron beam which travel through the sample and collect the information about the sample [138]. In general, TEM is working with two imaging mode: (1) Bright-filed image mode (2) Dark-filed image mode. Here we have used most commonly bright-field mode which is commonly used for microstructural analysis while in dark field image mode, direct beam is blocked by the aperture and pass one or more diffracted beam. The lattice planes and interplanar distances can be easily observed with the help of selected area diffraction pattern (SEAD) mode [139]. The wavelength of incident electron beam can easily be controlled by accelerating voltage.

$$\lambda = \frac{h}{p} = \frac{12.25 \times 10^{-10}}{\sqrt{V}} \tag{3.4}$$

Here, we have used TEM, Technai T20 FEI at 200 kV which is equivalent to 2.51 pm wavelength. With such low wavelength, very high-resolution images were obtained.

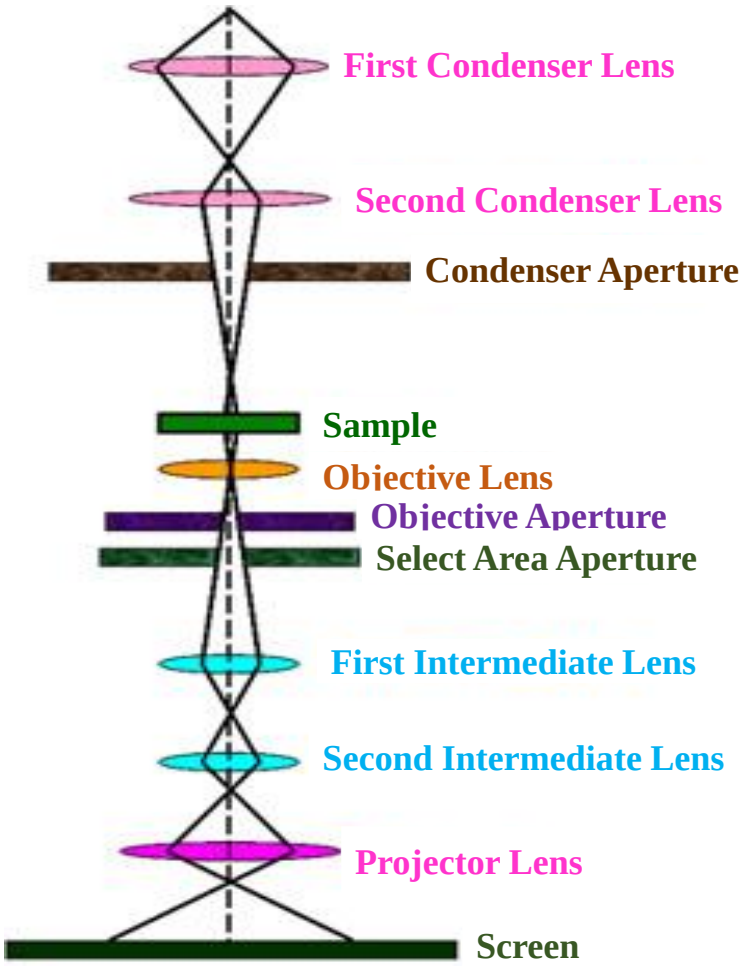

Fig. 3.6 Schematic diagram of the TEM.

3.5.4 UV-visible spectroscopy

When a beam of wavelength ranging from UV to visible falls on the material, then atom or molecules of the material absorbed the energy from incident light and goes

to excited state from ground state. UV-visible spectroscopy is greatly used for quantitative analysis of the materials and using for determine of the band gap of the material. The set up for the UV-vis spectrophotomtere is shown in figure 3.7. The principle of absorption spectroscopy is based on Beer's and Lambert law [140]; it states that fraction of incident radiation absorbed is proportional to the number of absorbing molecules in its path which is described in as follows:

$$A = -log_{10}(\frac{I}{I_o}) = \varepsilon.b.c \tag{3.5}$$

Where, ε = wavelength dependent absorptive coefficient, b = path length, I = intensity of incident light, I_o = intensity of transmitted light and c = concentration. From UV-visible spectroscopy, it is also possible to calculate the band gap using the Tauc's relation:

$$(\alpha h\nu)^{1/n} = A(h\nu - E_g) \tag{3.6}$$

Where E_g is the energy band gap, A is absorption coefficient and $h\nu$ is the energy of incident photon. n = 1/2, 2, 3/2, and 3 corresponding to allowed direct transition, allowed indirect transition, forbidden direct transition, and forbidden indirect transition respectively. Extrapolation of the tangent at the absorbance edge in Tauc's plot gives the value of the band gap of the material.

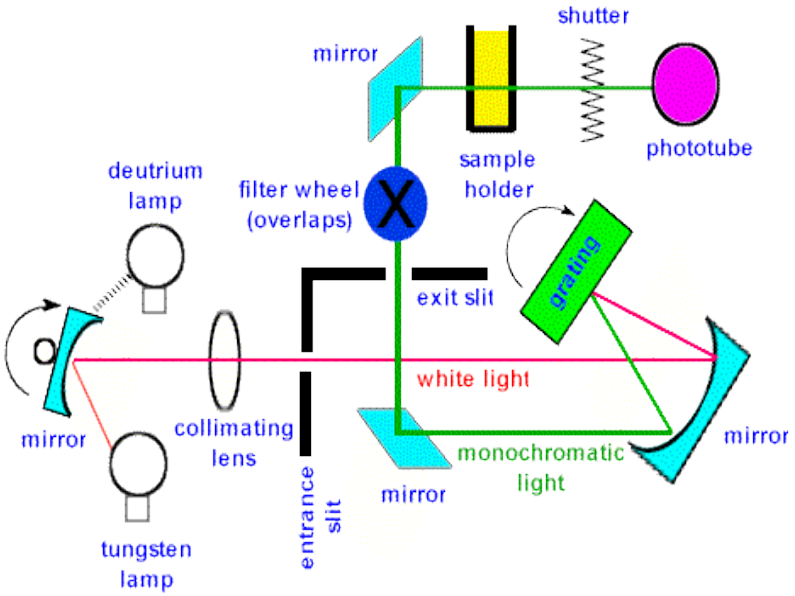

Fig. 3.7 Schematic for the set-up of UV-visible spectrophotometer.

In the present work, the nanoparticles were characterized in absorption mode by Agilent Technologies, Carry 60 UV-vis spectrophotometer.

3.5.5 Fourier transform infra-red spectroscopy (FTIR)

Infrared spectroscopy (IR) is a significant characterization tool to detect the existence of functional groups in a molecule of the specimen [141, 142]. Basically, a source generates light and it is splitted into two parts by beam splitter. One part goes to a reference, and the other one turns to the sample. Sample absorbs a particular wavelength of incident light which is corresponding to desired functional group of sample. A detector collects the passed-out wavelength and compares its energy with the reference (figure 3.8).

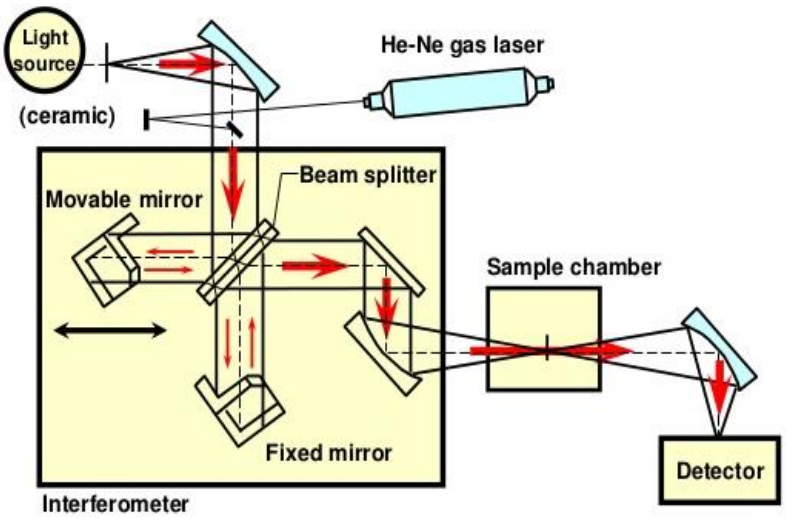

Fig. 3.8 Schematic process for FTIR spectroscopy.

Recorded energy as a function of frequency or wavelength gives information about the presence of functional group in the sample. A typical infrared scan is generated in the mid-infrared (400 to 4000 cm^{-1}) region of the light spectrum. Here, the model of the instrument used for the characterization was Perkin2Elmer. The pellets were prepared using KBr for FTIR measurement.

3.5.6 Raman spectroscopy

Raman spectroscopy is one of spectroscopic technique to observe the different modes of the specimen like vibrational, rotational and other low-frequency modes, based on inelastic scattering of monochromatic light, usually from a laser source with specimen. When the beam incident on the specimen, frequency of the incident photons changes due to inelastic interaction and it may be shifted up and down with the actual incident frequency. This shifting in frequency gives the information about the modes of the samples and this effect is called Raman Effect [143, 144]. This technique is very much useful for most molecular samples like liquids, gels, powders, slurries, some metals and thin films. Usually Raman gives both quantitative and qualitative

result and it is a non-destructive technique [145]. The Raman instrument typically made with four major components (figure 3.9):

1. Excitation laser source
2. light collection optics geometry
3. Filter for select the desired wavelength
4. Detector

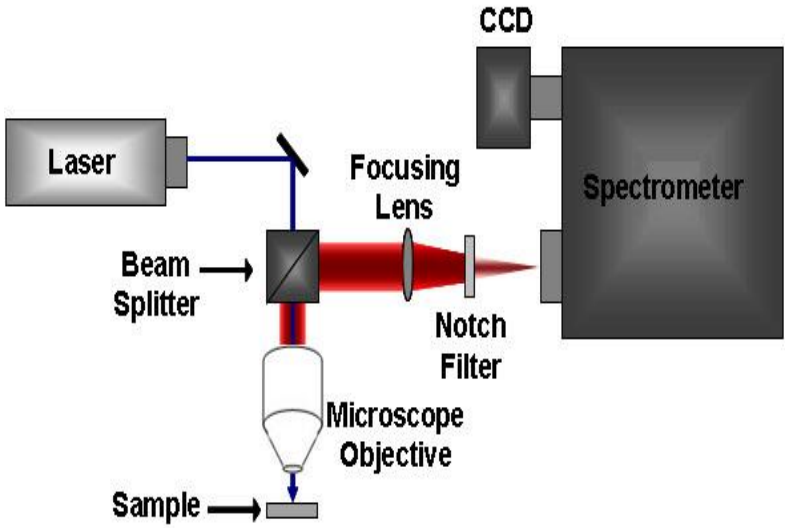

Fig. 3.9 Schematic diagram of Raman spectrophotometer.

The laser line at 532 nm of He-Cd laser was used with an output of 50 mW. The power of the laser at the sample was 5 mW. The Raman spectra were accumulated over 50 sec.

3.5.7 X-ray photoelectron spectroscopy (XPS)

X-ray Photoelectron spectroscopy is surface-sensitive technique to find the elemental composition with chemical and electrical state of the element present in the specimen. XPS spectra are observed by the escaped electrons which are continuously emitted from the sample with different kinetic energy during the X-ray irradiation over the top surface (up to few nanometer) of the sample. So it provides the more reliable information about the electronic structure as well as chemical composition/bonding of the material [146]. The binding energy of the element depends upon work function of the electron. As we move towards the inner shell of the atom, greater the binding energy and lesser the kinetic energy of emitted electron. This binding energy also shift to higher or lower energy when an atom makes bond with other atoms. Shifting depends upon the electron affinity of the sharing atom. The XPS measurements has been taken at ultra-high vacuum. The energy and intensity of electron further

analyzed with the help of the detector and analyze the surface chemistry of the material. The electron binding energy of the each emitted electron is given by fundamental relation [146]

$$E_{binding} = E_{photon} - (E_{KE} - \Phi) \tag{3.7}$$

Where $E_{binding}$ = binding energy of emitted electrons, E_{photon} = energy of X-ray photons, E_{KE} = kinetic energy of the emitted electrons, and Φ is the work function. The basic components of XPS are schematically represented in figure 3.10.

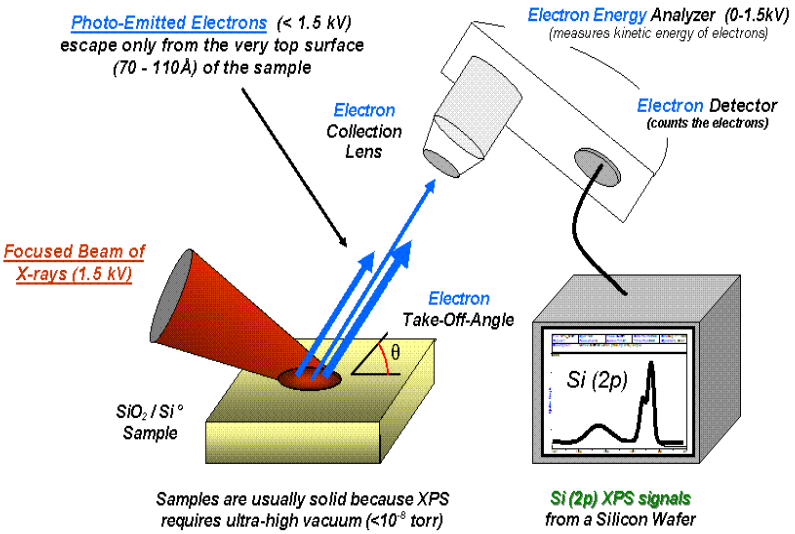

Fig. 3.10 Schematic representation of the XPS with basic components.

Here, XPS (Omnicron nanotechnology) measurements were performed at a pressure of 10^{-10} torr. The general scan and core level spectra of O (1s), S (2p), and Ti (2p) were obtained with monochromatized Al radiation (photon energy 1486.6 eV) with a pass energy of 50 eV for survey and 20 eV for core level spectra. Electron take-off angle was 90°. The background correction in core level spectra were done using the Shirley algorithm. Baseline correction and peak fitting were done using the software CasaXPS. The core level spectra were analysed with respect to the C (1s) binding energy of 284.8 eV.

3.5.8 Scanning electron microscopy (SEM)

Electron microscope are very advantageous microscopy tool due to high magnification and resolving power in comparison of light microscope. The highly energetic focused electron beam interacts with sample surface instead of light to get the image and structural information of the sample. The whole system of the imaging must be vacuum shielded for the prevention of the scattering of the electrons during experiment. The wavelength of the beam can be easily controlled with the operating

voltage which leads to acceleration of the electrons toward the sample. SEM gives following information regarding the specimen. (i) Topography (ii) Morphology (iii) Compositions and (iv) Crystallographic information [142]. The schematic diagram of SEM is shown in figure 3.11. At the top of instrument, there is source of electron beam which produces a very fine scale monochromatic electron beam (diameter $\sim$ 0.01 mm) in the range of 2-40 kV. The first condenser lens is used for controlling the beam. To eliminate the high-angle electrons from the beam, condenser lens works in conjunction with condenser aperture. The second condenser lens utilized to form the very thin, tight and coherent beam and is controlled by the "fine probe current knob". A set of scan coils used for the scan or sweep the electron beam during imaging in a grid fashion.

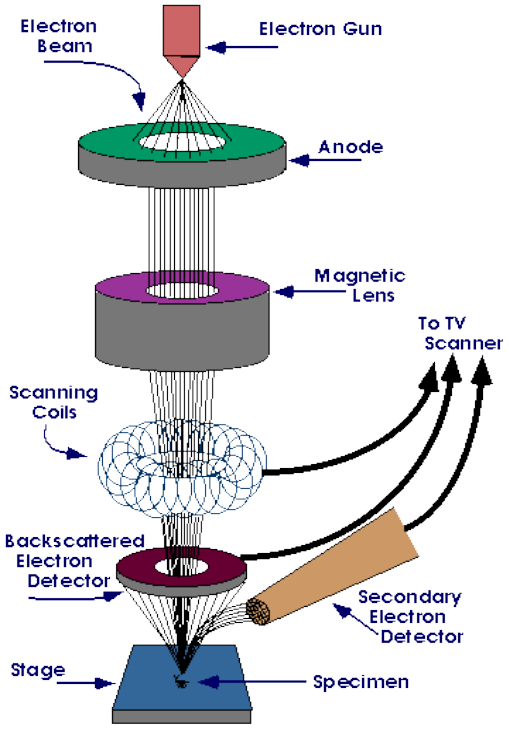

Fig. 3.11 Schematic diagram of SEM.

The various components are placed in the system to observe the interaction of electron beam with specimen and displayed pixel on a CRT monitor. The electron beam interacts with specimen in various ways with the surface of the sample. On the basic of these interactions the mainly two types of the signal are considered for the imaging in SEM and operated in following two modes; (a) Secondary electron mode (b) Backscattered mode. Secondary electron mode is the most common mode for the high-resolution imaging with detailed information about the surface. In this thesis, TiO_2 nanostructures were characterized by SEM (Nova Nano FE-SEM 450 FEI) with an accelerating voltage of 15 kV.

3.6 Conclusions

This chapter summarizes the information about the materials used for the experiments. The details of the methods adopted and the techniques used for the synthesis of the nanotemplates, nanoparticles, and ordered nanostructures have also been discussed. The brief discussion about the working of all the characterization tools have also been introduced.

Chapter 4

Block Copolymer Nanotemplates

4.1 Introduction

Ordered nanotemplates are of notable interest for the fabrication of highly ordered inorganic/organic nanostructures. For the block copolymers with a narrow distribution of molecular weights, different morphologies may be obtained from the phase separation within diblock copolymer thin films. The size and periodicity of blocks are the key parameters for different applications, and can be easily tuned by changing the molecular weight of copolymer [147]. Nanoscale periodicity renders them appealing as patterning materials for various technological applications in energy, membranes, fluidics and information technology [122, 148–150]. The properties and the applications of block copolymers has been discussed in detail in section 1.1 & 2.5. The morphology of the block copolymer thin films (thickness in nanoscale) is mainly directed by two interactions; polymer-substrate and polymer-air interaction. The copolymer which interacts most strongly with the substrate surface prefers to occupy the interface with the substrate surface. For the application of block copolymer as nanotemplates, they must have well-ordered. It provides the highly dense and equally separated domains, with the desired orientation, typically lamellar or cylindrical domains oriented perpendicular to the surface of substrate. However, the perpendicular orientation of domains is in contrary with the tendency to align parallel to the substrate surface because of the preferential interaction of the surface of the substrate with one of the blocks [4, 151]. The desired orientation of microdomains has been achieved by various approaches such as external stimuli, surface modifications and nonequilibrium approaches [147, 152, 153]. Supramolecular assembly has also been used as an efficient approach to obtain well-ordered perpendicular microdomains [48, 57, 154, 155]. Supramolecular assembly is the process in which the small molecules associate with one of the blocks via well-known non-covalent interactions like hydrogen bonding and Vander-Wall interaction. The major role of small molecules in supramolecular assembly is that the relative volume fraction of associated block increased and led to different morphological structures. Additionally,

it is very easy to remove the small molecules without perturbing the morphology of the thin films and create the nanopores/nanochannels lined with a functional group. These obtained nanostructured templates can be used for various applications like solar cells, light-emitting diode (LED), gas sensing, gas separation, field effect transistor (FET), antibacterial activity [156–162]. In present chapter, we have investigated the supramolecular assembly from PS-*b*-P4VP and HABA in 1-4 dioxane with the different molecular weight of PS-*b*-P4VP (M_n =39.9 kg/mol, $M_n = 41$ kg/mol, and $M_n = 205$ kg/mol) and different relative volume fraction of P4VP. Cylindrical (with different size) and lamellar nanodomains oriented perpendicular to the surface have been observed.

4.2 Experimental details

4.2.1 Deposition of thin films of supramolecular assembly

An appropriate amount of block copolymer PS-*b*-P4VP and aditive HABA (P4VP / HABA molar ratio 1:1, 1 wt%) was dissolved separately in the vapours of 1-4 dioxane under sonication. The polymer solution was added dropwise into the HABA solution, and the resultant solution was stirred in a volumetric flask for 3 hours at $75°C$ for homogeneous mixing. Then, obtained solution was allowed to cool and left for overnight to complete the hydrogen bonding between HABA and P4VP. The solution was filtered with 0.2 μm PVDF syringe filter. Separate solutions were prepared for PS-*b*-P4VP of different molecular weight following the same procedure. Thin films of block copolymer were deposited onto the cleaned substrates (Si, ITO coated glass, and ITO coated PET) by dip coating technique. Before deposition of the thin film, the substrates were thoroughly cleaned as described in section 3.3. Substrates were immersed into the filtered PS-*b*-P4VP/HABA solution and withdrawn at a speed of 100 mm/min.

4.2.2 Ordering in thin films and surface reconstruction

Thin films were dried and further annealed in the vapours of 1-4 dioxane in an air sealed glass chamber for 5 days to improve the ordering of nanodomains. Glass chamber was opened and allowed the solvent to evaporate freely. For the fabrication of nanotemplates, the annealed thin films were rinsed with ethanol to extract HABA selectively as ethanol is good solvent for PVP/HABA and poor solvent for PS.

4.3 Results and discussion

In the first step, supramolecular assembled thin films of diblock copolymers were deposited on cleaned Si substrate by dip coating from 1 wt% composite solution

of PS-*b*-P4VP and HABA. HABA molecules are expected to associate with P4VP blocks via hydrogen bond. Chemical structure of PS, P4VP and HABA is shown in figure 4.1. Thin films were annealed in the vapours of 1-4 dioxane for 5 days (slow rate of evaporation of solvent in chamber) in a sealed glass chamber. Surface morphology of thin films was observed by AFM in both the cases, before annealing and after annealing. Schematic for the fabrication of block copolymer nanotemplates is depicted in figure 4.1.

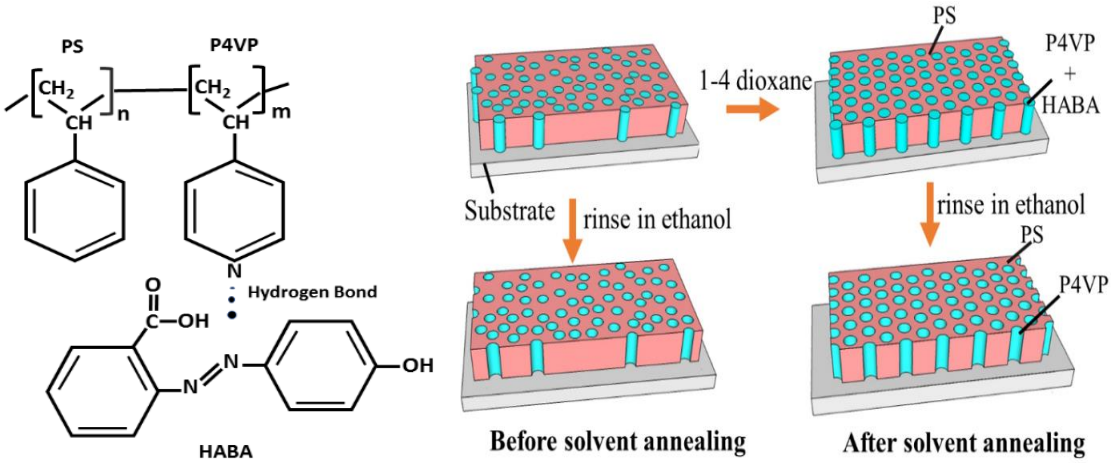

Fig. 4.1 Chemical structure of PS-*b*-P4VP/HABA supramolecular assembly (left) and schematic for the fabrication of nanotemplates (right).

4.3.1 Vertically aligned cylindrical porous templates

Figure 4.2 (a, b) represents the height and phase image of surface morphology of thin films of PS-*b*-P4VP/HABA ($M_n^{PS} = 35.5\ kg/mol$, $M_n^{P4VP} = 4.4\ kg/mol$) before annealing. It can be seen from images that both the phases are separated within nanoscale but the blocks are not well-ordered. It is attributed to the fast evaporation of solvent due to which polymer chains have not sufficient time to rearrange themselves to attain the equilibrium morphology. RMS roughness of the image was found as $\sim$1.2 nm. No sharp reflections have been observed in the fast fourier transform (FFT) of image which indicates that domains are not arranged in a particular order. The ordering of thin films can be improved by thermal annealing and solvent annealing. For supramolecular assembly, solvent annealing has been adopted to avoid the evaporation of small molecules at high temperatures because a little loss of small molecules can greatly affect the structures in thin films [48]. When the deposited thin films were exposed to the vapour of 1-4 dioxane in a glass chamber for annealing and examined by AFM, nanodots like features have been observed (shown in figure 4.2 ((c, d)). These dots like features are corresponding to P4VP/HABA domains dispersed in PS matrix.

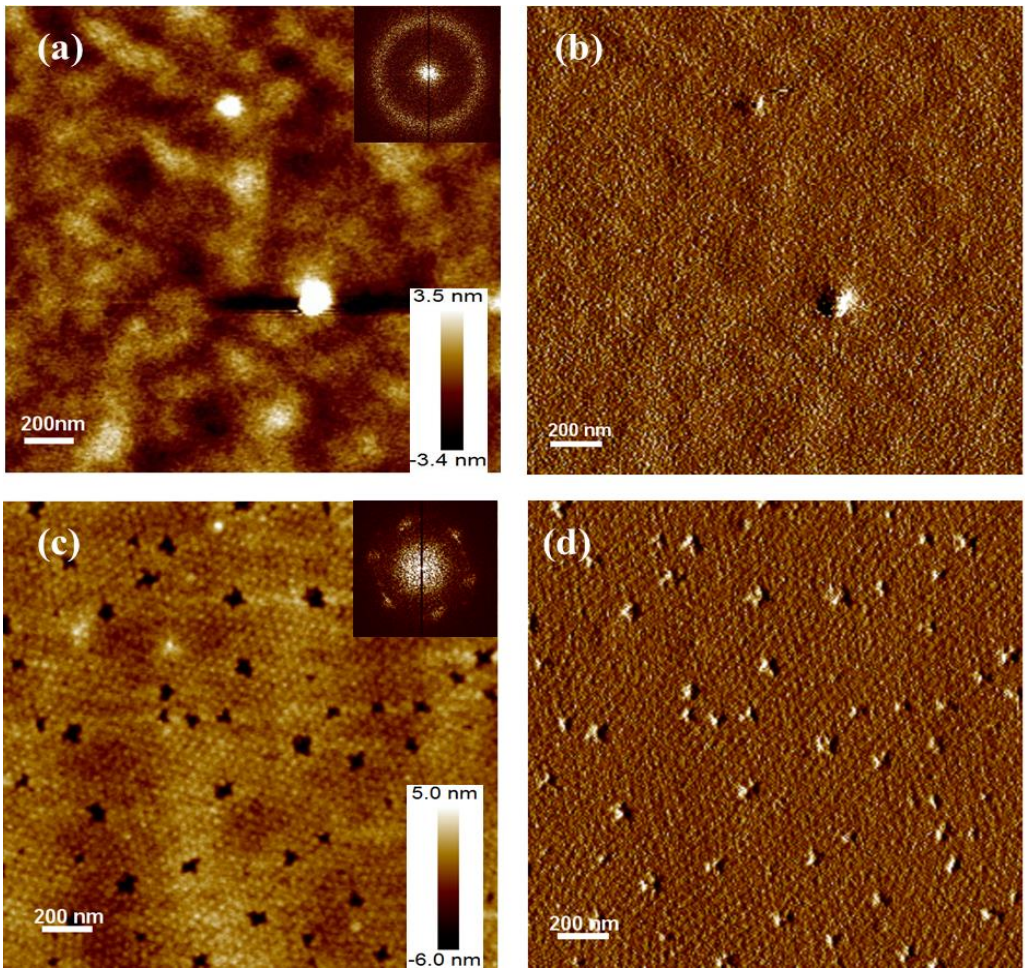

Fig. 4.2 AFM height and phase images of PS-*b*-P4VP/HABA ($M_n^{PS} = 35.5\ kg/mol$, $M_n^{P4VP} = 4.4\ kg/mol$) thin films (a-height, b-phase) without annealing and (c-height, d-phase) annealed in 1-4 dioxane vapours.

It is to be noted here that the relative volume fraction of P4VP/HABA in supramolecular assembly of PS-*b*-P4VP/HABA is approximately 0.3 so it is expectable that P4VP/HABA is arranged into the cylindrical domains (according to the phase diagram demonstrated by Matsen and Bates [6]). It could be hypothesized that these dots like features are the apex of cylindrical domains formed by P4VP/HABA. Tung *et al.* have reported that the orientation of cylindrical domains in supramolecular assembled thin films strongly depends on selectivity of solvents to each block and preferential interaction of the blocks to the surface of substrate [55]. Molecules of solvents used for annealing can provide the mobility to supramolecules leading to rearrangement of supramolecules into more ordered structures after annealing. Albeit the mobility of each phase may be different in different solvent. From figure 4.2, the inferences can be drawn that after solvent annealing, the P4VP/HABA domains are cylindrical, well-ordered, periodic and normal to the surface of substrate. Sharp six reflections in FFT (inset) reveals the hexagonal arrangement of cylindrical

domains. The thin films are very smooth and RMS roughness is found to be reduced on annealing and measured as $\sim$1 nm for an area of 2 $\times$ 2 μm^2 (lateral scale).

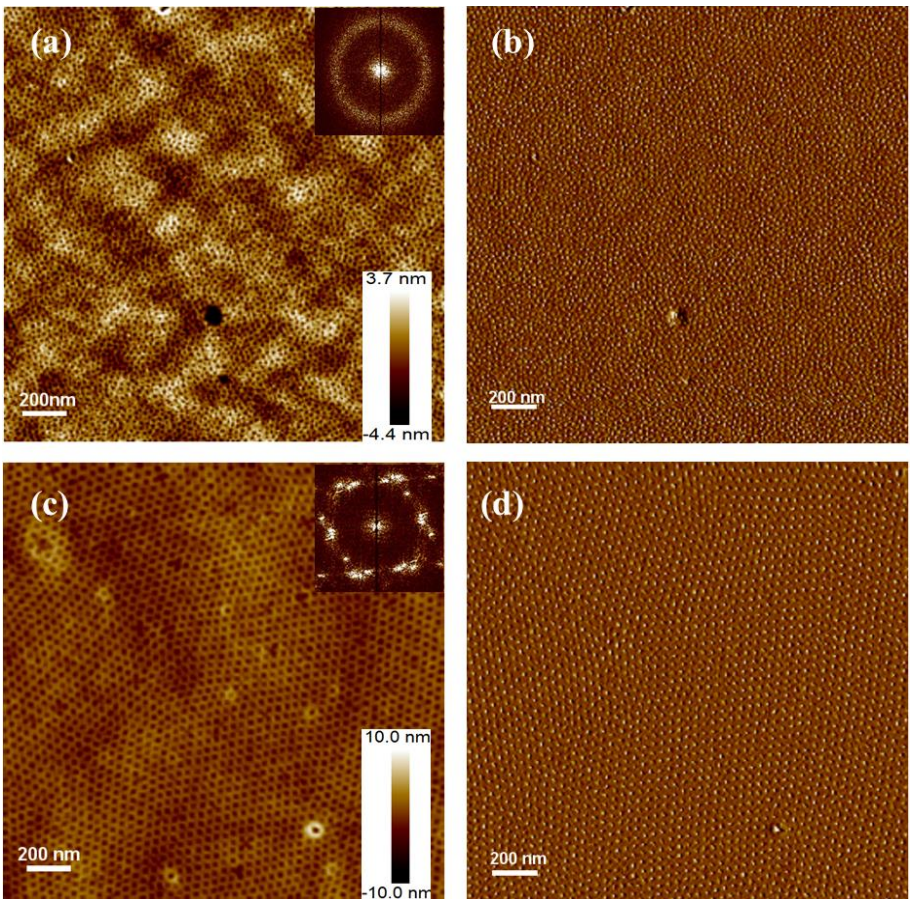

Fig. 4.3 AFM height and phase images of PS-*b*-P4VP/HABA ($M_n^{PS} = 35.5\ kg/mol$, $M_n^{P4VP} = 4.4\ kg/mol$) thin films after immersing in ethanol for 20 minutes (a-height, b-phase) without annealing and (c-height, d-phase) annealed in 1-4 dioxane vapours.

In the second step, the films were removed from the annealing chamber and rinsed in ethanol for 20 minutes for surface reconstruction and selectively extraction of HABA. Ethanol allows the disturbance of hydrogen bonds between HABA and P4VP and removes HABA molecules from the P4VP/HABA domains in thin films. So, additive (HABA) is selectively removed and leaving the nanochannels/nanopores lined with a functional group. However, ethanol imparts the mobility to P4VP/HABA chains but the movement is hindered by frozen PS chains as it is good solvent for P4VP/HABA and bad solvent for PS, thereby, retained the same morphology after dipping into ethanol. AFM images of PS-*b*-P4VP/HABA thin films without annealing, and after washing in ethanol is shown in figure 4.3 (a). It is clearly seen from height and phase images that the additive has been removed and porous structures are easily seen. However, the pores were not exhibiting long range ordering seen by FFT also. On the other hand, solvent annealed thin films showed hexagonally arranged

cylindrical pores normal to the surface of substrate after surface reconstruction as well as removal of HABA by dipping the film into ethanol (figure 4.3 (c, d)). Section

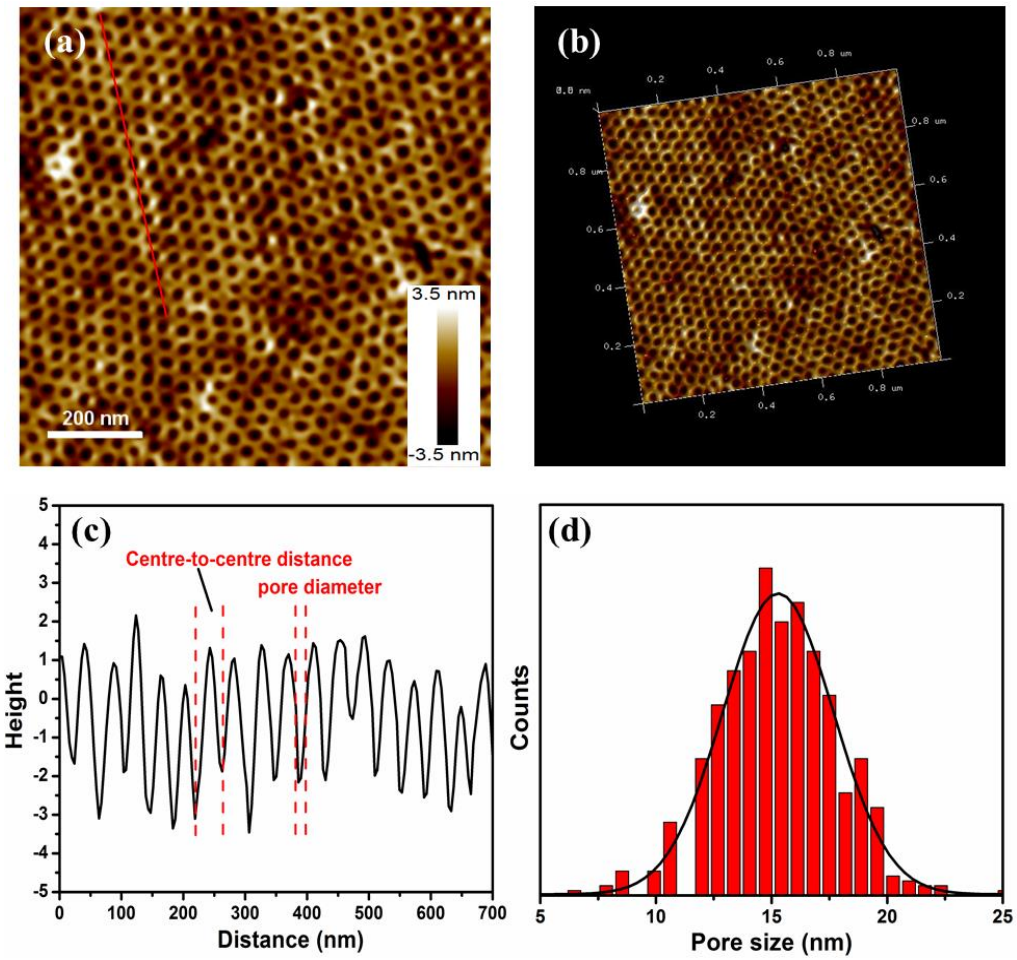

Fig. 4.4 (a, c) Section analysis of cylindrical pores in PS-*b*-P4VP/HABA ($M_n^{PS} = 35.5$ kg/mol, $M_n^{P4VP} = 4.4 kg/mol$) thin films annealed in 1-4 dioxane and immersing in ethanol for 20 minutes (b) 3-D view of nanotemplates and (d) pore size distribution.

analysis for the few pores is shown in figure 4.4 (a, c). Pore diameter and centre to centre distance was measured by Nanoscope Analysis over an image of $2\times$ 2 μm^2 lateral scale. Distribution of pore diameter is represented in figure 4.4 (d) and an average pore diameter of 15 ± 1 nm has been observed. Centre to centre distance was measured as 35 ± 2 nm.

For the applicability of the templates in various fields of research, the templates are to be prepared on various substrates. ITO coated glass substrates are commonly used for optoelectronic applications because of their good conductivity and transparency in visible region. It is evident from figure 4.5 that the morphology, size and the porosity of templates remains the same as on Si substrates while the deposition and annealing parameters kept same.

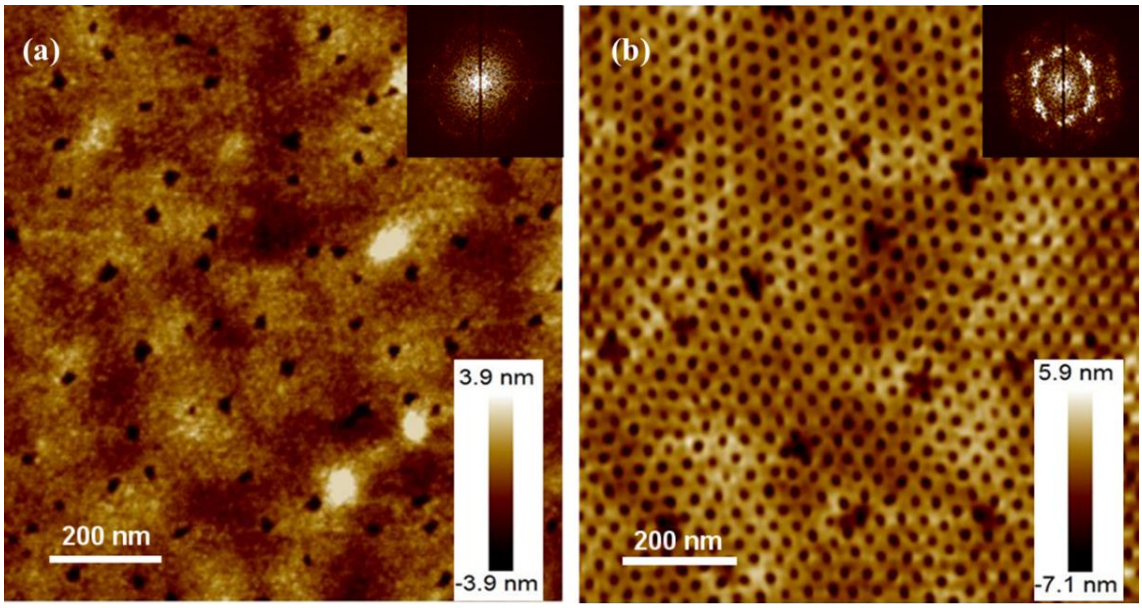

Fig. 4.5 AFM height images of PS-*b*-P4VP/HABA ($M_n^{PS} = 35.5\ kg/mol$, $M_n^{P4VP} = 4.4\ kg/mol$) thin films on ITO coated glass substrates and annealed in 1-4 dioxane vapours, (a) before and (b) after immersing in ethanol.

Nowadays, flexible devices have received immense interest due to their portability. ITO coated PET (polyethylene terephthalate) provide the flexibility in addition to conductivity and transparency. Thin films of block copolymer were deposited on ITO coated PET and annealed by following the same procedure and keeping the parameters same. Figure 4.6 revealed that the templates have pores of almost the same size though the image is not showing the perfect ordering of the pores. It may be affected due the flexibility of the substrate. However, it can be optimized and ordering can also be achieved. On the basis of above results it can be concluded that these nanotemplates are versatile and applicable to different applications.

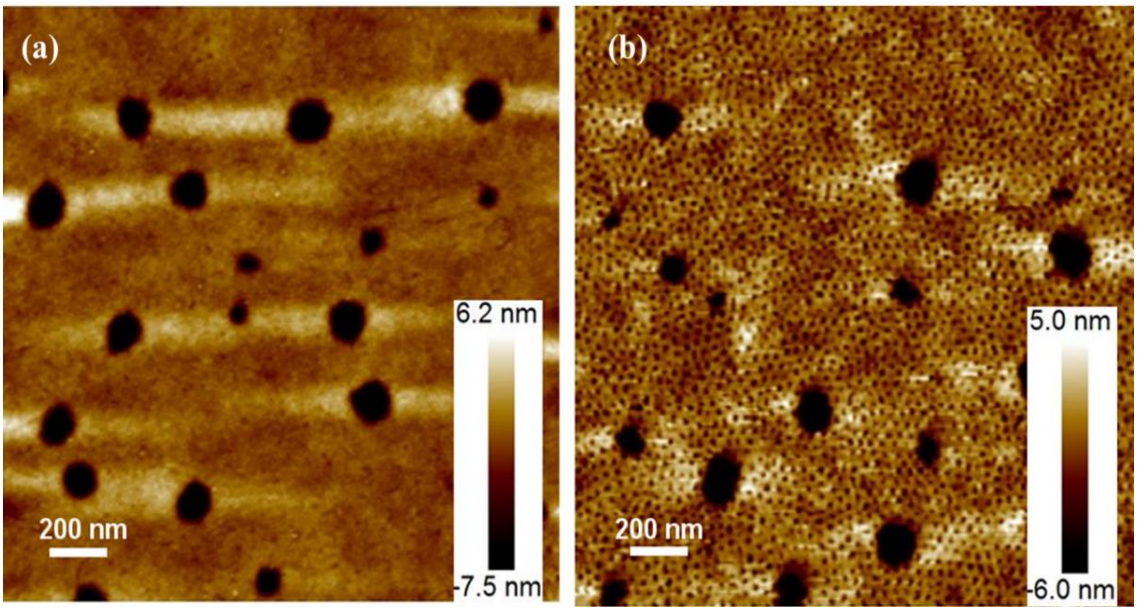

Fig. 4.6 AFM height images of PS-*b*-P4VP/HABA ($M_n^{PS} = 35.5\ kg/mol$, $M_n^{P4VP} = 4.4\ kg/mol$) thin films on ITO coated PET substrates annealed in 1-4 dioxane vapours, (a) before and (b) after immersing in ethanol.

As stated by the self-consistent field theory, the morphological parameters depend on the molecular weight, Flory Huggins interaction χ, volume fraction and the degree of polymerization [3]. Figure 4.7 shows the morphology of the supramolecular assembled thin films of PS-*b*-P4VP with the high molecular weight of polymer $M_n^{PS} = 130\ kg/mol$, $M_n^{P4VP} = 75\ kg/mol$, relative volume fraction of P4VP is also much higher. Before adding the additive, P4VP has a weight fraction of ~ 0.36 and it increases to ~ 0.65 after selective addition of HABA in equimolar ratio which is near the boundary of lamellar/cylindrical in bulk. Parameters for deposition and annealing of film kept same as for the lower molecular weight ($M_n^{PS} = 35.5\ kg/mol$, $M_n^{P4VP} = 4.4\ kg/mol$). P4VP/HABA dots in PS matrix are observed in figure 4.7. After selective binding of HABA with P4VP, P4VP-HABA constitutes the majority phase. Despite the P4VP-HABA constituting a majority phase, still P4VP-HABA core surrounded with PS corona was observed. This is referred as "inverted phase" which depends mainly on the nature of solvent or the interaction between solvent and each block and the concentration of solution. If the solvent possesses a preferential affinity to the minority block then swollen rate will be more than that of majority block and effectively it becomes the majority block. In our case 1-4 dioxane has a greater affinity towards PS rather than P4VP. However, other factors may also play a part like rate of evaporation of solvent and interfacial interactions during the deposition [163, 164]. Rinsing in ethanol results the nanoporous film and the size of the porous structure is estimated as 49 *nm*. Similar results for high molecular weight have also been obtained by Laforgue *et al.* using DHN as an additive [58].

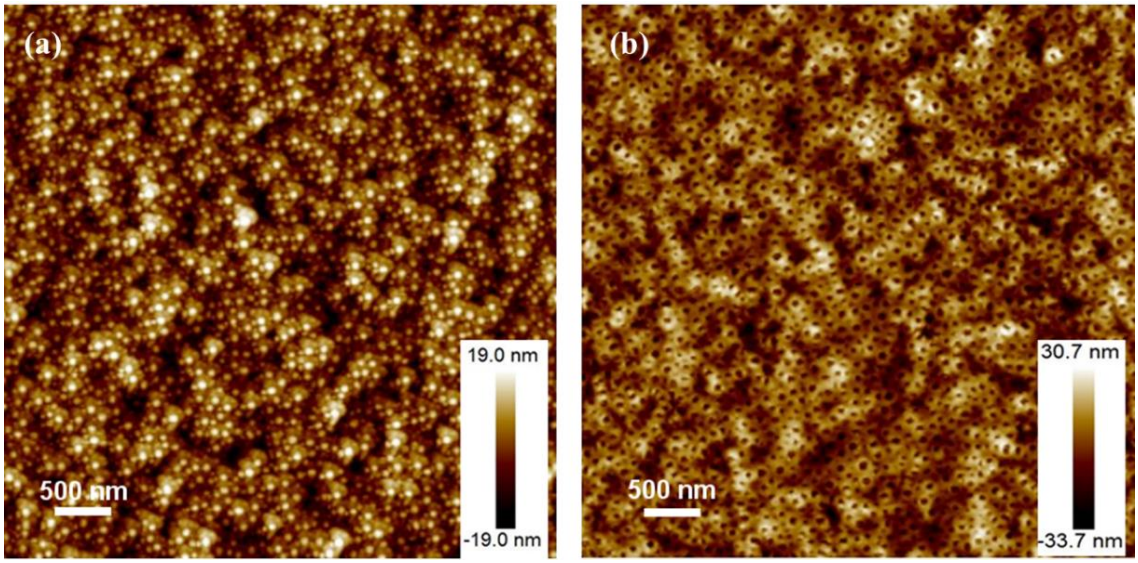

Fig. 4.7 AFM height images of PS-*b*-P4VP/HABA ($M_n^{PS} = 130\ kg/mol$, $M_n^{P4VP} = 75\ kg/mol$) thin films on Si, (a) annealed in 1-4 dioxane and (b) after immersing in ethanol

4.3.2 Vertically aligned lamellar templates

Different morphological behaviour other than cylindrical nanodomains has been observed in the thin films of supramolecular assembly when the different molecular weight or the relative fraction of copolymers have used ($M_n^{PS} = 33\ kg/mol$, $M_n^{P4VP} = 8\ kg/mol$). On addition of HABA with a molar ratio (P4VP: HABA) of 1:1 relative fraction of P4VP/HABA HABA in supramolecular assembly of PS-*b*-P4VP/HABA is approximately 0.5 which is corresponding to lamellar microdomains. Before annealing, thin films of supramolecular assembly are not showing any characteristic features due to fast evaporation of solvent and the expected morphology is far from equilibrium (figure 4.8(a, b)), similar to case of lower relative fraction of P4VP/HABA (figure 4.2 (a, b)). On further annealing in the vapours of 1-4 dioxane, structural reorganization takes place and leads to lamellar structures oriented perpendicular to surface of substrate (figure 4.8 (c, d)) due to the mobility imparted to the copolymer molecules. Measured value of roughness of the thin films was significantly reduced on annealing from 3.9 *nm* - 0.5 *nm*. Above study reveals that by varying the molecular weight or relative volume fraction with suitable solvent annealing in 1-4 dioxane, nanodomains can be reorganized from cylinders to lamella.

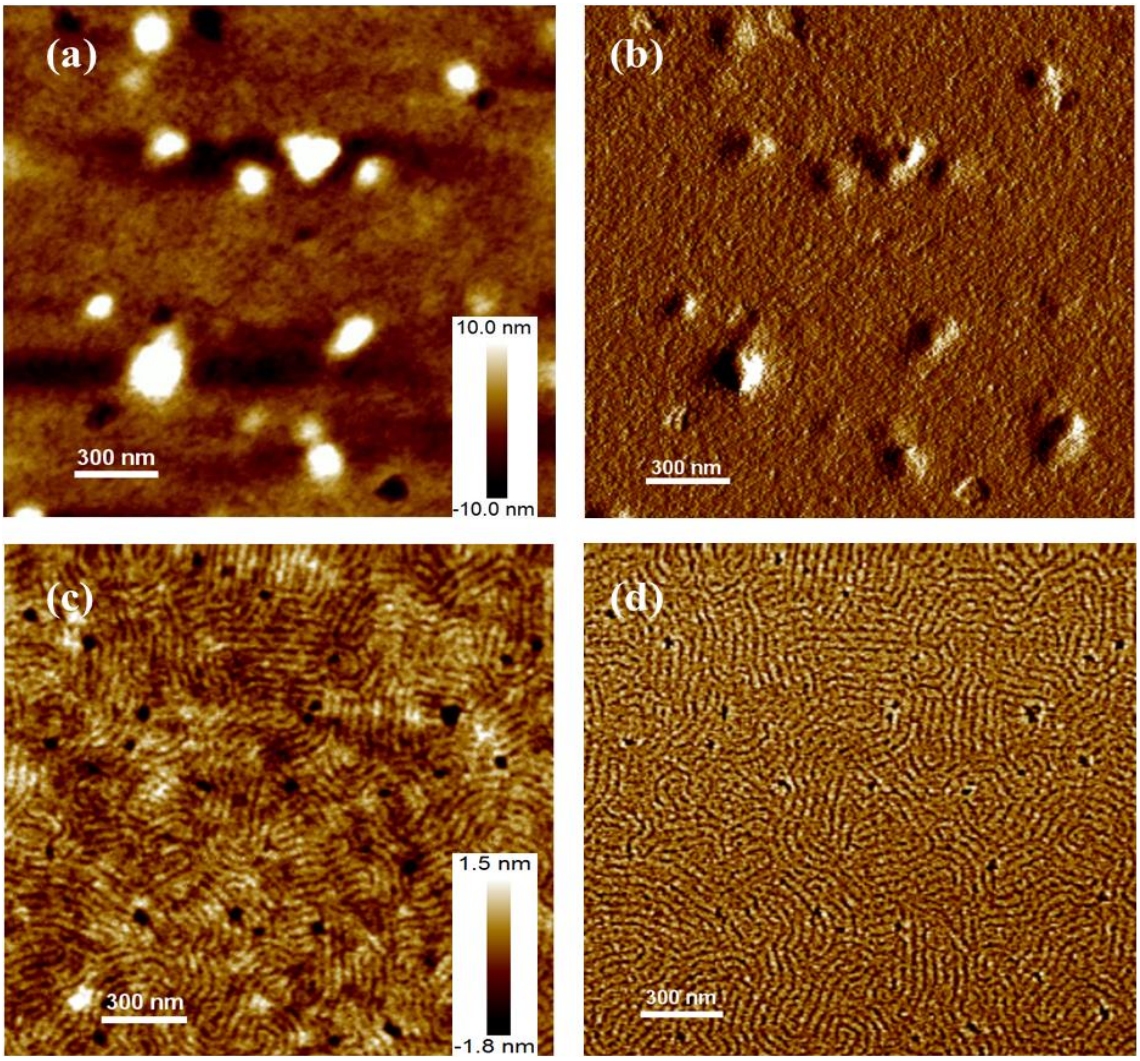

Fig. 4.8 AFM height and phase images of PS-*b*-P4VP/HABA ($M_n^{PS} = 33\ kg/mol$, $M_n^{P4VP} = 8\ kg/mol$) thin films (a, b) without annealing and (c, d) annealed in the vapours of 1-4 dioxane.

Selective extraction of HABA from the annealed thin films of PS-*b*-P4VP/HABA by dipping in ethanol left the films with periodically arranged channels perpendicular to surface of substrate (figure 4.9). Figure 4.9 (a) and (b) are taken at different magnification for the clear view of lamellar channels created in the film. The width and periodicity of the lamellar channels was measured as $\sim 14 \pm 2\ nm$ and $\sim 31 \pm 2\ nm$ respectively. Section analysis over a few porous lamellas is also shown in the figure 4.9 (c) for the estimation about the periodicity of lamellar domains and it is approximately 31 nm.

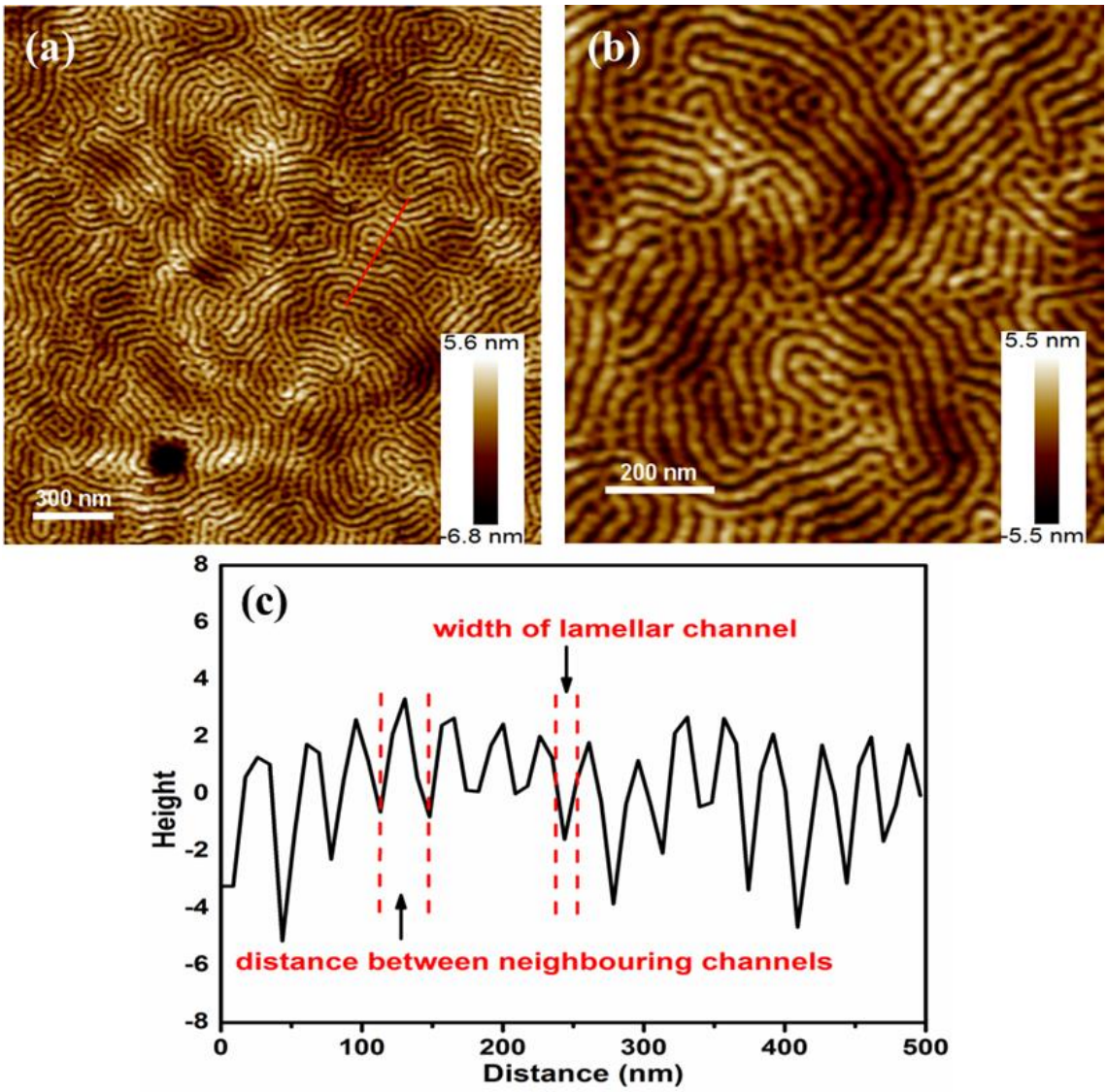

Fig. 4.9 (a, b) AFM images of PS-*b*-P4VP/HABA ($M_n^{PS} = 33\ kg/mol$, $M_n^{P4VP} = 8\ kg/mol$) thin films annealed in 1-4 dioxane and after immersing in ethanol (c) Section profile along the line shown in (a).

4.4 Conclusions

In this chapter, variation in morphological parameters with molecular weight and the relative volume fraction have been discussed. In summary, it could be concluded that the supramolecular assembly is an efficient approach for the preparation of highly dense and ordered nanotemplates. In the as-deposited thin films of PS-*b*-P4VP/HABA, the microdomains are not self-arranged in an ordered fashion due to the fast evaporation of solvent. Lateral ordering was then improved by the solvent annealing in 1-4 dioxane. The molecules of the annealing solvent impart the mobility to the copolymer molecules and leads to the rearrangement of the molecules to the equilibrium. Selectivity of the solvent offers the different affinity towards the each

copolymer and resulted in the perpendicular orientation of the domains. Minority block (P4VP/HABA) forms cylinders surround by majority block (PS). On surface reconstruction, nanotemplates with hexagonally arranged cylindrical pores (pore diameter 15 ± 1 nm, centre to centre distance 35 ± 2 nm) were obtained. Increasing the molecular weight of the copolymers and keeping the relative volume fraction almost same, the average size of the porous structure increased to 49 ± 3 nm. By changing the molecular weight of the copolymer as well as relative volume fraction of each phase, lamellae microdomains with a periodicity of 31 ± 2 nm have been obtained. The vertical orientation of nanodomains (cylindrical and lamellar) can be easily obtained without applying any external force.

Chapter 5

Synthesis and Characterizations of TiO_2 Nanoparticles

5.1 Introduction

TiO_2 nanoparticles constitute a very important class of material that has been widely studied and applied in photocatalysis [165], catalysis [166], photovoltaic cells [167], gas sensors [168], pigments or coatings [169], self-cleaning surfaces [170] and water purification [171] etc. TiO_2 has three polymorphs i.e. anatase (tetragonal I4/amd), rutile (tetragonal $P42/mnm$), brookite (orthorhombic Pcab) [172]. Among all three phases, rutile is most thermodynamically stable and rest of two are metastable. Anatase phase shows better photocatalytic activity than rutile while rutile is largely employed for pigments due to its effective light scattering [173]. Furthermore, mixed phase of anatase and rutile is known to possess enhanced photocatalytic activity which depends on electron-hole recombination rate, crystallinity, adsorptive affinity and particle interconnection [174–176]. TiO_2 has a band gap of 3.0 eV for rutile, 3.2 eV for anatase and 2.96 eV for brookite phase. All the polymorphs absorb in the UV region of electromagnetic spectrum. The phase transform from one phase to another in all TiO_2 polymorph can be in different ways; anatase to rutile, anatase to brookite and then brookite to rutile, brookite to anatase and then anatase to rutile. This phase transformation depends on various parameters; initial particle size, phase, and crystallinity, content of impurity, reaction temperature and pressure etc. [177]. Physiochemical properties of TiO_2 nanoparticles greatly influenced by size distribution, morphology, crystalline phase and the final state present at the surface of the materials [176, 178]. Various methods have been adopted for the synthesis of TiO_2 nanomaterials i.e. hydrothermal, solvothermal, and sol-gel method etc [179–181]. Among all these techniques sol-gel method has many advantages: simple, cheap technological equipment, stoichiometry control, cost effective, room temperature synthesis and a wide possibility to vary the properties by changing the composition

of the solution. For the effective use of TiO_2 in photochemical procedures, less rate of electron-hole recombination at the surface of TiO_2 is beneficial. Surface of the nanoparticles can easily be modified in sol-gel method using suitable capping agents. 1-thioglycerol act as a capping agent and prevents the nanoparticles agglomeration [182]. Growth of nanoparticles and surface medication results the change in structural and optical properties of nanoparticles. Here, we report the synthesis of TiO_2 nanoparticles by sol-gel method using 1-thioglycerol as a capping agent and its effect on size and the band gap of TiO_2 nanoparticles. Chemical bonding between the capping agent and nanoparticles were characterized by FTIR and XPS. For structural and optical properties, the nanoparticles were characterized by XRD, TEM and UV-visible spectroscopy.

5.2 Experimental details

5.2.1 Sol-gel method

TiO_2 nanoparticles were synthesized by sol-gel method [183]. Titanium (IV) isopropoxide (5 ml) was dissolved in ethanol (10 ml) and followed by stirring for 10 minutes. After that distilled water (50 ml) was added to the above solution under stirring and continued the stirring for 20 minutes. The white precipitate was formed and separated by centrifugation. The obtained precipitate was washed 5 times with distilled water to eradicate the alcohol. Decanted precipitate was dissolved completely in hydrogen peroxide (10 ml), an orange colored transparent sol was formed which transformed into a gel within few minutes at room temperature. Obtained gel was placed in an oven at 70°C until get dry. Yellowish amorphous TiO_2 powder was obtained by grinding the dried gel. The powder was post-annealed at 350°C for the transformation from amorphous to crystalline TiO_2 nanoparticles.

5.2.2 Modified sol-gel method

A slight modification was done in the above-mentioned sol-gel method; synthesis of nanoparticles was assisted by capping agent (1-thioglycerol). 0.25 ml of 1-thioglycerol was added after the addition of water and keeping the rest of the procedures and annealing temperature same. Samples with and without 1-thiogylecrol were designated as C-TiO_2 and TiO_2 respectively.

5.3 Results and discussion

5.3.1 TiO_2 nanoparticles by sol-gel method

X-ray diffraction patterns were recorded to analyse the structure and crystallite size of TiO_2 nanoparticles. Figure 5.1 shows the XRD pattern for TiO_2 nanoparticles without annealing and annealed at $350°C$. The broad peak at 25.3° observed in XRD pattern of nanoparticles without annealing indicates the amorphous behaviour of synthesized powder. After annealing, amorphous powder transforms into the crystalline TiO_2 with the crystallite size of the order of nanometer, estimated from the broadening of peaks. For TiO_2 nanoparticles, peaks at 25.39°, 37.99°, 48.11°, 54.04°, 55.13° and 62.73° are corresponding to the reflections from (101), (004),(220),(105), (211) and (204) planes respectively. These reflections confirm the anatase phase formation of TiO_2 nanoparticles (JCPDS No. 01-084-1285). There is no evidence for the rutile and brookite phase in XRD pattern. The average crystallite size was calculated using Debye-Scherrer formula [184].

$$\tau = \frac{0.9\lambda}{\beta cos\theta} \tag{5.1}$$

Where τ is particle size, λ is the wavelength of incident X-rays, β is full width at half maximum (FWHM) and θ is angle of diffraction. The average crystallite size was calculated as $\sim 13\ nm$. Further the size, shape, phase and crystallinity of the nanoparticles were investigated using TEM. Figure 5.2 represents the TEM image of TiO_2 nanoparticles annealed at $350°C$.

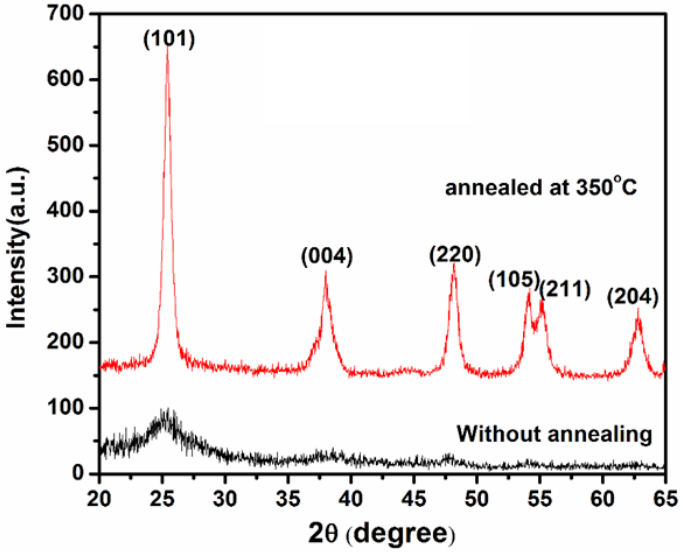

Fig. 5.1 XRD pattern of TiO_2 nanoparticles without annealing and annealed at 350°C

It seems that the shape of the nanoparticles is nearly spherical, however the particles are agglomerated. Average particle size estimated from TEM was around 14 nm

and it is in good agreement with the XRD results. HRTEM images show the lattice planes corresponding to (101) plane of anatase phase and *d*-spacing was found to be 3.52 Å. The observed rings in SAED pattern of TiO_2 nanoparticles clearly indicate the polycrystalline nature of nanoparticles and all the rings are corresponding to the planes of anatase TiO_2. Raman spectra also confirm the anatase phase of synthesized nanoparticles (figure 5.3).

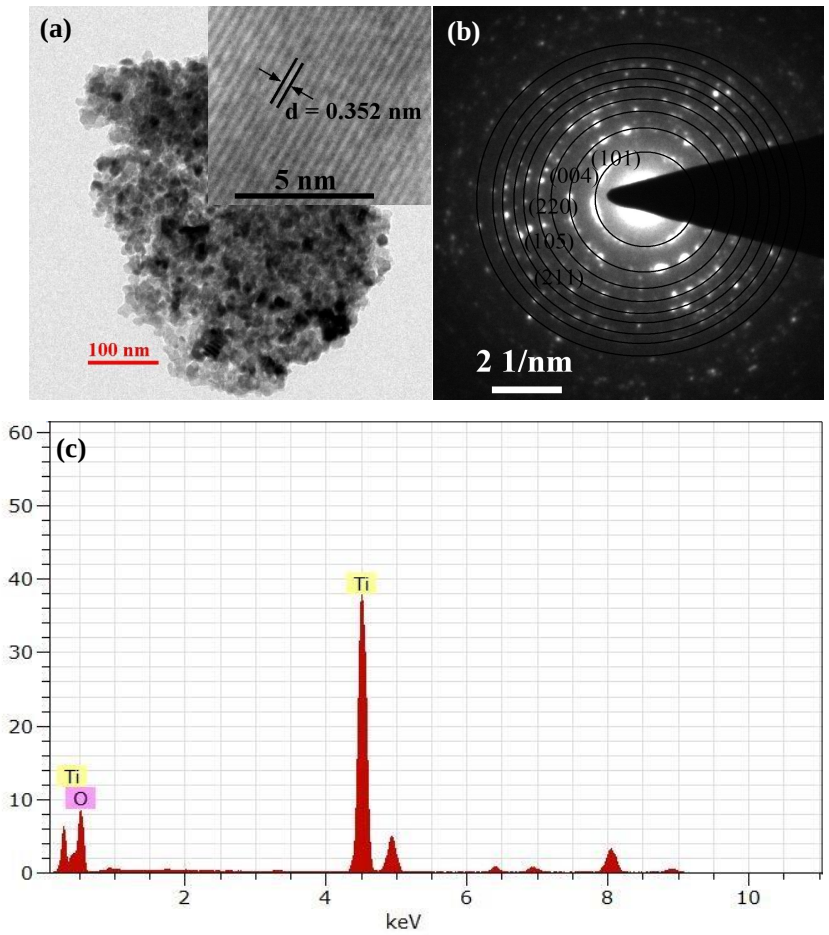

Fig. 5.2 (a) TEM image of TiO_2 nanoparticles, inset shows HRTEM image of lattice planes. (b) SAED pattern, and (c) EDX pattern of TiO_2 nanoparticles.

Ohsaka reported the Raman spectrum of anatase single crystal with six allowed mode at 144 cm^{-1} (E_g), 197 cm^{-1} (Eg), 399 cm^{-1} (B1g), 513 cm^{-1} (A1g), 519 cm^{-1} (B1g), and 639 cm^{-1} (Eg) [185]. Here, the five bands at 145 cm^{-1}(most intense), 197 cm^{-1}(a small peak), 398 cm^{-1}, 517 cm^{-1}, and 639 cm^{-1} are obtained. All these Raman active modes are corresponding to anatase phase of TiO_2. The existence of rutile [186] and brookite phase [187] is not evidenced from Raman spectra.

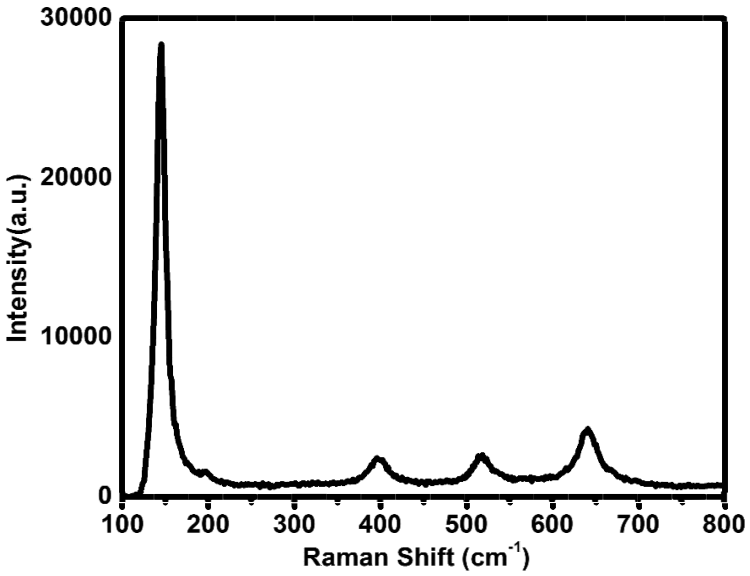

Fig. 5.3 Raman spectra of TiO_2 nanoparticles annealed at $350°C$.

5.3.2 TiO_2 nanoparticles by modified sol-gel method

In the previous section, the synthesis of TiO_2 nanoparticles and their characterizations for particle size and phase formation have been discussed and results show the anatase phase formation of nanoparticles with an average size of $\sim 13\ nm$. The formation of block copolymer nanotemplates have been discussed in chapter 4 and it was concluded that the average pore size of the nanotemplates prepared were $\sim 15\ nm$. So, the nanoparticles discussed in section 5.3.1 are not suitable for the successful deposition into templates. The particle size of nanoparticles has to be reduced, for that a slight modification has been done in the synthesis process. The capping agents are well known to control the growth and shape of the nanoparticles. Here, 1-thioglycerol was used as a capping agent. The process for the synthesis is given in section 5.2.
For the particle size analysis and the phase formation of TiO_2 nanoparticles synthesized by modified method (using capping agent), nanoparticles were characterized by XRD, TEM and RAMAN spectroscopy. For comparison, figure 5.4 (a) shows the XRD pattern of both TiO_2 and C-TiO_2 nanoparticles. It is clear from figure that the phase remains the same. As-synthesized nanoparticles are amorphous in nature and at annealing temperature 350°C anatase phase is obtained with the same lattice planes with decreased intensity. The decrement in the intensity of peaks shows the less crystallinity of nanoparticles synthesized with modified method.

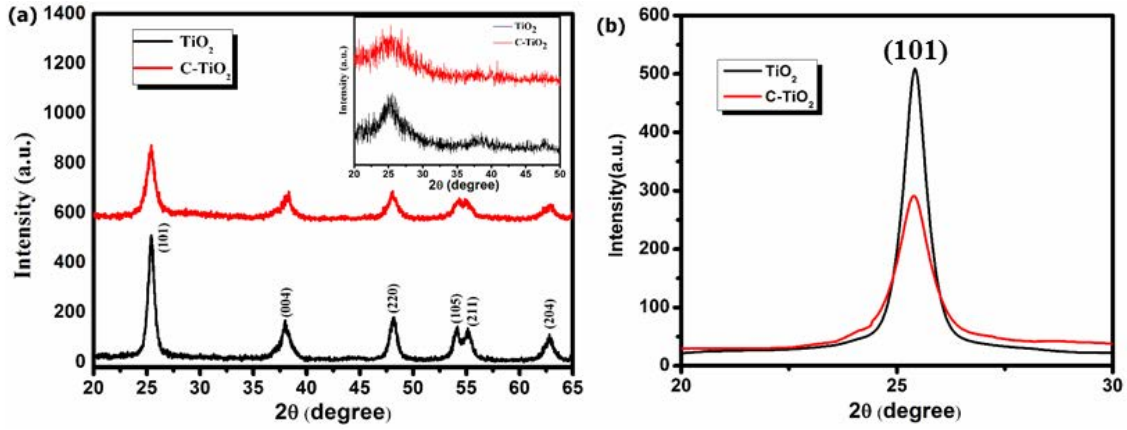

Fig. 5.4 (a) XRD pattern of TiO_2 and C-TiO_2 without annealing (inset) and annealed at 350°C (b) peak for (101) plane for TiO_2 and C-TiO_2.

An increase in the FWHM of the peaks clearly indicates the lower crystallite size and it was calculated as $\sim 9\ nm$. So, the capping agent affects the crystalline behaviour of nanoparticles and also reduces the particle size. Smaller the particle size, larger the surface area, which points towards more applicability of TiO_2 nanoparticles synthesized with capping agent. Recently, G. Xiang *et al.* illustrated the size dependent surface activity of titania and demonstrated that when size of the nanocrystals was small enough, their surface activity could be significantly enhanced [176]. Moreover, particle size growth rate and phase transformation depend on various parameters as initial particle size, starting phase, reaction temperature, pressure, impurity content etc. [188]. There is no spurious peak observed in the samples which indicates the crystallographic purity. The functional group of capping agents attach with the Ti or O of the nanoparticles and reduces the agglomeration or in other way it inhibits the growth of nanoparticles. The binding of the capping agent with nanoparticles was further examined by FTIR spectroscopy. No discernible shifting in the position of the most intense peak (101) of XRD pattern was observed (figure 5.4 (b)), only FWHM was found to be increased.

Raman spectra of TiO_2 and C-TiO_2 nanoparticles were measured to obtain more information about the structural behavior of nanoparticles and shown in figure 5.5. Both the spectra were recorded at room temperature. On comparing the Raman spectra of TiO_2 and C-TiO_2 nanoparticles, it was observed that no additional band occurred on using the capping agent which suggest the same structure of nanoparticles. Inset shows the enlarged view of principal Raman band of anatase TiO_2 and C-TiO_2 at 144 cm^{-1}. It is found that the position of peak shifts to higher wavenumber (from 145 cm^{-1} to 146.3 cm^{-1}) but it may be considered within the instrumental error also, though few literature suggested a decrease in the particle size on shifting the position of peak towards higher number [189, 190].

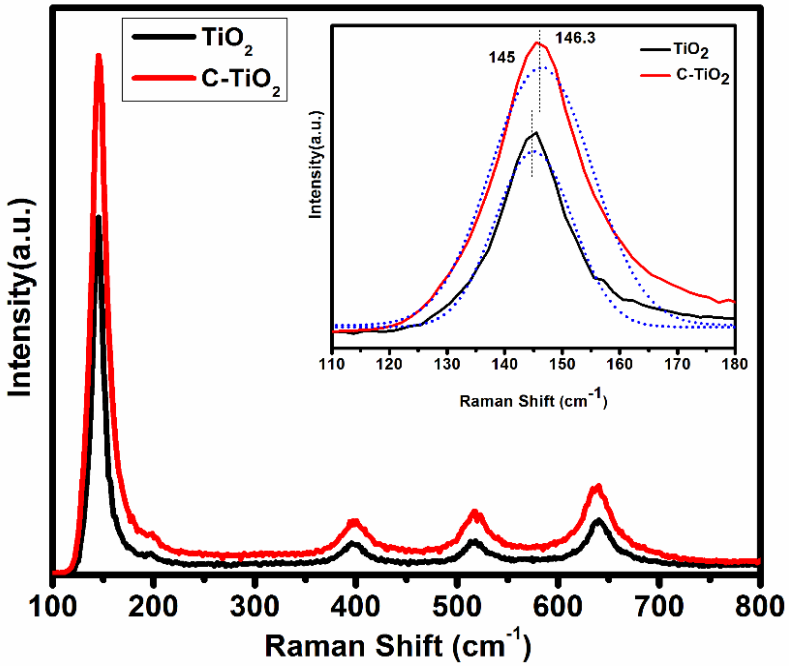

Fig. 5.5 Raman spectra of both TiO_2 and C-TiO_2 nanoparticles annealed at 350°C. Inset represents the principal Raman band of TiO_2 and C-TiO_2 nanoparticles.

No discernible signals corresponding to sulfur containing species was detected, which demonstrates that C-TiO_2 nanoparticles retain the same structure as the TiO_2 (anatase). These results are supported by XRD also. FWHM of the peak found to be increased and supports the decrement in the size.

Size and the shape of C-TiO_2 nanoparticles were further investigated by TEM. It can be seen from figure 5.6(a) that the shape of the nanoparticles remains unaffected, however the nanoparticles are less agglomerated as compared to the without capping agent and the particles size calculated from the TEM images $\sim 10\ nm$ was in good agreement with XRD results. HRTEM images show the lattice planes corresponding to (101) plane and d-spacing was found to be 3.57 Å which is almost same as for TiO_2 (3.52 Å). Since no significant change in d spacing is observed so shifting in the peak position of (101) in XRD cannot be expected. SAED pattern of represents all the rings corresponding to the planes observed in XRD patterns. EDX pattern shows the elements presents in the product. Here, Ti and O are the main element of TiO_2, S is present due the 1-thioglycerol used as a capping agent, C and Cu are from the TEM grid used for the sample preparation. No other element is present which indicates the absence of impurity in the nanoparticles.

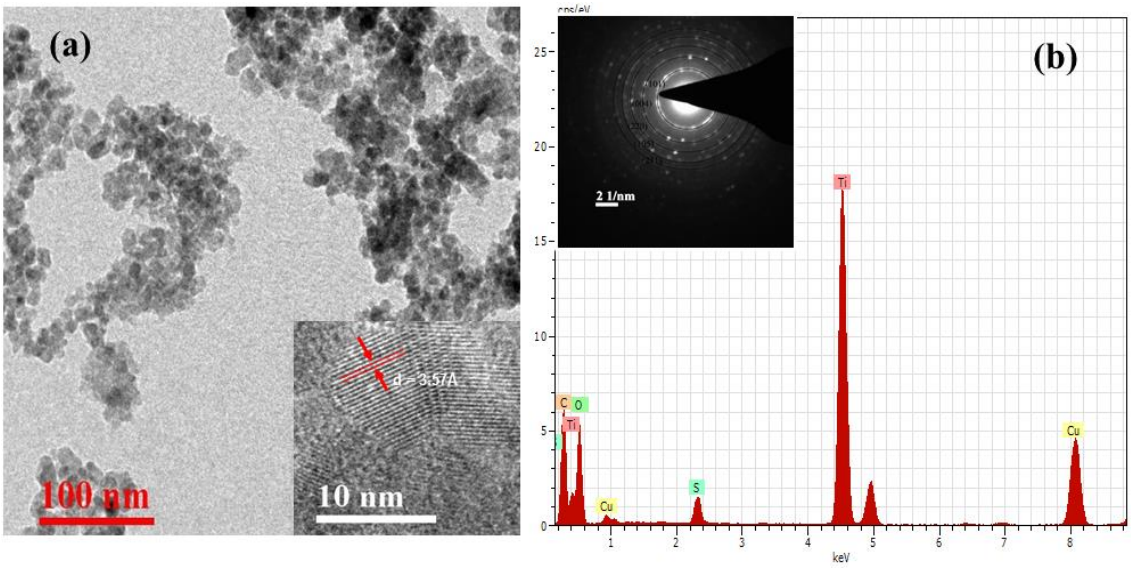

Fig. 5.6 (a) TEM image of C-TiO_2 nanoparticles, inset shows HRTEM image of lattice planes. (b) EDX pattern and SAED pattern (inset) of C-TiO_2 nanoparticles.

FTIR spectroscopy is a promising technique to gather the information about all the fundamental bands or the bonding characteristics of TiO_2. Figure 5.7 shows the FTIR spectra of TiO_2 and C-TiO_2 nanoparticles. Bands from 400 cm^{-1} to 800 cm^{-1} are corresponding to lattice vibrations of TiO_2 structure (Ti-O, Ti-O-Ti) [191]. Two additional peaks at 1049 cm^{-1} and 1126 cm^{-1} are observed in spectra of C-TiO_2 nanoparticles, which is an indicative of a new interaction. These bands arise from symmetric and asymmetric stretching vibration of S-O bonds on TiO_2 surface [192, 193]. The peak at 1636 cm^{-1} is attributed to bending vibrations of adsorbed water molecules [194]. Bands transmitted from 2850-3150 cm^{-1} and 1600 -1750 cm^{-1} may be ascribed to stretching vibrations of O-H and bending vibrations of adsorbed water molecules [192, 195]. The increased intensity of these bands in C-TiO_2 nanoparticles suggests more hydroxyl ions, which may be helpful in trapping of electrons to improve the separation efficiency of the electron-hole pair and can be beneficial for the photocatalytic degradation application [196].

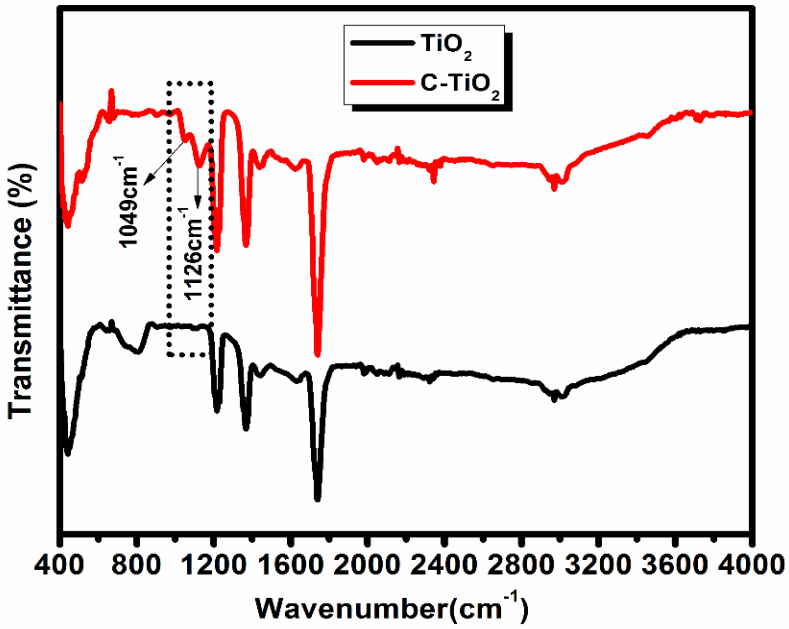

Fig. 5.7 FTIR spectra of TiO_2 and C-TiO_2 nanoparticles.

XPS is very sensitive technique to examine the chemical states of elements and elemental composition. XPS wide scan survey spectrum of TiO_2 and C-TiO_2 nanoparticles is shown in figure 5.8. High resolution XPS spectra of Ti (2p), O (1s), and S (2p) are shown in figure. 5.8 (b-d). The core level spectrum of Ti (2p) shows two peaks centred at 458.6 eV and 464.3 eV which can be ascribed to the binding energy of Ti ($2p_{3/2}$) and Ti ($2p_{1/2}$), respectively [197] and it should be assigned to Ti^{4+} of TiO_2[198]. The observed doublet separation between Ti ($2p_{3/2}$) and Ti ($2p_{1/2}$) peaks of 5.7 eV is a characteristic of TiO_2 [199]. Inset of figure 5.8 (b) represents the enlarged view of survey corresponding to Ti (2p). A small shoulder is clearly seen in C-TiO_2, which may be assigned to Ti^{3+}. The presence of Ti^{3+} may be ascribed to defects energy levels, indicates a reduction in the band gap which was also confirmed by UV-vis spectra. In C-TiO_2 nanoparticles the peak corresponding to Ti ($2p_{3/2}$) and Ti ($2p_{1/2}$) shifts towards the lower binding energy at 458.35 eV and 464.17 eV respectively. This shift may arise due to the difference in the ionization energy of titanium and sulfur.

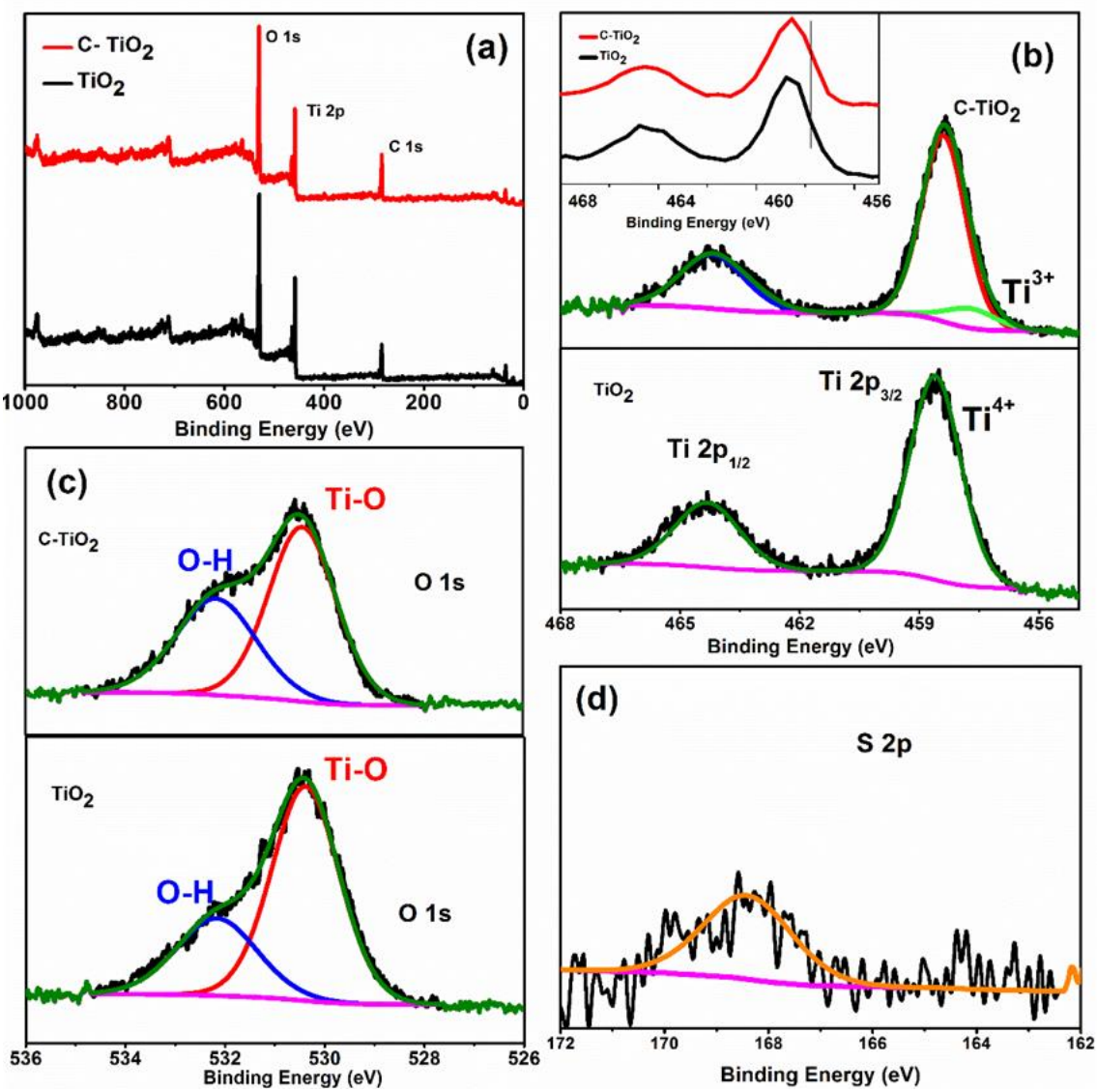

Fig. 5.8 (a) XPS survey and high resolution spectra for (b) Ti2p, (c) O1s, (d) S2p for TiO_2 and C-TiO_2 nanoparticles.

Figure 5.8 (c) shows O (1s) XPS spectrum which can be resolved into two peaks at 530.4 eV and 532.2 eV. The peak at 530.4 eV is an indicative of metal oxides arising from Ti lattice (Ti-O) and peak at 532.2 eV can be ascribed to surface hydroxyl (OH) species [200]. It is noticeable here that surface hydroxyl content in C-TiO_2 is more than that of TiO_2, which may be useful in photocatalytic activities. This is in good agreement with FTIR results also. A low intense peak at 168.4 eV for S (2p) was obtained only for the nanoparticles synthesized with 1-thioglycerol. The oxidation state of sulfur mainly depends on the sulfur precursor and the method of synthesis. The Peak at 168.4 eV confirms the presence of sulfur and can be assigned to the S^{+6} state [201]. So, it can be supposed that sulfur is dispersed over TiO_2 nanoparticles in chemical state S^{+6}. Based on XPS spectrum, O/Ti ratio is almost the same and it is suggested that TiO_2 and C-TiO_2 possess the same stoichiometry.

UV-visible absorption spectra of TiO_2 and C-TiO_2 nanoparticles is shown in figure 5.9. It is clear from absorption spectra that TiO_2 and C-TiO_2 nanoparticles show the intense absorption in the UV range of the spectrum with the absorption edge near visible region. On addition, the 1-thioglycerol a discernible red shift in absorption edge has been observed. Optical energy band gap was calculated by Tauc's relation (equation 5.2) between band gap and absorption coefficient

$$\alpha h\nu = A(h\nu - E_g)^2 \tag{5.2}$$

Where, α and E_g represent the absorption coefficient and energy band gap respectively. A is a constant, $h\nu$ is the energy of the incident photon. The value of n depends on the nature of electronic transition responsible for the reflection i.e. 1/2 for allowed direct transition, 3/2 for forbidden direct transition, 2 for allowed indirect transition and 3 for the forbidden indirect transition. Inset of figure 5.9 shows Tauc's plot for the calculation of optical energy band gap of TiO_2 and C-TiO_2 nanoparticles. Extrapolation of the tangent on the graph gives the value of energy band gap and it was calculated as $\sim 3.19\ eV$ and $\sim 2.91\ eV$ for TiO_2 and C-TiO_2 nanoparticles. Indirect band gap of anatase titania was taken into account. The reason for narrowing band gap may be the contribution of p states of S by mixing with O (2p) states of TiO_2 or defects energy levels. Decreased band gap may be useful for many applications such as photovoltaic device, photocatalytic activity.

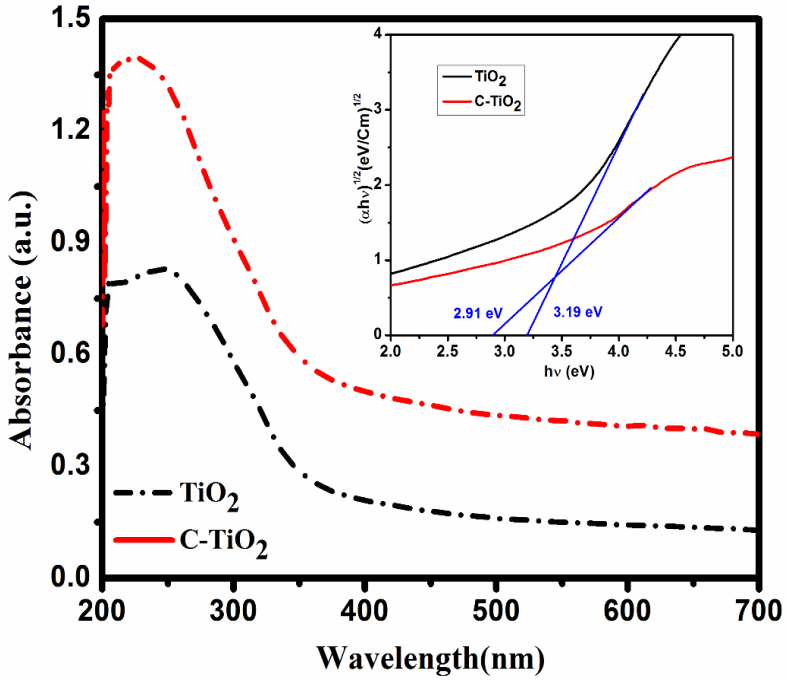

Fig. 5.9 UV-visible absorption spectrum of TiO_2 and C-TiO_2 nanoparticles and Tauc's plot (inset).

5.3.3 Effect of capping agent on thermal stability

The growth of TiO_2 nanoparticles mainly depends on hydrolysis and condensation to form Ti-O-Ti networks [202]. In order to observe the effect of capping agent on the crystallite size, crystallinity, and phase of the nanoparticles, both the samples were characterized by XRD. Phase formation of TiO_2 nanoparticles depends on their annealing temperature also. In this study, both the nanoparticles were further isochronally annealed at different temperatures from 500°C to 800°C to examine the thermal stability of 1-thiglycerol capped nanoparticles. Figure 5.10 shows the XRD patterns for TiO_2 and C-TiO_2 nanoparticles annealed at different temperatures. The intensity of peaks in all the samples reflects the crystalline behaviour of TiO_2 nanoparticles, and from figure. It is clearly observed that the intensity of the peaks increases with the increase in annealing temperature which shows the increasing crystallinity of the nanoparticles with annealing temperature. FWHM of the peaks are decreasing with annealing temperature which clearly indicates the increment in particle size and it as calculated using equation (5.1). Variation of particle size with annealing temperature is shown in figure 5.11. The particle size was found to be lower with capping agent at each annealing temperature as compared to without capping agent. From the slope of the line fitted, it can be concluded that the rate of growth of particle size is lower in C-TiO_2 nanoparticles. Quantification of phase proportions in an anatase rutile mixture usually carried out by the method of Spurr and Myer as follows in following equation [203].

$$f_R = \frac{1}{1 + 0.8\frac{I_A}{I_R}} \tag{5.3}$$

Where f_R are fraction of rutile phase in anatase-rutile mixture. I_A & I_R represent the intensity of most intense peak in XRD pattern corresponding to anatase and rutile phase respectively. Upto 500°C, both the samples are in the anatase phase of TiO_2. At 600°C, TiO_2 nanoparticles are found in a mixed phase of anatase and rutile while C-TiO_2 are still in pure anatase phase. The onset temperature for the rutile transformation is found to be raised from 600°C to 700°C and the anatase phase retained up to higher temperature. Without 1-thioglycerol TiO_2 transforms into rutile phase completely at 800°C, while with capping agent still a mixed phase is present. So, thermal stability of anatase phase has increased when the nanoparticles were synthesized with 1-thioglycerol.

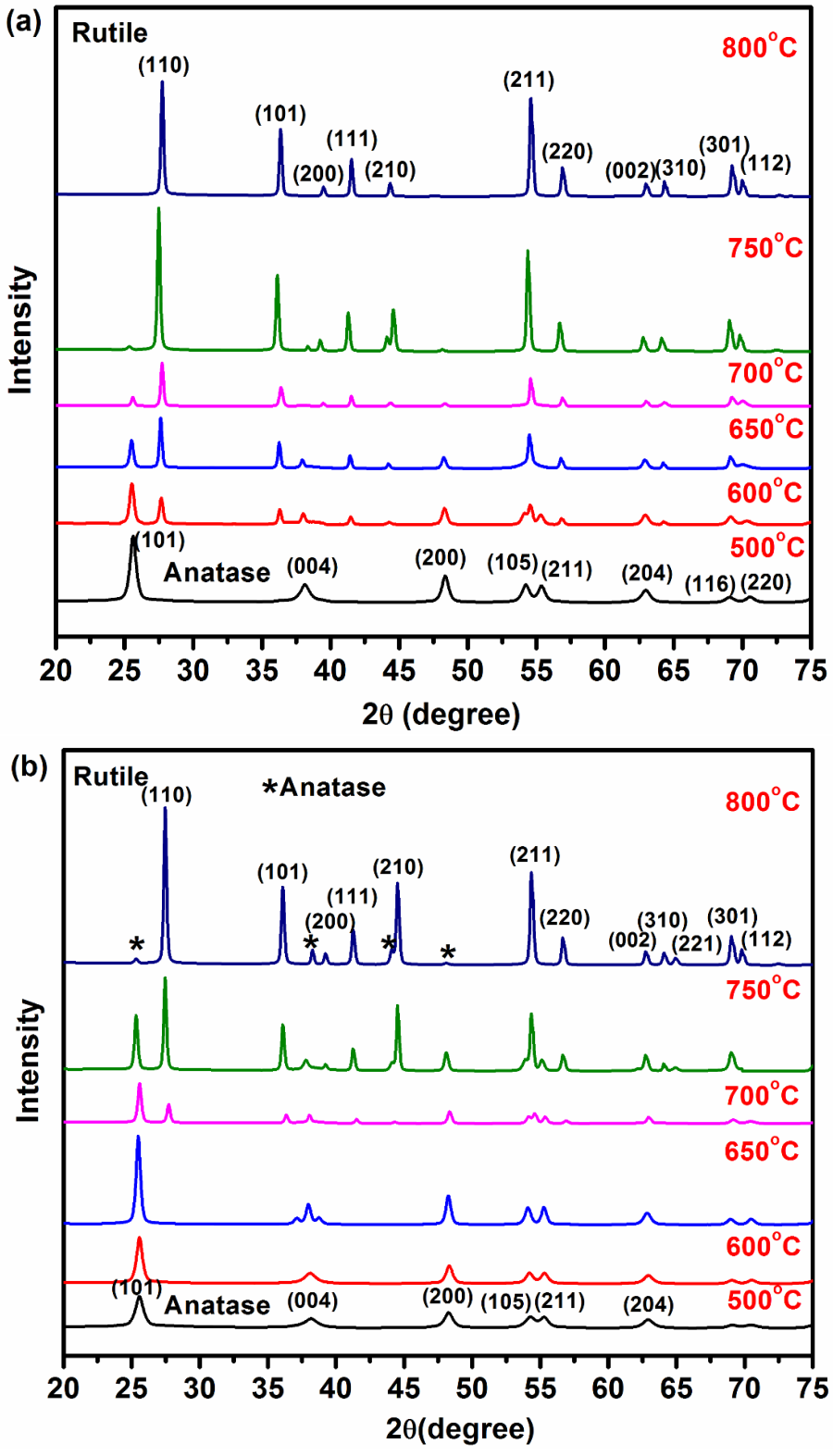

Fig. 5.10 XRD pattern of (a) TiO_2 and (b) C-TiO_2 nanoparticles annealed at different temperatures (500°C to 800°C).

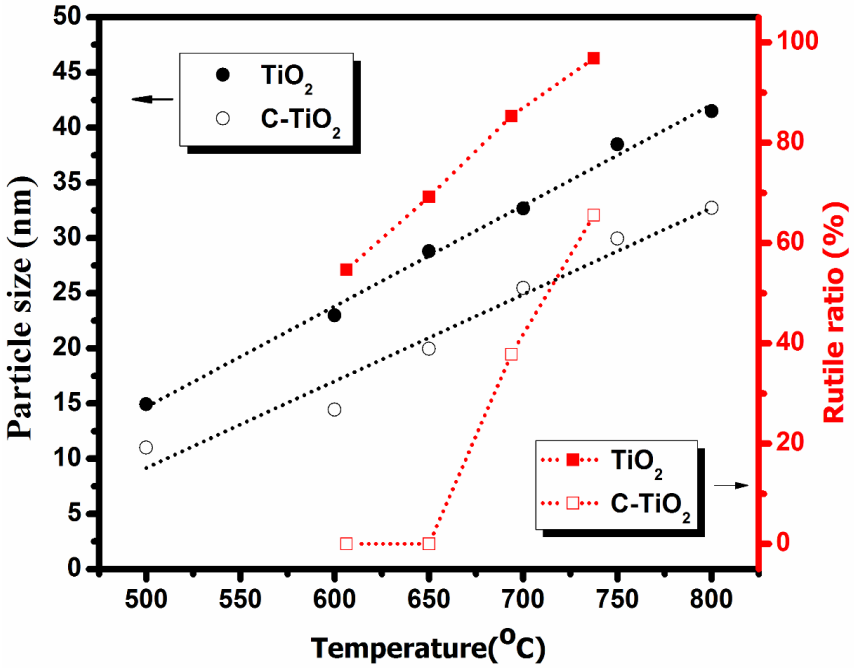

Fig. 5.11 Variation of particle size and ratio of rutile phase with annealing temperature.

XRD results were also corroborated by Raman spectra (figure 5.12). Anatase TiO_2 shows the Raman active fundamental bands at 144 cm^{-1} (E_g), 197 cm^{-1} (E_g), 399 cm^{-1} (B_{1g}), 513 cm^{-1} (A_{1g}), 519 cm^{-1} (B_{1g}), and 639 cm^{-1} (E_g) [185] and rutile TiO_2 shows the bands at 143 cm^{-1} (B_{1g}), 237 cm^{-1} (B_{2g}), 447 cm^{-1} (E_g), and 612 cm^{-1} (A_{1g}) [186]. In our samples annealed at temperature 500°C Raman bands at 144 cm^{-1} (most intense), 197 cm^{-1} (a small peak), 396 cm^{-1}, 514cm^{-1}, and 639 cm^{-1} are obtained which confirm the pure anatase phase of TiO_2. As the annealing temperature increases up to 700°C the intensity of these Raman bands in C-TiO_2 increases which is due to increase in the crystallinity while in TiO_2 intensity of these bands decreases which indicates the phase transformation from anatase to rutile. The bands at 447 cm^{-1} and 612 cm^{-1} in TiO_2 at 600°C confirms the rutile phase while in C-TiO_2 these bands are obtained at annealing temperature 700°C. It is in accordance with XRD results that the onset temperature for phase transformation has been raised while using 1-thioglycerol. At 800°C, second order features for rutile phase are also occurred at 237 cm^{-1} [204] and all the bands corresponding to anatase phase are disappeared which clearly shows the transformation from mixed phase to pure rutile phase.

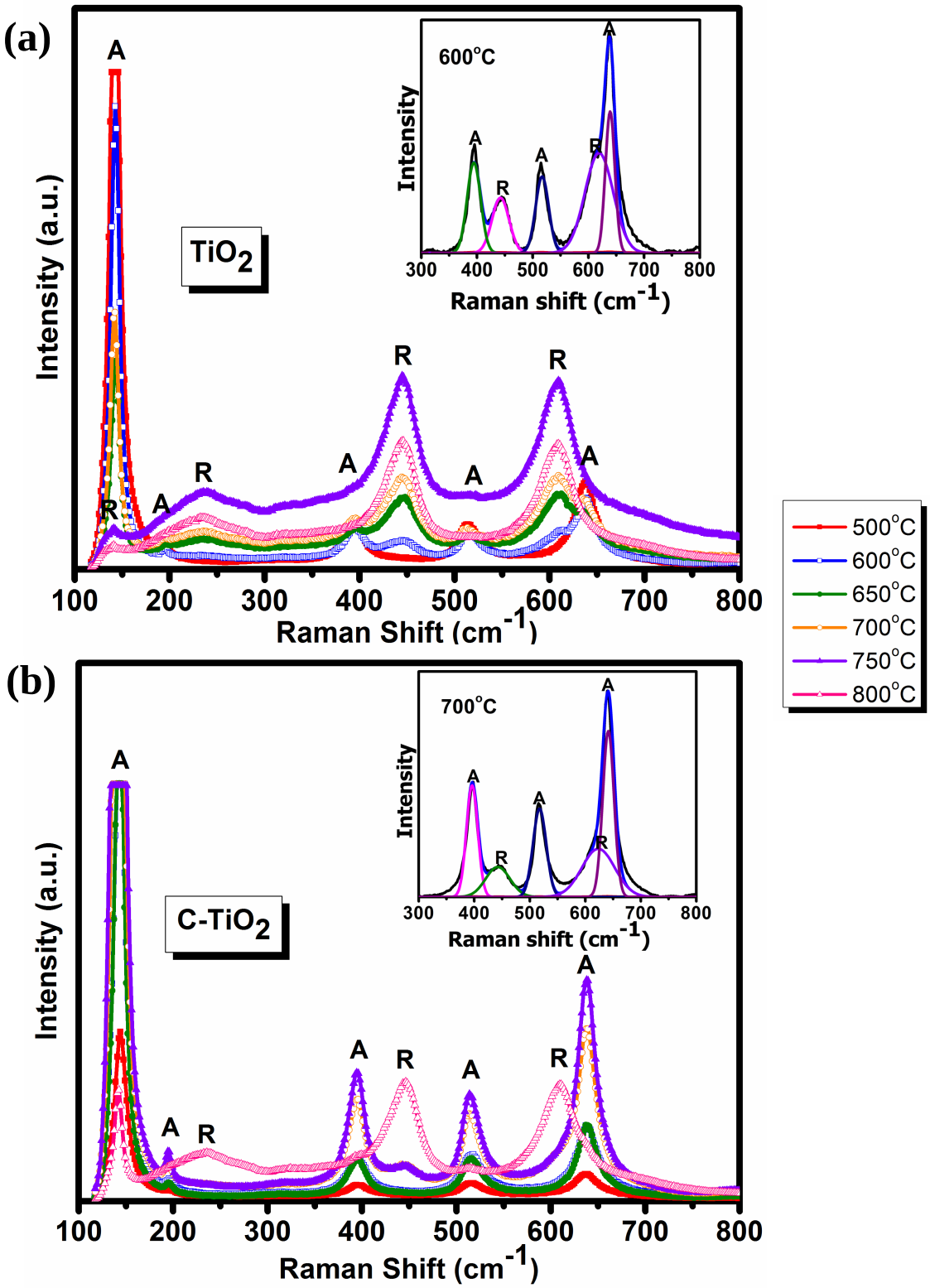

Fig. 5.12 Raman spectra of TiO_2 and C-TiO_2 nanoparticles annealed at different temperatures (500°C to 800°C).

5.3.4 Optimized size of TiO_2 nanoparticles

From the above discussion, it has been concluded that the particle size is decreased when the capping agent has been used and it increases with annealing temperature. The least optimized particle size is $\sim 9\ nm$ at 350°C with capping agent (C-TiO_2). For the successful deposition into the templates, particle size further need to be reduced. It can be done by annealing of C-TiO_2 nanoparticles at lower temperature. C-TiO_2 nanoparticles were annealed at 250°C for 1 hour and characterized by XRD and TEM to calculate their size and crystallinity. Figure 5.13 shows the XRD pattern and TEM image with SAED pattern of C-TiO_2 nanoparticles. Average particle size was calculated $\sim 5\ nm$ from XRD and corroborated with TEM also. SAED pattern shows the polycrystalline nature of nanoparticles. Now these nanoparticles are suitable for the successful selective deposition into templates of size $\sim 15\ nm$. The process and the results for the deposition of these nanoparticles into templates have been discussed in next chapter.

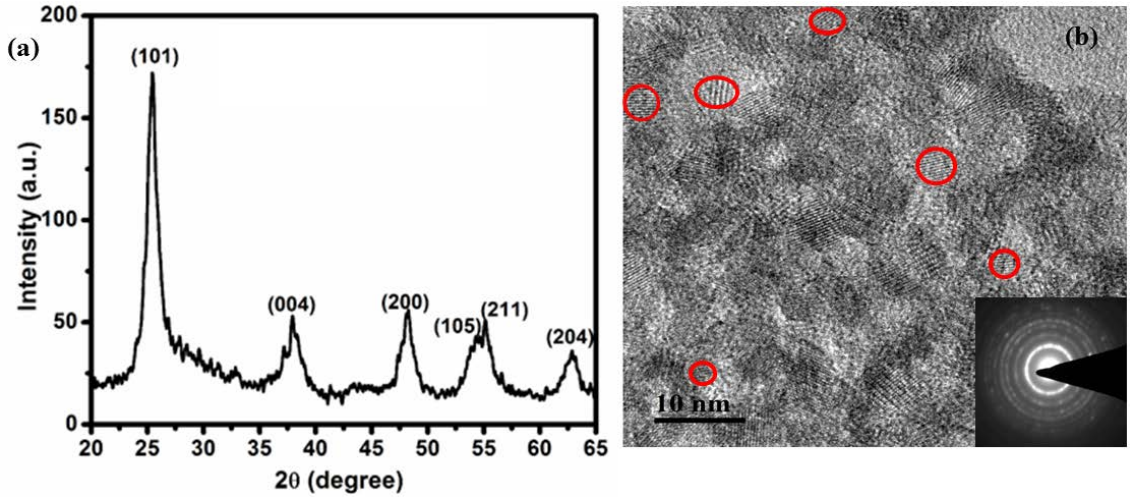

Fig. 5.13 XRD pattern (a) and TEM image (b) with SAED pattern (inset) of C-TiO_2 nanoparticles annealed at 250°C

5.4 Conclusions

TiO_2 nanoparticles have been synthesized by sol-gel method for the deposition into the templates for the fabrication of ordered TiO_2 nanostructures. Initially the particles size was calculated as $\sim 13\ nm$ from XRD and the same results were found from TEM also. This particle size is not appropriate for the deposition, so it is to be reduced. For the reduction in the size in sol-gel method, capping agent (1-thioglycerol) was used. The binding of the capping agent with nanoparticles was confirmed with FTIR. The presence of sulfur from the thiol group of capping agents was confirmed with XPS. Ti was present as Ti^{+4} in TiO_2 while in C-TiO_2, Ti^{+3} was also present along with Ti^{+4} which may be responsible for the defect energy levels.

These defect energy levels may reduce the energy band gap also which was calculated by Tauc' plot using UV-visible spectroscopy. Major role of capping agent is to inhibit the growth of nanoparticles and the average particle size was decreased from ~ 13 nm to ~ 9 nm at annealing temperature of 350°C. Then, it was investigated that on increasing the annealing temperature, particle size also increases but the growth rate of particle size becomes slower with capping agent than that of without capping agent. Phase transformation also occurred when the annealing temperature increases and anatase phase of TiO_2 transforms into a mixed phase of anatase and rutile at 600°C. This phase transformation occurs at 700°C in C-TiO_2 which suggest that the anatase phase of nanoparticles is more stable with the capping agent. Further, the reduction in the particle size of C-TiO_2 was done by annealing at lower temperature with capping agent. C-TiO_2 nanoparticles were annealed at 250°C for 1 hour. The average particle size was calculated as ~ 5 nm which is appropriate for the deposition into the nanotemplates. So, the optimization of size and phase of TiO_2 nanoparticles have been discussed in this chapter.

Chapter 6

Fabrication of Ordered Nanostructures

6.1 Introduction

Inorganic nanostructures provide the pathways for the charge carriers and play a major role for the improvement in the efficiency of solar cells. For this purpose, nanostructures must be highly ordered and in the range of exciton diffusion length. The suitability of the energy levels of TiO_2 with various conducting polymers and dyes renders them appealing for solar cells. In addition to that, ordering of TiO_2 nanostructures supports the better charge transportation to the respective electrodes and contribute to the enhancement of the power conversion efficiency (PCE) [35, 205] Ordered assemblies of nanomaterials in 1D, 2D, and 3D, can be produced by bottom-up technique which has been recognized as a well-designed and powerful approach [206–209]. The flexibility in the selection of inorganic material and the arrangement of molecules make these approaches versatile over the well-known top-down lithographic techniques. Particularly, block copolymers pattering represents a most promising technique for the fabrication of ordered inorganic nanostructures (metal/metal oxide nanoparticles, nanorods, quantum dots) due to their self-assembly into a variety of well-ordered nanoscale periodic patterns with a typical dimension of $5 - 100\ nm$ [210, 211, 116, 4].

Nanostructures can be fabricated by either *in-situ* or *ex-situ* approach. L. Song *et al.* have used *in-situ* method for the synthesis of titania nanoparticles using the titanium isopropoxide as a TiO_2 precursor and loading the precursor in poly(styrene)-b-poly(4-vinylpyridine) (PS-*b*-P4VP) solution [103]. The authors have demonstrated that the concentration of titania precursor alters the resultant morphology. In this chapter, both *in-situ* and *ex-situ* approach have been adopted. *Ex-situ* approach has found more controllable and efficient because the properties of the pre-synthesized nanoparticles can be tailored easily. In *ex-situ* approach, selective incorporation of

nanoparticles in on of the blocks of block copolymer is an easy process, but it is less attractive because it enhances the tendency of agglomeration of nanoparticles and form the clusters [212] and the morphology will also be altered at a particular concentration of nanoparticles loading [213]. To retain the same structure as that of block copolymer domains and to avoid the cluster formation, direct deposition of nanoparticles (*ex-situ*) into the templates is an effective approach to fabricate the well-ordered nanoparticles array with high fidelity. Stamm and co-workers have reported the metal nanopatterning through the deposition of nanoparticles (*ex-situ*) into the templates because of their easy dispersion in a solvent [109, 112]. But for metal oxides, agglomeration of nanoparticles is a hurdle for selective deposition into the templates and not explored yet.
To conquer with this obstacle, we herein made an effort to subdue the agglomeration by sonication during deposition and a well-ordered array of TiO_2 nanodots has been obtained by incorporating the pre-synthesized nanoparticles into the templates. This approach is versatile and can be applied to the other metal oxides nanostructures also.

6.2 Experimental details

Fabrication of nanotemplates has been discussed in chapter 4. Prepared nanotemplates were then backfilled by 1) titania precursors and 2) direct deposition of nanoparticles. Subsequently, the templates were characterized by AFM and SEM to observe the morphological behavior.

6.2.1 Filling the titania precursor into templates

Prepared nanotemplates were then dipped into sol of titania precursors in ethanol. Titanium tetra isopropoxide was mixed in ethanol in the ratio of 2:1, 3:1 and dipped for 5 and 30 seconds. Both types of templates (Cylindrical and lamellar structure) were used.

6.2.2 Deposition of nanoparticles into the templates

Cylindrical porous nanotemplates were used for the fabrication of ordered nanodots. Templates were immersed into the aqueous solution of TiO_2 nanoparticles. Synthesis of TiO_2 nanoparticles has been described in detail in section 5.2. For the deposition of nanoparticles, 0.05 gm powder of pre-synthesized TiO_2 nanoparticles was dispersed in 20 ml of deionized water with sonication and then filtered through 0.2 μm PVDF filter two times. The filtered solution becomes colorless from the milky white solution which shows the presence of dispersed nanoparticles and indicated the reduction of agglomeration. The templates were dipped into the filtered solution for 6-12 hours

under the sonication. Continuous sonication reduces the problem of agglomeration of metal oxide nanoparticles.

6.2.3 Removal of polymer template

In the next step, polymer templates were removed by two ways; exposure to UV irradiation for 48 hours and calcination at 450°C for 1 hour.

6.3 Results and discussion

6.3.1 *In-situ* approach

In the case of *in-situ* approaches for the deposition of inorganic nanomaterials, templates are to be backfilled with the sol of inorganic materials. TTIP is commonly used as a precursor for TiO_2. Here, the templates were dipped in the solution of TTIP and they were expected to be filled with the TTIP. TTIP can easily be hydrolyzed with the moisture and form titanium hydroxide ($Ti(OH)_4$). It is easily transformed into TiO_2 on heating. Simultaneously, heating will remove the template also and leave the TiO_2 network on the substrate. Before heating, the filled templates were exposed to the UV irradiation for 2 hours to provide stability to the template so that melting and evaporation of the polymer do not affect the arrangement of TiO_2 nanostructures.

PS-*b*-P4VP (35.5 *kg/mol* - 4.4 *kg/mol*)

Figure 6.1 shows the SEM image of nanotemplates (cylindrical) on immersing into the TTIP solution for 5 sec. The TTIP was dissolved in ethanol in a ratio of 2:1. From the figure it can be estimated that a layer of TiO_2 with some cracks has been coated over the templates. In the magnified image, the layer of nanoparticles can be easily seen over the nanotemplates.

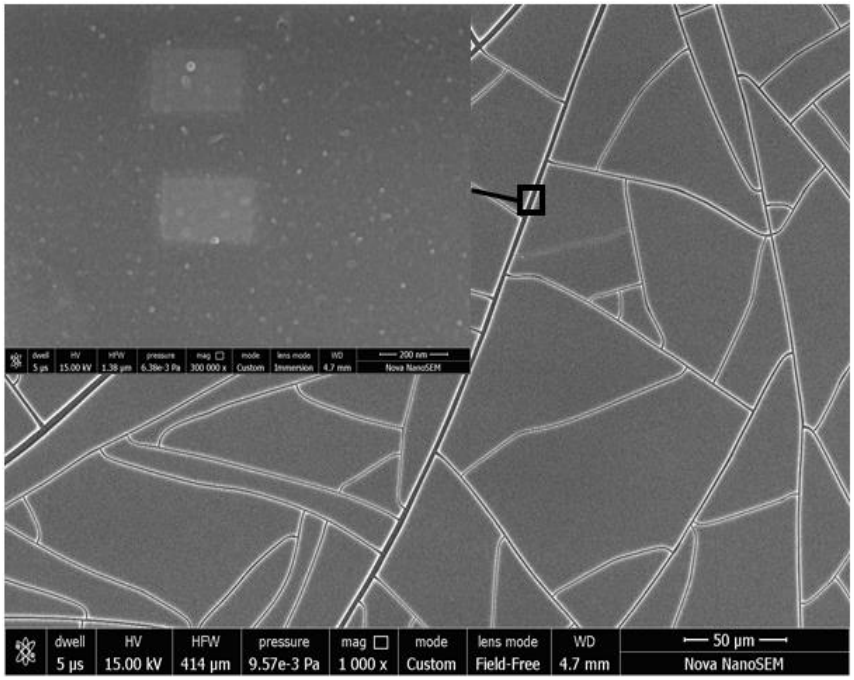

Fig. 6.1 SEM image of templates (mol. wt. 35.5 kg/mol - 4.4 kg/mol) filled with TTIP solution for TTIP: ethanol::2:1.

PS-*b*-P4VP (33.0 *kg/mol* - 8.0 *kg/mol*)

Templates with the lamellar structures were also filled with the TTIP solution, and it was observed from figure 6.2 that a layer of TiO_2 nanoparticles had covered the surface of the templates. Though from the figure it is not clear whether these nanoparticles are filled into the pores also or the templates are overlayered with TiO_2. Then, the templates were heated at temperature $450°C$ for one hour so that the polymer can be removed. Figure 6.3 shows the resultant TiO_2 network after heating the templates. It can be inferred from the image that the polymer has been removed and TiO_2 is deposited on the substrate, but it is not the same as the templates. However, it is interesting to see that the size or the width of TiO_2 connecting network is in the range of $10\ nm - 20\ nm$. So, one can conjecture that obtained TiO_2 network is deposited through the template which confirms the filling of channels with the precursor. But, the obtained network is different than the lamellar structures of the templates (shown in inset of figure 6.3) which may be due to the formation of a continuous layer of TiO_2 over the template. Moreover, dark patches of around 100 nm are also observed where the TiO_2 is not present. This inhomogeneity may be attributed to the melting of the polymer by heating. Although, the filled templates were exposed to UV to avoid this disturbance, it still occurs. So, the heating ramp rate may also be responsible for this irregular network of TiO_2.

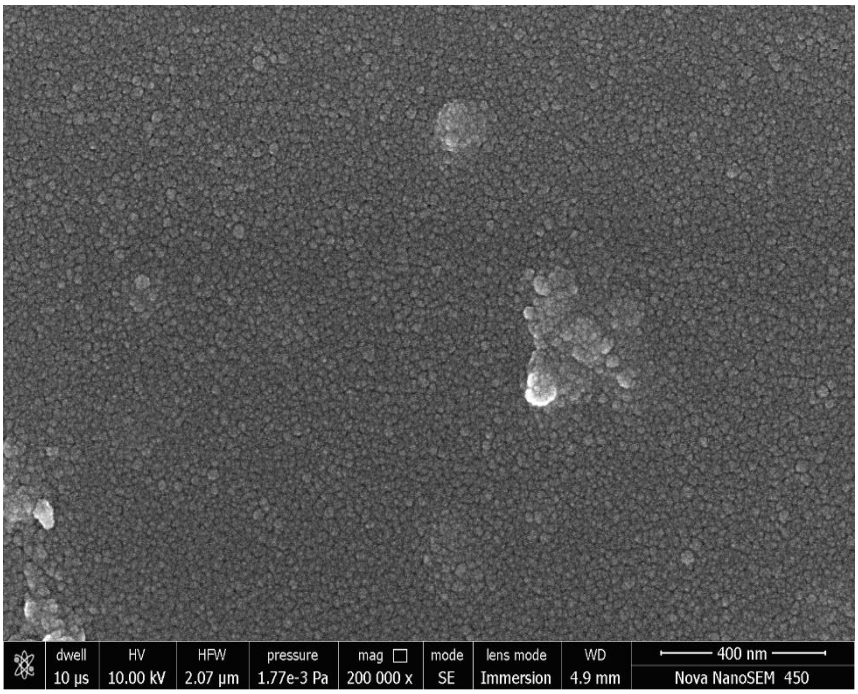

Fig. 6.2 SEM image of templates (mol. wt. 33.0 kg/mol - 8.0 kg/mol) filled with TTIP solution for TTIP: ethanol::3:1.

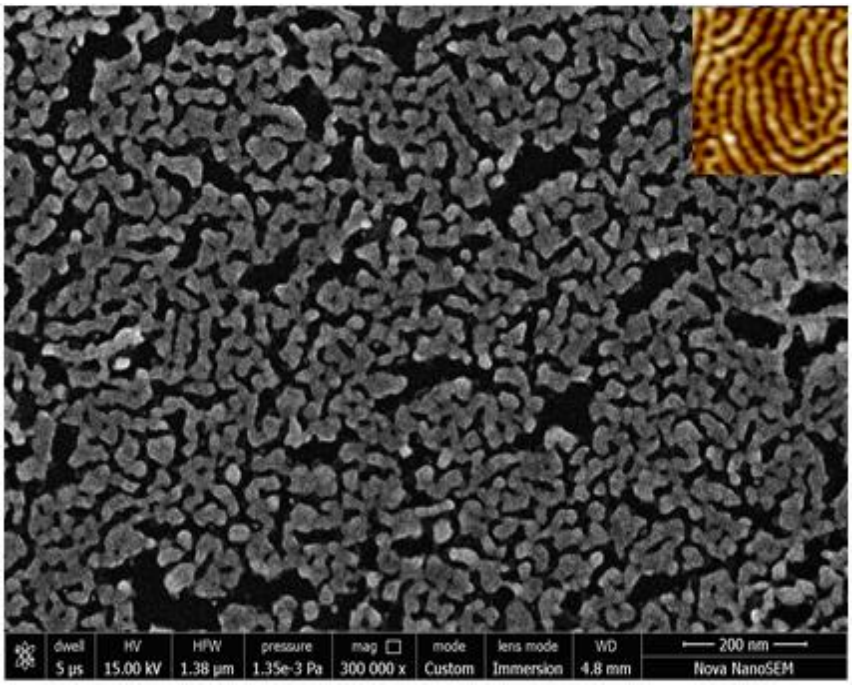

Fig. 6.3 SEM image of TiO_2 network obtained after removal of templates (mol. wt. 33.0 kg/mol - 8.0 kg/mol) by heating at 450°C. Inset shows a glimpse of the bare template.

PS-*b*-P4VP (130.0 *kg/mol* - 75.0 *kg/mol*)

Figure 6.4 shows the SEM image of a connecting network of TiO_2 prepared using the templates with cylindrical morphology and large pore size following the same steps (filled with TTIP and subsequent removal of the polymer by heating). However, a careful observation illustrates that the TiO_2 is deposited in the form of rings and these rings are interconnected to each other and forming a continuous network. It may be assumed that the titanium of TTIP is attached to walls of pores which is lined with the functional group of P4VP. In this case, the outer diameter of this ring-like structure is expected to be same as the diameter of pores. But it has a variation from values of the diameter of pores, the reason may be the same as explained in the section 6.3.1 (heating ramp rate and continuous layer of TiO_2).

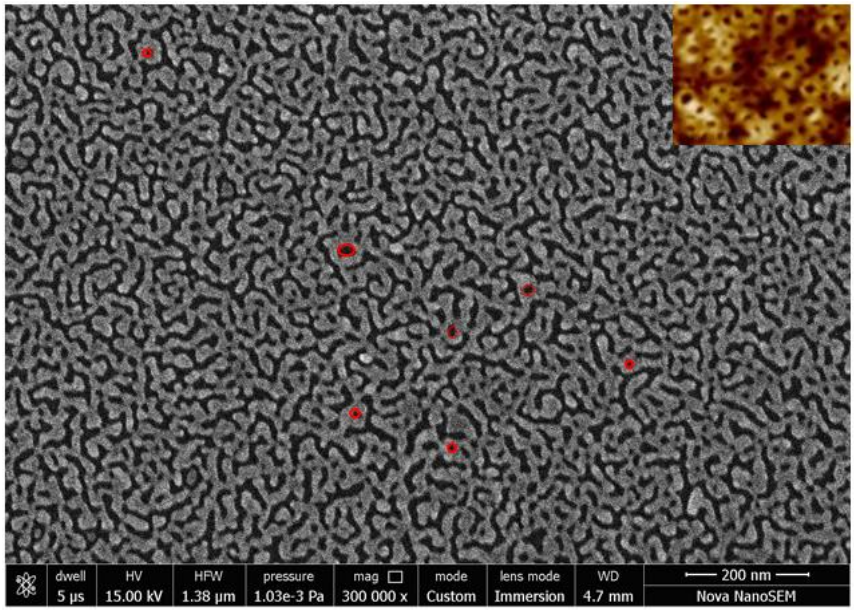

Fig. 6.4 SEM image of TiO_2 connecting network obtained after removal of templates (mol. wt. 130.0 kg/mol - 75.0 kg/mol) by heating at 450°C. Inset shows a glimpse of the bare template.

The inner diameter of these ring-like structures is much lesser than the diameters of pores created in the template, and it is in the range of approximately 5 - 20 nm with a wall thickness varied from about 10 - 30 nm. Although the obtained nanostructures are not orderly arranged but the dimension of the deposited network lies in the range from 5 to 30 nm which is in the range of exciton diffusion length, and it provides the large surface area also. So, it can play a good role in the enhancement of efficiency of the solar cell like dye-sensitized solar cell and polymer solar cell.

6.3.2 *Ex-situ* approach

Schematic of the process for *ex-situ* deposition, followed in the present study is depicted in figure 6.5.

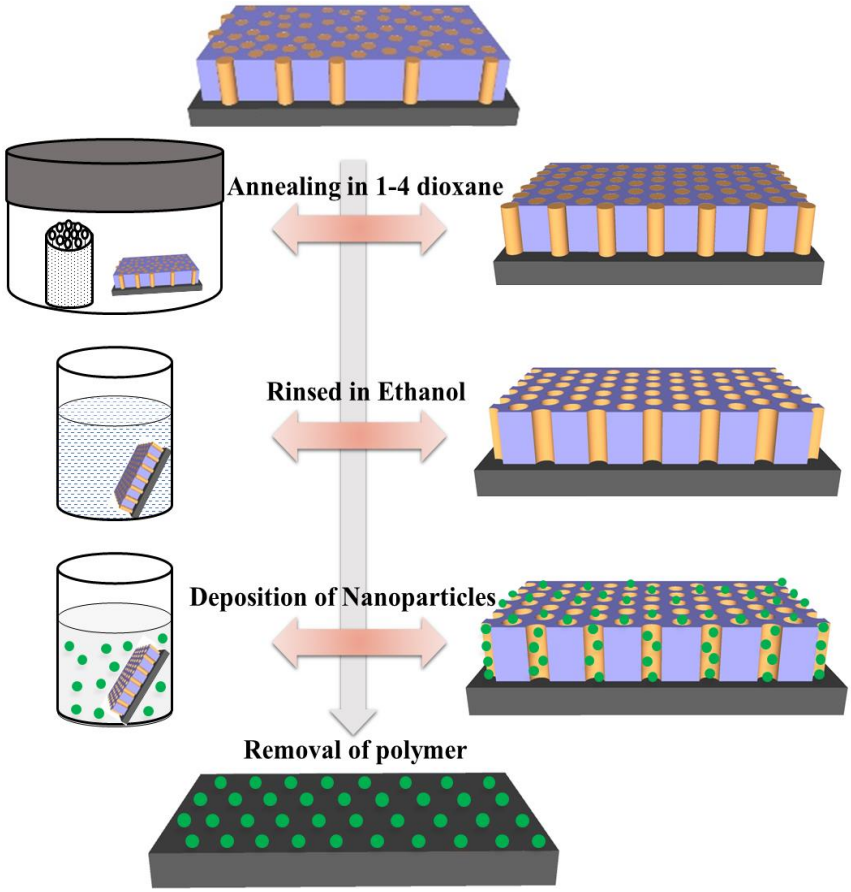

Fig. 6.5 Scheme for the fabrication of ordered TiO_2 nanodots.

In the first step, PS-*b*-P4VP was mixed with HABA homogenously for Supramolecular assembly with P4VP:HABA::1:1 and 1 wt% solution. The thin films were deposited on Si substrate from the prepared solution using dip coating technique. Carboxylic group of HABA reacts selectively with the pyridine group of P4VP by hydrogen bonding. The ordering in the thin films of Supramolecular assembly was performed by placing the films in a glass chamber containing 1-4 dioxane vapors. P4VP/HABA cylindrical domains are surrounded by PS matrix. Second, cylindrical pores were created by rinsing the ordered thin films into ethanol which leads the selective extraction of P4VP/HABA as it is a good solvent for P4VP/HABA cylinders and non-solvent for PS matrix. Surface reconstruction leads the nanotemplates with cylindrical pores lined with the P4VP functional group. Third, these nanotemplates were dipped into the aqueous solution of pre-synthesized nanoparticles, and the nanoparticles were allowed to enter into the hexagonally arranged cylindrical pores by the diffusion and the capillary forces. This step was performed in the ultrasonic bath to avoid the agglomeration of nanoparticles and blocking of the pores. In the last step, the polymer matrix was removed by heating/UV irradiation and leaving the self-assembled nanodots onto the substrate with the high fidelity. Morphology of as-deposited and solvent annealed thin film of Supramolecular assembly on surface reconstruction by immersing in ethanol has been discussed in section 4.3.1. The

average pore diameter was calculated as $15 \pm 1\ nm$ with an average center to center distance of $35 \pm 1\ nm$ shown in figure 6.6. Unlike to the metal nanoparticles, metal oxide nanoparticles agglomerate and settle down very fast which is unfavorable for the successful deposition of nanoparticles into the pores. Nanoparticles were mixed with deionized water under sonication and subsequently filtered with 0.2 μm PVDF filter two times. Obtained aqueous solution of nanoparticles becomes transparent from milky white solution, which suggests the dispersed nanoparticles into the solution. In addition to above, the nanoparticles solution was sonicated during the deposition also, to lessen the agglomeration and cluster formation.

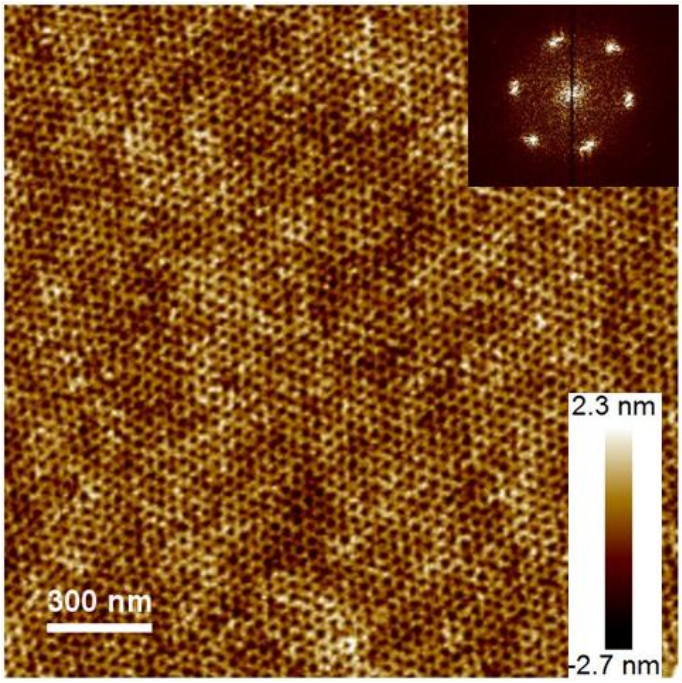

Fig. 6.6 AFM image of ordered nanoporous template. FFT of image is shown in inset.

The Supramolecular assembly nanotemplates were immersed into the sonicated and filtered aqueous solution of pre-synthesized TiO_2 nanoparticles for 6, 9 and 12 hours. The templates were removed from the nanoparticles solution and then washed with deionized water to remove the nanoparticles, weakly attached to PS matrix. After deposition of nanoparticles into the templates, polymer matrix was removed by two different ways. The polymer-TiO_2 film was exposed to UV irradiation, and selectively polymer was removed leaving the ordering of nanostructures intact. Alternatively, calcination at $450°C$ was performed to burn away the polymer as it is much higher than the glass transition temperature of both the blocks (PS and P4VP). Calcination improves the crystallinity of TiO_2 nanostructures.
Figure 6.7 represents the AFM and SEM images of templates after dipped into the solution for different time and followed by UV exposure for 48 hours. From the surface morphology in AFM image corresponding to 6 hours immersion time, any

exact information for the deposition of nanoparticles cannot be extracted. However, SEM image for the same sample clearly showed the array of nanodots. The poor contrast may be attributed to the lower crystallinity and low density of TiO_2.
As the immersion time increased to 9 hours, AFM image shows the unambiguous deposition of TiO_2 nanoparticles into the templates.

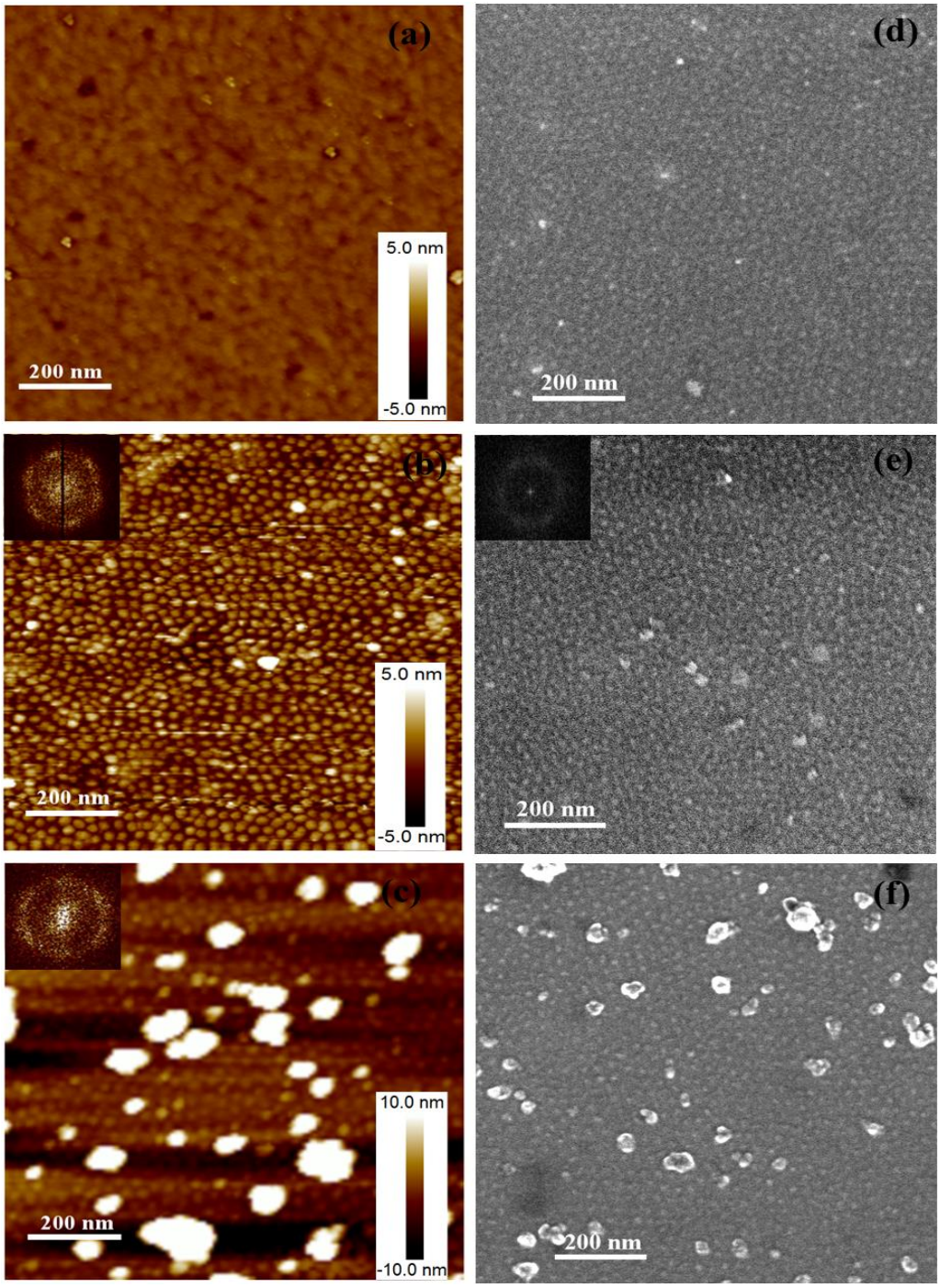

Fig. 6.7 AFM and SEM images of an array of nanostructures for (a, d) 6 hours (b, e) 9 hours (c, f) 12 hours immersion time after removal of the polymer by UV treatment.

Six reflections in the FFT (inset figure 6.7 (b & e)) confirms fidelity/exactness of nanodots with the hexagonal lattice of pores. Same inferences were drawn from the SEM image for the same sample. Further increasing the immersion time leads the coagulation of nanoparticles at some points. Bright contrast in AFM and SEM images was due to TiO_2 rich area. However, ordering in the deposited nanostructure is still intact, confirmed by FFT (inset figure 6.7 (c)). In the present study, optimal immersion time could be proposed 9 hours.

The mechanism for the deposition of TiO_2 into the cylindrical pores of templates can be proposed as follows. The first and most important condition for the direct deposition of pre-synthesized nanoparticles is the size of the nanoparticles which should be smaller enough than the pore size which is satisfied in the present study. However, in the case of transition metal oxides, especially TiO_2, the agglomeration of nanoparticles is a hurdle which has been subdued here by filtration and sonication during the deposition. So, in the present case, the diffusion of nanoparticles into the pores is tuned. Second, the selection of the solvent for the dispersion of nanoparticles is also important. It should not perturb the structure of templates, and it is required to allow the wetting of pores exclusively. In this regard, the aqueous solution of nanoparticles is advantageous in the present study. Since P4VP is hydrophilic and PS is hydrophobic, so the solution of nanoparticles readily wet the pore walls because the pores are lined with the P4VP functional group. The solution could not be swollen the PS matrix, and the structure remains intact after deposition of nanoparticles into the pores. Once the pore walls get wetted by the solution, the nanoparticles were then allowed entering into the pores by the capillary force. Additionally, coordination of the nanoparticles with pyridine group lined in the pore walls plays a crucial role which further promotes the deposition of nanoparticles into the pores.

The coordination of anatase TiO_2 with pyridine has been studied in detail by T. Bezrodna *et al.* [214]. The average diameter of TiO_2 nanodots and their distribution are shown in figure 6.8. The diameter of TiO_2 is found in the range from 10 - 25 nm with a mean diameter of 15 ± 1 nm. Cross-section analysis was also performed collect the information of size, centre-to-centre distance and their distribution which is consistent with the results obtained from particle analysis and PSD pattern (Figure 6.9). In the array of TiO_2 nanostructures, the center-to-center distance between neighbouring TiO_2 were obtained from the peak position in PSD analysis of AFM images. The peak in curve (a) in figure 6.9 is corresponding to the centre-to-centre distance of consecutive pores in the ordered template which is ~ 35 nm. The peak position is nearly same ~ 34.2 nm when the nanoparticles were deposited for 9 hours (figure 6.9, curve b) which confirm the fidelity of nanostructures with the template. However, on increasing the immersion time to 12 hours (figure 6.9, curve c), no peak was observed in PSD pattern which may be ascribed to agglomeration and cluster formation of nanoparticles which hinders the periodicity of nanostructures.

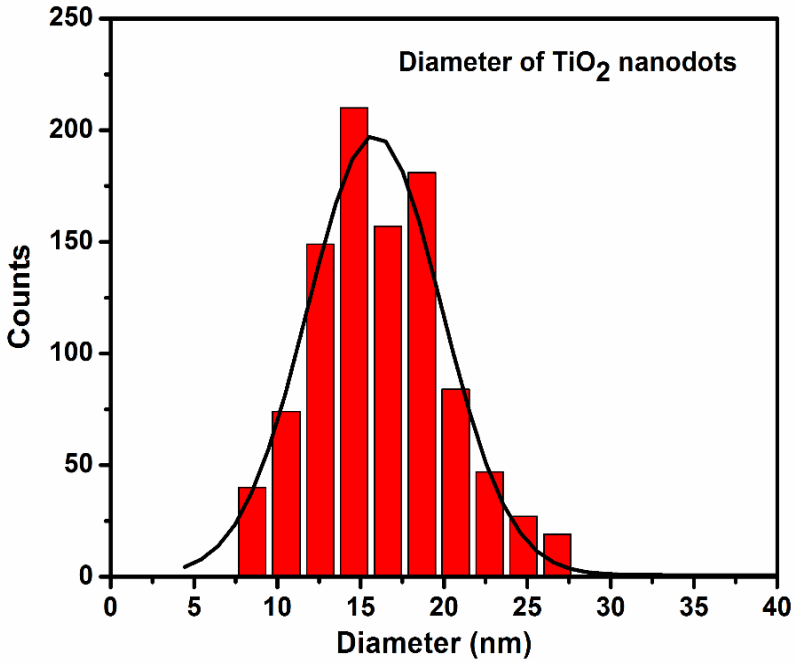

Fig. 6.8 The distribution of diameter of TiO_2 nanodots deposited.

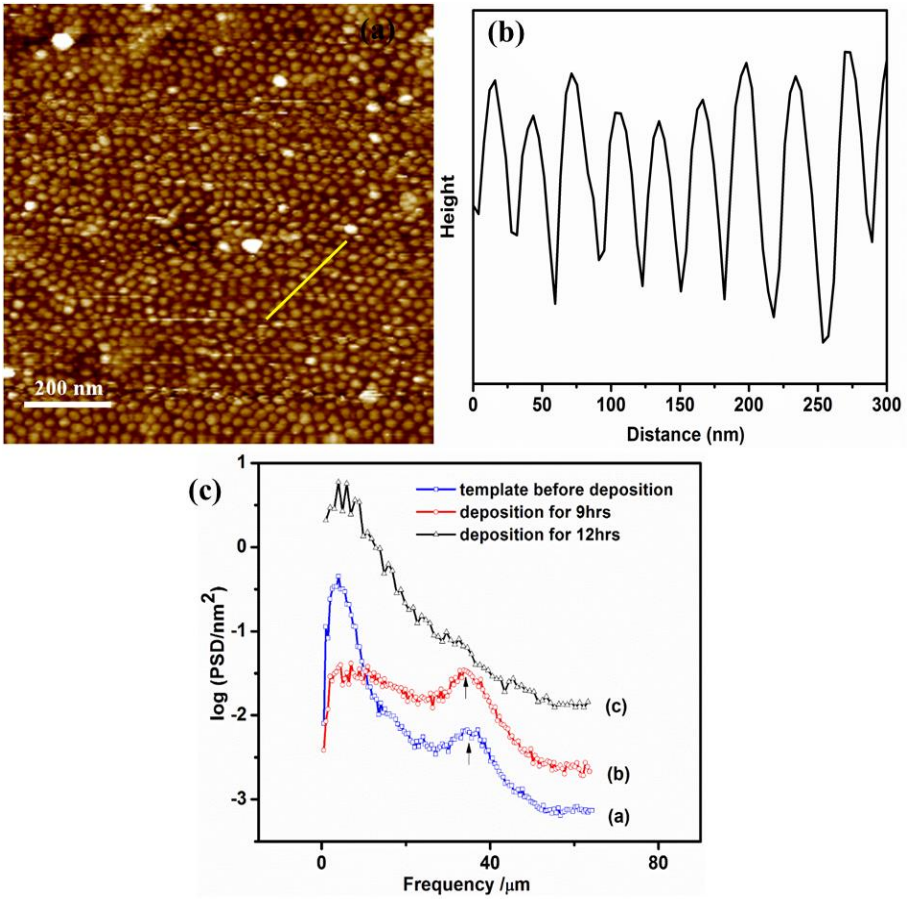

Fig. 6.9 (a) AFM image of array of TiO_2 nanodotes (b) section profile along the line shown in (a) (c) Power spectral density profiles of PS-*b*-P4VP templates (curve a), an array of TiO_2 nanostructures for different immersion time; 9 hours (curve b) and 12 hours (curve c).

An array of nanostructures was examined by AFM and SEM after removing the polymer by calcination also (figure 6.10). The formation of larger aggregates of TiO_2 during heating at 450°C was observed in the images. The reason for the aggregated TiO_2 may be the short interparticle distance which does not prevent the agglomeration efficiently during heating. Another possibility may be high ramp rate of heating (8°C min^{-1}) due to which the polymer melts before burning out and perturb the arrangement of TiO_2 nanostructures. However, the shape of each TiO_2 dot is preserved after heating. In contrast to the formation of aggregates on heating, UV treatment of polymer-TiO_2 hybrid films does not show a remarkable change in the large-scale structure. As shown in figure 6.7 (b and e), the arrangement of TiO_2 domains remains uninfluenced after removing the polymer matrix by degradation in deep UV region. This study can be further extended to the solar cell application where the better efficient charge transportation can be realized with these nanostructures.

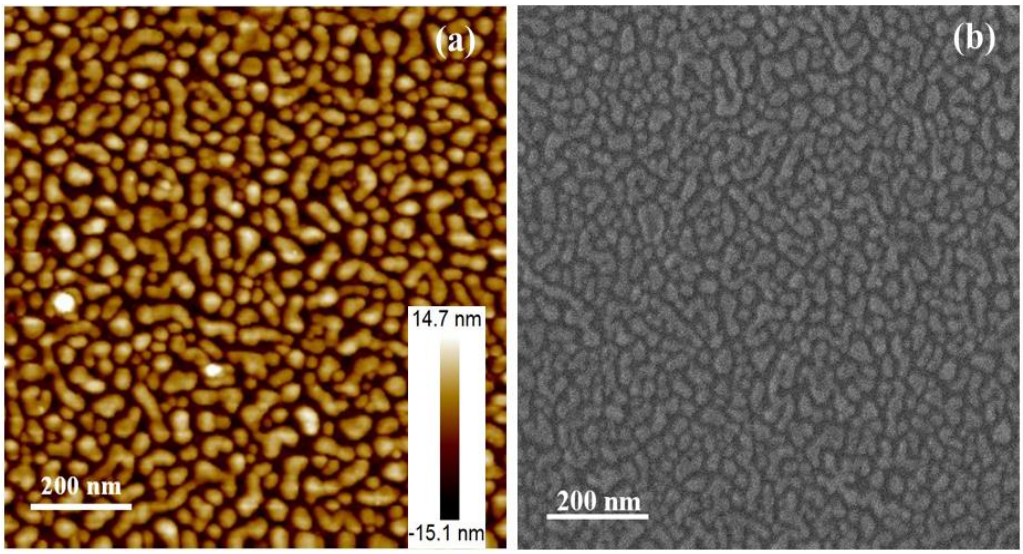

Fig. 6.10 AFM (a) and SEM (b) image of TiO_2 nanostructures after removal of polymer by heating at 450°C

6.4 Conclusions

In summary, the direct assembly of TiO_2 nanodots on the substrate has been obtained. PS-*b*-P4VP thin films were annealed in 1-4 dioxane vapours and used as nanotemplates for the fabrication of an ordered array of TiO_2. Direct deposition of pre-synthesized nanoparticles into templates is a simple approach, and for TiO_2 nanoparticles, this approach is used for the first time by our group. Immersion of nanotemplates into the aqueous solution led to the wetting of walls of pores and supports the selective assembly of nanoparticles. During deposition, sonication also guided the pathways to nanoparticles into the pores. Effect of immersion time on the deposition of nanoparticles have been studied. A dense and ordered array of TiO_2

with high fidelity has been obtained for a particular time. Longer immersion time leads to the agglomerates of TiO_2. This approach is versatile and can be applied to various other size and shape of TiO_2. Here, the diameters of TiO_2 in the hexagonal array lied in the range of exciton diffusion length, so, these structures have the potential to be used in optoelectronic applications.

Chapter 7

Conclusions and Future Scope of Work

7.1 Conclusions

The present thesis represents the successful fabrication of highly ordered TiO_2 nanodots on various substrate which could be used in solar cell application. The following conclusions are made on the basis of the studies carried out:

- √ Synthesis of the SMA thin films using diblock copolymer PS-b-P4VP and additive HABA have been done using dip coating technique. It was found that each domain is microphase separated, but they are not arranged in a regular way due to the fast evaporation of the solvent.

- √ SMA thin films were exposed to the vapors of 1-4 dioxane for the ordering in the thin films (solvent annealing). 1-4 dioxane is a selective solvent, and it offers the different mobility to each copolymer PS and P4VP/HABA. It led to the ordered cylindrical domains normal to the substrate and arranged hexagonally.

- √ For the template formation, the additive was removed chemically. Additive HABA is soluble in ethanol while PS is non-soluble, so ordered porous nanotemplates were obtained by immersing the ordered SMA thin films in ethanol. Hexagonally arranged cylindrical pores with pore size 15 ± 1 nm and periodicity $\sim 31 \pm 2$ nm were obtained.

- √ The effect of substrates on the morphology was also investigated and the morphology was found to be independent of the choice of the substrate which makes these nanotemplates more applicable to various applications. Nanotemplates have been prepared on Si wafers, ITO coated glass and ITO coated PET.

√ Effect of molecular weight and relative volume fraction of minority block have also been studied. Increasing the molecular weight and keeping the relative volume fraction almost same, the morphology remains the same but the domain size (or pore size) and periodicity increases. And changing the relative volume fraction of P4VP/HABA from 0.3 to 0.45, the morphological transition from cylindrical domains to lamellar domains were observed.

√ On removal of additive, lamellar channels with a width of $\sim 14 \pm 2$ nm and periodicity $\sim 31 \pm 2$ nm have been created.

√ For the fabrication of ordered TiO_2 nanostructures, the nanotemplates were immersed in a solution of titania precursor i.e., TTIP (in-situ approach). It was concluded that the templates were overlayered with TiO_2. And on removal the polymer matrix by heating at 450°C, an interconnected network of TiO_2 was obtained on the substrate, but the structures were not the same as that of the templates. The reason was attributed to the high ramp rate and the TiO_2 layer formation over the templates. In the case of lamellar nanotemplates, short wire type interconnected nanostructures were observed while in cylindrical nanotemplates of large pore size, interconnected ring type structures were observed.

√ For the selective deposition into the templates, TiO_2 nanoparticles were synthesized by sol-gel method. As-synthesized nanoparticles were found to be amorphous in nature and become polycrystalline when the nanoparticles were annealed at 350°C. Particle size was calculated as ~ 13 nm at annealing which is not suitable for the templates of pore size of ~ 15 nm. So, the particles size was further reduced by modification in the sol-gel method.

√ Capping agent (1-thiglycerol) was used to reduce the particle size, and it was optimized to ~ 5 nm at annealing temperature of 250°C. Besides, the effect of capping agent on the phase transformation was also investigated. Onset temperature for the phase transformation was found to be increased from 600°C to 700°C, and it was concluded that the anatase phase is more stable when the nanoparticles were synthesized with capping agent. The growth rate of particle size with capping agent was found to be lower than that of without capping agent.

√ TiO_2 nanoparticles with reduced size were deposited into the nanotemplates for different time (ex-situ approach), and polymer was removed by the exposure of UV irradiation for 48 hours. A systematic study of the deposition of nanoparticles into the templates were carried out. An ordered array of TiO_2 nanodots having the morphology mirrors to that of the nanotemplates was obtained for immersion time of 9 hours. Further, increasing the immersion

time leads to the coagulation of nanoparticles and the agglomerates of TiO_2 along with the ordered nanodots were observed.

√ These ordered arrays of TiO_2 could be suggested for organic photovoltaics applications because of their size in the range of exciton diffusion length.

7.2 Future scope of the work

Based on the findings in the present work, future scope of the work can be proposed as follows:

√ Fabrication of highly ordered TiO_2 nanodots by ex-situ approach has been discussed here. So, the same method can be applied for other metal oxides also.

√ TiO_2 have shown their extensive use in solar cells (PSC, DSSC and perovskites). So, the use of these ordered nanostructures can be extended to the device fabrication. Here, we are proposing the plan for the fabrication of polymer solar cells. The schematic of the device is shown in figure 7.1

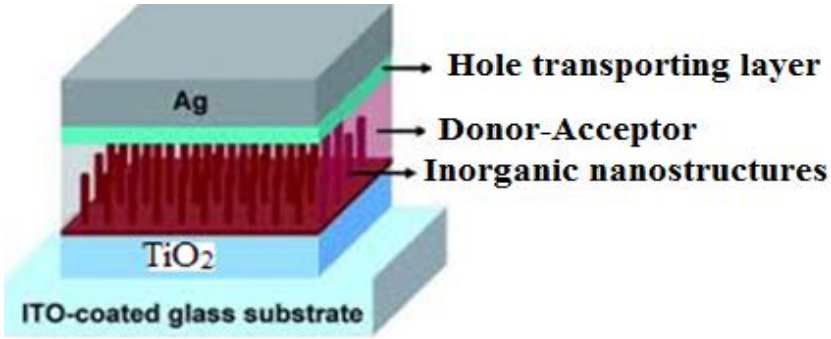

Fig. 7.1 Schematic for the proposed device.

The process flow for the fabrication of hybrid (inorganic/organic) solar cell using the nanostructures prepared by block copolymer templates can be proposed as follows:

- Deposition of thin film of TiO_2 (ETL/HBL) on ITO coated glass by spin coating or dip coating technique.
- Deposition of SMA thin films with cylindrical and lamellar morphology on TiO_2/ITO.
- Ordering in SMA thin films by solvent annealing and creation of porous nanotemplates

- Backfilling of nanotemplates and removal of polymer matrix will lead to the formation of nanodots, nanorods, and nanowalls.
- Filling the gap between the nanodots/nanorods/nanowalls by active materials for solar cells (P3HT: PCBM & PTB7: PCBM) by spin coating.
- Deposition of hole transport layer (HTL).
- Thermal evaporation of back electrode.

Embedded ordered TiO_2 nanostructures within the range of exciton diffusion length, will help for the dissociation of excitons and improvement of the charge transportation to the electrodes. As a result, short circuit current density is expected to be increased and consequently the improvement in PCE of solar cell is also expected.

References

[1] F. S. Bates and G. H. Fredrickson, *Physics today*, 1999, **52**, 32–38.

[2] I. Hamley, *Progress in Polymer Science*, 2009, **34**, 1161–1210.

[3] G. H. Fredrickson and F. S. Bates, *Annual Review of Materials Science*, 1996, **26**, 501–550.

[4] F. S. Bates and G. H. Fredrickson, *Annual review of physical chemistry*, 1990, **41**, 525–557.

[5] W. van Zoelen and G. ten Brinke, *Soft Matter*, 2009, **5**, 1568–1582.

[6] M. Matsen and F. S. Bates, *Macromolecules*, 1996, **29**, 1091–1098.

[7] L. Leibler, *Macromolecules*, 1980, **13**, 1602–1617.

[8] E. Helfand and Z. Wasserman, *Macromolecules*, 1976, **9**, 879–888.

[9] E. Helfand, *Macromolecules*, 1975, **8**, 552–556.

[10] M. Li and C. K. Ober, *Materials Today*, 2006, **9**, 30–39.

[11] J. Ruokolainen, G. t. Brinke and O. Ikkala, *Advanced Materials*, 1999, **11**, 777–780.

[12] J. Ruokolainen, M. Saariaho, O. Ikkala, G. Ten Brinke, E. Thomas, M. Torkkeli and R. Serimaa, *Macromolecules*, 1999, **32**, 1152–1158.

[13] O. Ikkala and G. ten Brinke, *science*, 2002, **295**, 2407–2409.

[14] W. ten Brinke and M. Stamm.

[15] J. Y. Cheng, C. A. Ross, H. I. Smith and E. L. Thomas, *Advanced Materials*, 2006, **18**, 2505–2521.

[16] M. Park, C. Harrison, P. M. Chaikin, R. A. Register and D. H. Adamson, *Science*, 1997, **276**, 1401–1404.

[17] T. Thurn-Albrecht, R. Steiner, J. DeRouchey, C. M. Stafford, E. Huang, M. Bal, M. Tuominen, C. J. Hawker, T. P. Russell *et al.*, *Advanced Materials*, 2000, **12**, 787–791.

[18] A. S. Zalusky, R. Olayo-Valles, J. H. Wolf and M. A. Hillmyer, *Journal of the American Chemical Society*, 2002, **124**, 12761–12773.

[19] J. G. Kennemur, M. A. Hillmyer and F. S. Bates, *Macromolecules*, 2012, **45**, 7228–7236.

[20] G. Pfaff and P. Reynders, *Chemical reviews*, 1999, **99**, 1963–1982.

[21] A. Salvador, M. Pascual-Martı, J. Adell, A. Requeni and J. March, *Journal of pharmaceutical and biomedical analysis*, 2000, **22**, 301–306.

[22] G. Wakefield, M. Green, S. Lipscomb and B. Flutter, *Materials science and technology*, 2004, **20**, 985–988.

[23] R. Zallen and M. Moret, *Solid State Communications*, 2006, **137**, 154–157.

[24] L. Kavan, M. Grätzel, S. Gilbert, C. Klemenz and H. Scheel, *Journal of the American Chemical Society*, 1996, **118**, 6716–6723.

[25] B. O'regan and M. Grfitzeli, *nature*, 1991, **353**, 737–740.

[26] K. Zakrzewska, *Vacuum*, 2004, **74**, 335–338.

[27] A. A. Kashale, K. P. Gattu, K. Ghule, V. H. Ingole, S. Dhanayat, R. Sharma, J.-Y. Chang and A. V. Ghule, *Composites Part B: Engineering*, 2016, **99**, 297–304.

[28] M. Søndergaard, Y. Shen, A. Mamakhel, M. Marinaro, M. Wohlfahrt-Mehrens, K. Wonsyld, S. Dahl and B. B. Iversen, *Chemistry of Materials*, 2014, **27**, 119–126.

[29] A. Bharathi, S. M. Roopan, A. Kajbafvala, R. Padmaja, M. Darsana and G. N. Kumari, *Chinese Chemical Letters*, 2014, **25**, 324–326.

[30] X. Wang, Z. Li, J. Shi and Y. Yu, *Chemical reviews*, 2014, **114**, 9346–9384.

[31] C. Ruan, M. Paulose, O. K. Varghese, G. K. Mor and C. A. Grimes, *The Journal of Physical Chemistry B*, 2005, **109**, 15754–15759.

[32] X. Ren, T. Gershon, D. Iza, D. Munoz-Rojas, K. Musselman and J. MacManus-Driscoll, *Nanotechnology*, 2009, **20**, 365604.

[33] S. Kathirvel, C. Su, Y.-J. Shiao, Y.-F. Lin, B.-R. Chen and W.-R. Li, *Solar Energy*, 2016, **132**, 310–320.

[34] H.-E. Wang, Z. Chen, Y. H. Leung, C. Luan, C. Liu, Y. Tang, C. Yan, W. Zhang, J. A. Zapien, I. Bello *et al.*, *Applied Physics Letters*, 2010, **96**, 263104.

[35] C. Kuo, W. Tang, C. Gau, T. Guo and D. Jeng, *Applied Physics Letters*, 2008, **93**, 263.

[36] S. Yodyingyong, X. Zhou, Q. Zhang, D. Triampo, J. Xi, K. Park, B. Limketkai and G. Cao, *The Journal of Physical Chemistry C*, 2010, **114**, 21851–21855.

[37] W. Lee and S.-J. Park, *Chemical reviews*, 2014, **114**, 7487–7556.

[38] M.-S. Seo, I. Jeong, J.-S. Park, J. Lee, I. K. Han, W. I. Lee, H. J. Son, B.-H. Sohn and M. J. Ko, *Nanoscale*, 2016, **8**, 11472–11479.

[39] J. E. Allen, B. Ray, M. R. Khan, K. G. Yager, M. A. Alam and C. T. Black, *Applied Physics Letters*, 2012, **101**, 063105.

[40] G. Ren, P.-T. Wu and S. A. Jenekhe, *ACS nano*, 2010, **5**, 376–384.

[41] V. Abetz and P. Simon, *Block copolymers I*, 2005, 125–212.

[42] P. Mansky, P. Haikin and E. Thomas, *Journal of Materials Science*, 1995, **30**, 1987–1992.

[43] P. Mansky, C. Harrison, P. Chaikin, R. Register and N. Yao, *Applied physics letters*, 1996, **68**, 2586–2588.

[44] W. Zheng and Z.-G. Wang, *Macromolecules*, 1995, **28**, 7215–7223.

[45] C. Auschra and R. Stadler, *Macromolecules*, 1993, **26**, 2171–2174.

[46] U. Breiner, U. Krappe and R. Stadler, *Macromolecular rapid communications*, 1996, **17**, 567–575.

[47] W. van Zoelen, E. Polushkin and G. Ten Brinke, *Macromolecules*, 2008, **41**, 8807–8814.

[48] S.-H. Tung, N. C. Kalarickal, J. W. Mays and T. Xu, *Macromolecules*, 2008, **41**, 6453–6462.

[49] A. Sidorenko, I. Tokarev, S. Minko and M. Stamm, *Journal of the American Chemical Society*, 2003, **125**, 12211–12216.

[50] B. K. Kuila, E. B. Gowd and M. Stamm, *Macromolecules*, 2010, **43**, 7713–7721.

[51] I. Tokarev, R. Krenek, Y. Burkov, D. Schmeisser, A. Sidorenko, S. Minko and M. Stamm, *Macromolecules*, 2005, **38**, 507–516.

[52] V. Luchnikov, A. Kondyurin, P. Formanek, H. Lichte and M. Stamm, *Nano Letters*, 2007, **7**, 3628–3632.

[53] W. van Zoelen, T. Asumaa, J. Ruokolainen, O. Ikkala and G. Ten Brinke, *Macromolecules*, 2008, **41**, 3199–3208.

[54] W. van Zoelen, S. Bondzic, T. F. Landaluce, J. Brondijk, K. Loos, A.-J. Schouten, P. Rudolf and G. ten Brinke, *Polymer*, 2009, **50**, 3617–3625.

[55] W.-H. Huang, P.-Y. Chen and S.-H. Tung, *Macromolecules*, 2012, **45**, 1562–1569.

[56] K. Albrecht, A. Mourran, X. Zhu, T. Markkula, J. Groll, U. Beginn, W. H. de Jeu and M. Moeller, *Macromolecules*, 2008, **41**, 1728–1738.

[57] J. Kao, J. Tingsanchali and T. Xu, *Macromolecules*, 2011, **44**, 4392–4400.

[58] A. Laforgue, C. G. Bazuin and R. E. Prud'Homme, *Macromolecules*, 2006, **39**, 6473–6482.

[59] H. Huang, Z. Hu, Y. Chen, F. Zhang, Y. Gong, T. He and C. Wu, *Macromolecules*, 2004, **37**, 6523–6530.

[60] C. Sinturel, M. Vayer, M. Morris and M. A. Hillmyer, *Macromolecules*, 2013, **46**, 5399–5415.

[61] I. P. Campbell, C. He and M. P. Stoykovich, *ACS Macro Letters*, 2013, **2**, 918–923.

[62] X. Gu, I. Gunkel, A. Hexemer, W. Gu and T. P. Russell, *Advanced Materials*, 2014, **26**, 273–281.

[63] Z. Qiang, Y. Zhang, J. A. Groff, K. A. Cavicchi and B. D. Vogt, *Soft Matter*, 2014, **10**, 6068–6076.

[64] S. Wu, *The Journal of Physical Chemistry*, 1970, **74**, 632–638.

[65] A. M. Welander, H. Kang, K. O. Stuen, H. H. Solak, M. Müller, J. J. de Pablo and P. F. Nealey, *Macromolecules*, 2008, **41**, 2759–2761.

[66] F. F. Lupi, T. Giammaria, M. Ceresoli, G. Seguini, K. Sparnacci, D. Antonioli, V. Gianotti, M. Laus and M. Perego, *Nanotechnology*, 2013, **24**, 315601.

[67] G. Seguini, T. J. Giammaria, F. F. Lupi, K. Sparnacci, D. Antonioli, V. Gianotti, F. Vita, I. F. Placentino, J. Hilhorst, C. Ferrero *et al.*, *Nanotechnology*, 2014, **25**, 045301.

[68] T. Seshimo, R. Maeda, R. Odashima, Y. Takenaka, D. Kawana, K. Ohmori and T. Hayakawa, *Scientific reports*, 2016, **6**, year.

[69] F. Ferrarese Lupi, T. Giammaria, F. Volpe, F. Lotto, G. Seguini, B. Pivac, M. Laus and M. Perego, *ACS applied materials & interfaces*, 2014, **6**, 21389–21396.

[70] S. Ji, C.-C. Liu, W. Liao, A. L. Fenske, G. S. Craig and P. F. Nealey, *Macromolecules*, 2011, **44**, 4291–4300.

[71] S. H. Kim, M. J. Misner and T. P. Russell, *Advanced Materials*, 2004, **16**, 2119–2123.

[72] S. H. Kim, M. J. Misner, T. Xu, M. Kimura and T. P. Russell, *Advanced Materials*, 2004, **16**, 226–231.

[73] S. Park, B. Kim, J. Xu, T. Hofmann, B. M. Ocko and T. P. Russell, *Macromolecules*, 2009, **42**, 1278–1284.

[74] D. Borah, M. T. Shaw, J. D. Holmes and M. A. Morris, *ACS applied materials & interfaces*, 2013, **5**, 2004–2012.

[75] X. Zhang, K. D. Harris, N. L. Wu, J. N. Murphy and J. M. Buriak, *ACS nano*, 2010, **4**, 7021–7029.

[76] K. W. Gotrik and C. Ross, *Nano letters*, 2013, **13**, 5117–5122.

[77] W. I. Park, K. Kim, H.-I. Jang, J. W. Jeong, J. M. Kim, J. Choi, J. H. Park and Y. S. Jung, *Small*, 2012, **8**, 3762–3768.

[78] J. E. Seppala, R. L. Lewis III and T. H. Epps III, *ACS nano*, 2012, **6**, 9855–9862.

[79] J. W. Jeong, Y. H. Hur, H.-j. Kim, J. M. Kim, W. I. Park, M. J. Kim, B. J. Kim and Y. S. Jung, *ACS nano*, 2013, **7**, 6747–6757.

[80] E. M. Freer, L. E. Krupp, W. D. Hinsberg, P. M. Rice, J. L. Hedrick, J. N. Cha, R. D. Miller and H.-C. Kim, *Nano letters*, 2005, **5**, 2014–2018.

[81] W. A. Phillip, B. O'Neill, M. Rodwogin, M. A. Hillmyer and E. Cussler, *ACS applied materials & interfaces*, 2010, **2**, 847–853.

[82] J. Yin, X. Yao, J.-Y. Liou, W. Sun, Y.-S. Sun and Y. Wang, *ACS nano*, 2013, **7**, 9961–9974.

[83] T. Hirai, M. Leolukman, C. C. Liu, E. Han, Y. J. Kim, Y. Ishida, T. Hayakawa, M.-a. Kakimoto, P. F. Nealey and P. Gopalan, *Advanced Materials*, 2009, **21**, 4334–4338.

[84] E. Kim, H. Ahn, S. Park, H. Lee, M. Lee, S. Lee, T. Kim, E.-A. Kwak, J. H. Lee, X. Lei *et al.*, *ACS nano*, 2013, **7**, 1952–1960.

[85] G. Kim and M. Libera, *Macromolecules*, 1998, **31**, 2569–2577.

[86] Y. Xuan, J. Peng, L. Cui, H. Wang, B. Li and Y. Han, *Macromolecules*, 2004, **37**, 7301–7307.

[87] Y. Wang, X. Hong, B. Liu, C. Ma and C. Zhang, *Macromolecules*, 2008, **41**, 5799–5808.

[88] H. Huang, F. Zhang, Z. Hu, B. Du, T. He, F. K. Lee, Y. Wang and O. K. Tsui, *Macromolecules*, 2003, **36**, 4084–4092.

[89] W. Bai, K. Yager and C. Ross, *Macromolecules*, 2015, **48**, 8574–8584.

[90] E. B. Gowd, B. Nandan, M. K. Vyas, N. C. Bigall, A. Eychmüller, H. Schlörb and M. Stamm, *Nanotechnology*, 2009, **20**, 415302.

[91] P. F. Green, T. M. Christensen and T. P. Russell, *Macromolecules*, 1991, **24**, 252–255.

[92] C. T. Black, C. Forrey and K. G. Yager, *Soft Matter*, 2017, **13**, 3275–3283.

[93] S. Roland, R. E. Prud'homme and C. G. Bazuin, *ACS Macro Letters*, 2012, **1**, 973–976.

[94] H.-Y. Si, J.-S. Chen and G.-M. Chow, *Colloids and Surfaces A: Physicochemical and Engineering Aspects*, 2011, **373**, 82–87.

[95] D. Grosso, *Journal of Materials Chemistry*, 2011, **21**, 17033–17038.

[96] T. Thurn-Albrecht, J. Schotter, G. Kästle, N. Emley, T. Shibauchi, L. Krusin-Elbaum, K. Guarini, C. Black, M. Tuominen and T. Russell, *Science*, 2000, **290**, 2126–2129.

[97] S. Ndoni, M. E. Vigild and R. H. Berg, *Journal of the American Chemical Society*, 2003, **125**, 13366–13367.

[98] R.-M. Ho, C.-K. Chen and Y.-W. Chiang, *Macromolecular rapid communications*, 2009, **30**, 1439–1456.

[99] A. W. Fahmi, H.-G. Braun and M. Stamm, *Advanced Materials*, 2003, **15**, 1201–1204.

[100] S.-Z. Chu, K. Wada, S. Inoue and S.-i. Todoroki, *Chemistry of materials*, 2002, **14**, 266–272.

[101] M. Roulet, M. Vayer and C. Sinturel, *European Polymer Journal*, 2013, **49**, 3897–3903.

[102] P. S. Chinthamanipeta, Q. Lou and D. A. Shipp, *ACS nano*, 2010, **5**, 450–456.

[103] L. Song, Y. M. Lam, C. Boothroyd and P. W. Teo, *Nanotechnology*, 2007, **18**, 135605.

[104] Q. Lou, P. S. Chinthamanipeta and D. A. Shipp, *Langmuir*, 2011, **27**, 15206–15212.

[105] J. Peng, W. Knoll, C. Park and D. H. Kim, *Chemistry of Materials*, 2008, **20**, 1200–1202.

[106] B. Nandan, B. K. Kuila and M. Stamm, *European Polymer Journal*, 2011, **47**, 584–599.

[107] W. Lee, S. Y. Lee, X. Zhang, O. Rabin and R. Briber, *Nanotechnology*, 2013, **24**, 045305.

[108] Z. Liu, T. Chang, H. Huang and T. He, *RSC Advances*, 2013, **3**, 20464–20470.

[109] B. Nandan, E. B. Gowd, N. C. Bigall, A. Eychmüller, P. Formanek, P. Simon and M. Stamm, *Advanced Functional Materials*, 2009, **19**, 2805–2811.

[110] A. Horechyy, B. Nandan, N. E. Zafeiropoulos, P. Formanek, U. Oertel, N. C. Bigall, A. Eychmüller and M. Stamm, *Advanced Functional Materials*, 2013, **23**, 483–490.

[111] E. B. Gowd, B. Nandan, N. C. Bigall, A. Eychmüller, P. Formanek and M. Stamm, *Polymer*, 2010, **51**, 2661–2667.

[112] A. Horechyy, N. E. Zafeiropoulos, B. Nandan, P. Formanek, F. Simon, A. Kiriy and M. Stamm, *Journal of Materials Chemistry*, 2010, **20**, 7734–7741.

[113] I. Barandiaran and G. Kortaberria, *RSC Advances*, 2015, **5**, 95840–95846.

[114] G. W. Nyce, J. R. Hayes, A. V. Hamza and J. H. Satcher, *Chemistry of materials*, 2007, **19**, 344–346.

[115] E. J. Crossland, S. Ludwigs, M. A. Hillmyer and U. Steiner, *Soft Matter*, 2010, **6**, 670–676.

[116] S. Park, J.-Y. Wang, B. Kim, J. Xu and T. P. Russell, *Acs Nano*, 2008, **2**, 766–772.

[117] R. Ruiz, H. Kang, F. A. Detcheverry, E. Dobisz, D. S. Kercher, T. R. Albrecht, J. J. de Pablo and P. F. Nealey, *Science*, 2008, **321**, 936–939.

[118] J. Y. Cheng, C. Ross, V.-H. Chan, E. L. Thomas, R. G. Lammertink and G. J. Vancso, *Advanced Materials*, 2001, **13**, 1174–1178.

[119] S. Y. Yang, I. Ryu, H. Y. Kim, J. K. Kim, S. K. Jang and T. P. Russell, *Advanced materials*, 2006, **18**, 709–712.

[120] S. Y. Yang, J. Park, J. Yoon, M. Ree, S. K. Jang and J. K. Kim, *Advanced Functional Materials*, 2008, **18**, 1371–1377.

[121] K.-V. Peinemann, V. Abetz and P. F. Simon, *Nature materials*, 2007, **6**, 992–996.

[122] P. D. Topham, A. J. Parnell and R. C. Hiorns, *Journal of Polymer Science Part B: Polymer Physics*, 2011, **49**, 1131–1156.

[123] T. M. Clarke and J. R. Durrant, *Chemical reviews*, 2010, **110**, 6736–6767.

[124] S. B. Darling, *Energy & Environmental Science*, 2009, **2**, 1266–1273.

[125] F. Meyers, A. Heeger and J. Brédas, *The Journal of chemical physics*, 1992, **97**, 2750–2758.

[126] X. L. Chen and S. A. Jenekhe, *Macromolecules*, 1996, **29**, 6189–6192.

[127] M. Sommer, A. S. Lang and M. Thelakkat, *Angewandte Chemie International Edition*, 2008, **47**, 7901–7904.

[128] Q. Zhang, A. Cirpan, T. P. Russell and T. Emrick, *Macromolecules*, 2009, **42**, 1079–1082.

[129] W. Chen, Y. Qiu, K. Yan and S. Yang, *Journal of power sources*, 2011, **196**, 10806–10816.

[130] Z. Sun, Y. Cheng, M. Lechmann, J. Li, J. Li, J. Wu, A. Grimsdale, K. Müllen, H.-J. Butt and J. S. Gutmann, *Physical Chemistry Chemical Physics*, 2009, **11**, 1604–1609.

[131] J. Perlich, M. Memesa, A. Diethert, E. Metwalli, W. Wang, S. V. Roth, A. Timmann, J. S. Gutmann and P. Müller-Buschbaum, *ChemPhysChem*, 2009, **10**, 799–805.

[132] J. Lee and J. Y. Jho, *Solar energy materials and solar cells*, 2011, **95**, 3152–3156.

[133] M. Aymerich, A. I. Gómez-Varela, E. Álvarez and M. T. Flores-Arias, *Materials*, 2016, **9**, 728.

[134] S. N. Magonov and M.-H. Whangbo, *Surface analysis with STM and AFM: experimental and theoretical aspects of image analysis*, John Wiley & Sons, 2008.

[135] P. C. Braga and D. Ricci, *Atomic force microscopy: biomedical methods and applications*, Springer Science & Business Media, 2004, vol. 242.

[136] B. Cullity and S. Stock, *Elements of X-ray Diffraction*, Prentice Hall, 2001.

[137] A. Guinier, *X-ray diffraction in crystals, imperfect crystals, and amorphous bodies*, Courier Corporation, 1994.

[138] C. S. Kumar, *Transmission electron microscopy characterization of nanomaterials*, Springer Science & Business Media, 2013.

[139] D. Williams and C. Carter, *SpringerLink (Online service). Transmission Electron Microscopy: A Textbook for Materials Science*, 2009.

[140] C. S. Kumar, *UV-VIS and photoluminescence spectroscopy for nanomaterials characterization*, Springer, 2013.

[141] B. C. Smith, *CRC, Boca Raton, FL*, 1996.

[142] E. Kaufmann, *Characterization of Materials, 2 Volume Set*, Wiley, 2003.

[143] P. Vandenabeele, *Practical Raman spectroscopy: an introduction*, John Wiley & Sons, 2013.

[144] J. R. Ferraro, *Introductory raman spectroscopy*, Academic press, 2003.

[145] G. Wu, *RAMAN SPECTROSCOPY: An Intensity Approach*, World Scientific, 2016.

[146] S. Hofmann, in *Auger-and X-Ray Photoelectron Spectroscopy in Materials Science*, Springer, 2013, pp. 297–408.

[147] T. Xu, A. Zvelindovsky, G. Sevink, K. Lyakhova, H. Jinnai and T. Russell, *Macromolecules*, 2005, **38**, 10788–10798.

[148] C. T. Black, R. Ruiz, G. Breyta, J. Y. Cheng, M. E. Colburn, K. W. Guarini, H.-C. Kim and Y. Zhang, *IBM Journal of Research and Development*, 2007, **51**, 605–633.

[149] A. Mecke, C. Dittrich and W. Meier, *Soft Matter*, 2006, **2**, 751–759.

[150] A. Checco, A. Rahman and C. T. Black, *Advanced Materials*, 2014, **26**, 886–891.

[151] D. Schwark, D. Vezie, J. Reffner, E. Thomas and B. Annis, *Journal of materials science letters*, 1992, **11**, 352–355.

[152] E. Han, K. O. Stuen, M. Leolukman, C.-C. Liu, P. F. Nealey and P. Gopalan, *Macromolecules*, 2009, **42**, 4896–4901.

[153] W. A. Phillip, M. A. Hillmyer and E. Cussler, *Macromolecules*, 2010, **43**, 7763–7770.

[154] J. W. Lee, C. Lee, S. Y. Choi and S. H. Kim, *Macromolecules*, 2009, **43**, 442–447.

[155] C.-H. Lee and S.-H. Tung, *Soft Matter*, 2011, **7**, 5660–5668.

[156] J. Li, Y. Li, J.-T. Xu and C. K. Luscombe, *ACS Applied Materials & Interfaces*, 2017.

[157] S. Zhang, X. Zhang, F. Si, J. Dong, J. Wang, X. Liu, Z. Yin and H. Gao, *Applied Physics Letters*, 2012, **101**, 121104.

[158] J. Zhang, X. Liu, G. Neri and N. Pinna, *Advanced Materials*, 2016, **28**, 795–831.

[159] M. A. Basyooni, M. Shaban and A. M. El Sayed, *Scientific Reports*, 2017, **7**, year.

[160] M. C. Beard, J. M. Luther and A. J. Nozik, *Nature nanotechnology*, 2014, **9**, 951–954.

[161] A. Sirelkhatim, S. Mahmud, A. Seeni, N. H. M. Kaus, L. C. Ann, S. K. M. Bakhori, H. Hasan and D. Mohamad, *Nano-Micro Letters*, 2015, **7**, 219–242.

[162] X. Qin, Y. Sun, N. Wang, Q. Wei, L. Xie, Y. Xie and J.-R. Li, *RSC Advances*, 2016, **6**, 94177–94183.

[163] T. Xu, C. J. Hawker and T. P. Russell, *Macromolecules*, 2005, **38**, 2802–2805.

[164] J. M. Shin, Y. Kim, H. Yun, G.-R. Yi and B. J. Kim, *ACS nano*, 2017, **11**, 2133–2142.

[165] A. Fujishima, *nature*, 1972, **238**, 37–38.

[166] Y. K. Tailor, S. Khandelwal, Y. Kumari, K. Awasthi and M. Kumar, *RSC Advances*, 2015, **5**, 46415–46422.

[167] M. I. Dar, A. K. Chandiran, M. Grätzel, M. K. Nazeeruddin and S. A. Shivashankar, *Journal of Materials Chemistry A*, 2014, **2**, 1662–1667.

[168] A. Abbasi and J. J. Sardroodi, *Environmental Science: Nano*, 2016, **3**, 1153–1164.

[169] L. Ojamäe, C. Aulin, H. Pedersen and P.-O. Käll, *Journal of colloid and interface science*, 2006, **296**, 71–78.

[170] C. J. Ng, H. Gao and T. T. Y. Tan, *Nanotechnology*, 2008, **19**, 445604.

[171] S.-Y. Lee and S.-J. Park, *Journal of Industrial and Engineering Chemistry*, 2013, **19**, 1761–1769.

[172] G. Liu, H. G. Yang, C. Sun, L. Cheng, L. Wang, G. Q. M. Lu and H.-M. Cheng, *CrystEngComm*, 2009, **11**, 2677–2682.

[173] J. H. Braun, *JCT, Journal of coatings technology*, 1997, **69**, 59–72.

[174] R. Scotti, I. R. Bellobono, C. Canevali, C. Cannas, M. Catti, M. D'Arienzo, A. Musinu, S. Polizzi, M. Sommariva, A. Testino *et al.*, *Chemistry of materials*, 2008, **20**, 4051–4061.

[175] A. Bojinova, R. Kralchevska, I. Poulios and C. Dushkin, *Materials Chemistry and Physics*, 2007, **106**, 187–192.

[176] G. Xiang, Y.-G. Wang, D. Wu, T. Li, J. He, J. Li and X. Wang, *Chemistry–A European Journal*, 2012, **18**, 4759–4765.

[177] H. Zhang and J. F. Banfield, *The Journal of Physical Chemistry B*, 2000, **104**, 3481–3487.

[178] C. Liang, Y. Shimizu, T. Sasaki and N. Koshizaki, *Applied Physics A: Materials Science & Processing*, 2005, **80**, 819–822.

[179] B. Souvereyns, K. Elen, C. De Dobbelaere, A. Kelchtermans, N. Peys, J. D'Haen, M. Mertens, S. Mullens, H. Van den Rul, V. Meynen *et al.*, *Chemical engineering journal*, 2013, **223**, 135–144.

[180] P. Bosch-Jimenez, M. Lira-Cantu, C. Domingo and J. A. Ayllón, *Materials Letters*, 2012, **89**, 296–298.

[181] H. Lin, P. W. de Oliveira, I. Grobelsek, A. Haettich and M. Veith, *Zeitschrift für anorganische und allgemeine Chemie*, 2010, **636**, 1947–1954.

[182] A. Rahdar, *World Application Programming*, 2013, **3**, 56–60.

[183] T. C. Jagadale, S. P. Takale, R. S. Sonawane, H. M. Joshi, S. I. Patil, B. B. Kale and S. B. Ogale, *The Journal of Physical Chemistry C*, 2008, **112**, 14595–14602.

[184] L. Alexander and H. P. Klug, *Journal of Applied Physics*, 1950, **21**, 137–142.

[185] T. Ohsaka, F. Izumi and Y. Fujiki, *Journal of Raman spectroscopy*, 1978, **7**, 321–324.

[186] V. Swamy, B. C. Muddle and Q. Dai, *Applied Physics Letters*, 2006, **89**, 163118.

[187] G. Tompsett, G. Bowmaker, R. Cooney, J. Metson, K. Rodgers and J. Seakins, *Journal of Raman Spectroscopy*, 1995, **26**, 57–62.

[188] J. Wang, A. K. Mishra, Q. Zhao and L. Huang, *Journal of Physics D: Applied Physics*, 2013, **46**, 255303.

[189] N. Li, X. Zhang, W. Zhou, Z. Liu, G. Xie, Y. Wang and Y. Du, *Inorganic Chemistry Frontiers*, 2014, **1**, 521–525.

[190] H. C. Choi, Y. M. Jung and S. B. Kim, *Vibrational Spectroscopy*, 2005, **37**, 33–38.

[191] S. Ivanov, A. Barylyak, K. Besaha, A. Bund, Y. Bobitski, R. Wojnarowska-Nowak, I. Yaremchuk and M. Kus-Liśkiewicz, *Nanoscale research letters*, 2016, **11**, 140.

[192] S.-H. Nam, T. K. Kim and J.-H. Boo, *Catalysis today*, 2012, **185**, 259–262.

[193] T. Yamaguchi, T. Jin and K. Tanabe, *The Journal of Physical Chemistry*, 1986, **90**, 3148–3152.

[194] M. Hamadanian, A. Reisi-Vanani and A. Majedi, *Materials Chemistry and Physics*, 2009, **116**, 376–382.

[195] C. McManamon, J. O'Connell, P. Delaney, S. Rasappa, J. D. Holmes and M. A. Morris, *Journal of Molecular Catalysis A: Chemical*, 2015, **406**, 51–57.

[196] G. Tian, H. Fu, L. Jing and C. Tian, *Journal of Hazardous Materials*, 2009, **161**, 1122–1130.

[197] C. Zhai, M. Zhu, Y. Lu, F. Ren, C. Wang, Y. Du and P. Yang, *Physical Chemistry Chemical Physics*, 2014, **16**, 14800–14807.

[198] S. Liu and X. Chen, *Journal of Hazardous Materials*, 2008, **152**, 48–55.

[199] X. Xue, W. Ji, Z. Mao, H. Mao, Y. Wang, X. Wang, W. Ruan, B. Zhao and J. R. Lombardi, *The Journal of Physical Chemistry C*, 2012, **116**, 8792–8797.

[200] M. Zhu, C. Zhai, L. Qiu, C. Lu, A. S. Paton, Y. Du and M. C. Goh, *ACS Sustainable Chemistry & Engineering*, 2015, **3**, 3123–3129.

[201] B. Naik, K. Parida and C. S. Gopinath, *The Journal of Physical Chemistry C*, 2010, **114**, 19473–19482.

[202] D. G. Calatayud, T. Jardiel, M. Rodríguez, M. Peiteado, D. Fernández-Hevia and A. C. Caballero, *Ceramics International*, 2013, **39**, 1195–1202.

[203] R. A. Spurr and H. Myers, *Analytical Chemistry*, 1957, **29**, 760–762.

[204] S. Porto, P. Fleury and T. Damen, *Physical Review*, 1967, **154**, 522.

[205] B. Kannan, K. Castelino and A. Majumdar, *Nano Letters*, 2003, **3**, 1729–1733.

[206] M. Lazzari, C. Rodríguez-Abreu, J. Rivas and M. A. López-Quintela, *Journal of nanoscience and nanotechnology*, 2006, **6**, 892–905.

[207] M. Grzelczak, J. Vermant, E. M. Furst and L. M. Liz-Marzán, *ACS nano*, 2010, **4**, 3591–3605.

[208] M. J. Pavan and R. Shenhar, *Journal of Materials Chemistry*, 2011, **21**, 2028–2040.

[209] S.-S. Kim, C. Chun, J.-C. Hong and D.-Y. Kim, *Journal of Materials Chemistry*, 2006, **16**, 370–375.

[210] I. Vukovic, G. ten Brinke and K. Loos, *Polymer*, 2013, **54**, 2591–2605.

[211] C. Cummins, D. Borah, S. Rasappa, A. Chaudhari, T. Ghoshal, B. O'Driscoll, P. Carolan, N. Petkov, J. Holmes and M. Morris, *Journal of Materials Chemistry C*, 2013, **1**, 7941–7951.

[212] S.-W. Yeh, K.-H. Wei, Y.-S. Sun, U.-S. Jeng and K. S. Liang, *Macromolecules*, 2005, **38**, 6559–6565.

[213] B. J. Kim, J. J. Chiu, G.-R. Yi, D. J. Pine and E. J. Kramer, *Advanced Materials*, 2005, **17**, 2618–2622.

[214] T. Bezrodna, G. Puchkovska, V. Shimanovska, I. Chashechnikova, T. Khalyavka and J. Baran, *Applied surface science*, 2003, **214**, 222–231.

List of Publication

Publications from thesis work

1. **Yogita Kumari**, Lokesh Kumar Jangir, Manoj Kumar, K. C. Swami and Kamlendra Awasthi, Effect of volume fraction of minority block on the morphology of PS-*b*-P4VP nanotemplates, **Macromolecular Symposia**, xxx (2017) xxx (accepted).
2. **Yogita Kumari**, Lokesh Kumar Jangir, Anil Kumar, Manoj Kumar and Kamlendra Awasthi, Investigation of thermal stability of TiO_2 nanoparticles using 1-thioglycerol as capping agent, **Solid State Communications**, 263 (2017) 1.
3. **Yogita Kumari**, Lokesh Kumar Jangir, Manoj Kumar and Kamlendra Awasthi, Titania nanodots using self-assembled poly(styrene)-*b*-poly(4-vinylpyridine) block copolymer nanotemplates via ex-siu approach, **Materials Letters**, 209 (2017) 365 .

Publications other than thesis work

1. **Yogita Kumari**, Lokesh Kumar Jangir, Anil Kumar, Manoj Kumar, K. C. Swami and Kamlendra Awasthi, Structural and morphological study of PS-TiO_2 nanocomposite Membranes, **Macromolecular Symposia**, 357 (2015) 200.
2. Yogesh Kumar Tailor, Sarita Khandelwal, **Yogita Kumari**, Kamlendra Awasthi and Mahendra Kumar, An efficient one pot three- component nanocatalyzed synthesis of spiroheterocycles using TiO_2 nanoparticles as heterogeneous catalyst, **RSC Advances**, 5 (2015) 46415.
3. Anjali Awasthi, Ankita Dube, **Yogita Kumari**, Lokesh Kumar Jangir, Kumud Kant Awasthi, and Kamlendra Awasthi, Toxicological evaluation of TiO_2 nanoparticles in bacterial cell, **Macromolecular Symposia**, 357 (2015) 235.
4. Anil Kumar, Lokesh Kumar Jangir, **Yogita Kumari**, Manoj Kumar, Vinod Kumar and Kamlendra Awasthi, Electrical behaviour of dual-morphology polyaniline, **Journal of Applied Polymer Science**, 133 (2016) 44091.
5. Lokesh Kumar Jangir, **Yogita Kumari**, Anil Kumar, Manoj Kumar and Kamlendra Awasthi, Investigation of luminescent and structural properties of ZnO nanoparticles synthesized with different precursors, **Materials Chemistry Frontiers**, 1 (2017) 1413.
6. Lokesh Kumar Jangir, Purva Bansal, **Yogita Kumari**, K. C. Swami, Manoj Kumar, Ghanshyam Singh and Kamlendra Awasthi, Effective doping of Er^{3+} in ZnO nanoparticles to control its luminescent properties, **Macromolecular Symposia**, xxx (2017) xxx.